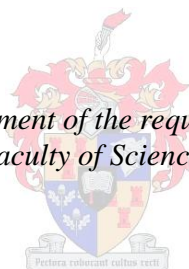


**A detailed kinetic and mechanistic
investigation of the multi-step oxidation of
 $[\text{Pt}^{\text{II}}\text{Cl}_4]^{2-}$ by $[\text{Ir}^{\text{IV}}\text{Cl}_6]^{2-}$ in acidic medium**

by
Jacobus Barend van Dyk

*Thesis presented in fulfilment of the requirements for the degree of
Master of Science in the Faculty of Science at Stellenbosch University*



Supervisor: Dr. Wilhelmus J. Gerber
Prof. Klaus R. Koch

December 2013

Declaration

By submitting this thesis electronically, I declare that the entirety of the work contained therein is my own, original work, that I am the sole author thereof (save to the extent explicitly otherwise stated), that reproduction and publication thereof by Stellenbosch University will not infringe any third party rights and that I have not previously in its entirety or in part submitted it for obtaining any qualification.

Date: December 2013

Copyright © 2013 Stellenbosch University

All rights reserved

Manuscripts in Progress

Manuscript: A detailed kinetic and mechanistic investigation of the multi-step oxidation of $[\text{Pt}^{\text{II}}\text{Cl}_4]^{2-}$ by $[\text{Ir}^{\text{IV}}\text{Cl}_6]^{2-}$ in acidic medium.

Manuscript Title: An ion-pairing reversed phase UHPLC-ESI-Q-TOF-MS method for the characterization of $[\text{Pt}^{\text{IV}}\text{Cl}_{6-n}\text{Br}_n]^{2-}$ ($n = 0 - 6$) and mono-aquated $[\text{Pt}^{\text{IV}}\text{Cl}_{5-n}\text{Br}_n(\text{H}_2\text{O})]^-$ ($n = 0 - 5$) species at the sub parts per million range. (*see Appendix A*)

Acknowledgements

I would sincerely like to thank

- My supervisor, Dr. Wilhelmus J. Gerber, for all his guidance, support and motivation throughout my studies
- My co-supervisor, Prof. Klaus R. Koch, for all his enthusiasm, support and advice
- The University of Stellenbosch for funding
- The technical staff of the Analytical Chemistry department, Shafiek Mohammed, Deidre Davids and Roger Lawrence
- The PGM research group for their advice and support
- My family and Friends for their love and support throughout my studies
- God for the life and knowledge he bestowed onto me

List of Abbreviations

PGM	Platinum Group Metal
UV-Vis	Ultraviolet Visible light
ICP-OES	Inductively coupled plasma optical emission spectroscopy
ESI-Q-TOF-MS	electrospray ionization quadrupole time of flight mass spectroscopy
HCl	Hydrochloric acid
IP-HPLC	Ion-pair high performance liquid chromatography
ppm	parts per million (ICP-OES)
TBA ⁺ Cl ⁻	tetrabutylammonium chloride
ΔG_{rxn}^0	standard Gibbs reaction energy
ΔG^\ddagger	Gibbs energy of activation
ΔH^\ddagger	Enthalpy of activation
ΔS^\ddagger	Entropy of activation

Abstract

A detailed kinetic and mechanistic study of the multi-step oxidation of $[\text{Pt}^{\text{II}}\text{Cl}_4]^{2-}$ by $[\text{Ir}^{\text{IV}}\text{Cl}_6]^{2-}$ in acidic medium was done to investigate the contribution of this redox reaction to the time dependant species evolution of $[\text{Ir}^{\text{IV}}\text{Cl}_6]^{2-}$ and $[\text{Pt}^{\text{IV}}\text{Cl}_6]^{2-}$ during the simultaneous ClO_3^- oxidation of $[\text{Ir}^{\text{III}}\text{Cl}_6]^{3-}$ and $[\text{Pt}^{\text{II}}\text{Cl}_4]^{2-}$.

The kinetic investigation of the redox reaction between $[\text{Pt}^{\text{II}}\text{Cl}_4]^{2-}$ and $[\text{Ir}^{\text{IV}}\text{Cl}_6]^{2-}$ was carried out as a function of reagent concentration, ionic strength and temperature and have shown that the reaction rate is dependent on the concentrations of both $[\text{Pt}^{\text{II}}\text{Cl}_4]^{2-}$ and $[\text{Ir}^{\text{IV}}\text{Cl}_6]^{2-}$. Furthermore, it has been established that the stoichiometry of this reaction is $2 [\text{Ir}^{\text{IV}}\text{Cl}_6]^{2-} : 1 [\text{Pt}^{\text{II}}\text{Cl}_4]^{2-}$. By using the steady state approximation the diffusion controlled rate model was derived. This reaction rate model was simulated to the kinetic data and yielded a rate constant $k_1 = 6.60 \pm 0.46 \text{ M}^{-1} \cdot \text{sec}^{-1}$ at 301.1 K in a 2.73 M HCl solution. The rate of the reaction between $[\text{Ir}^{\text{IV}}\text{Cl}_6]^{2-}$ and $[\text{Pt}^{\text{II}}\text{Cl}_4]^{2-}$ has shown a significant dependence on the ionic strength of the sample matrix and was postulated to be due to the formation of solvent-separated ion-pairs with the cations in solution stabilizing the transition state. The simultaneous ClO_3^- oxidation of $[\text{Pt}^{\text{II}}\text{Cl}_4]^{2-}$ and $[\text{Ir}^{\text{III}}\text{Cl}_6]^{3-}$ was simulated, taking into account the reduction of $[\text{Ir}^{\text{IV}}\text{Cl}_6]^{2-}$ by $[\text{Pt}^{\text{II}}\text{Cl}_4]^{2-}$, $k_1 = 6.60 \pm 0.46 \text{ M}^{-1} \cdot \text{sec}^{-1}$. The simulation shows an induction period in the oxidation of $[\text{Ir}^{\text{IV}}\text{Cl}_6]^{2-}$ and only after complete oxidation of $[\text{Pt}^{\text{II}}\text{Cl}_4]^{2-}$ has occurred can the formation of $[\text{Ir}^{\text{IV}}\text{Cl}_6]^{2-}$ be observed.

The diffusion controlled rate model was simulated to the kinetic runs at varying temperature and the resulting rate constants were used to construct plot of $\ln(k_1/T)$ vs $1/T$ for the determination of the enthalpy- and entropy of activation (ΔH^\ddagger and ΔS^\ddagger). The ΔH^\ddagger and ΔS^\ddagger was determined as $\Delta H^\ddagger = 36.65 \pm 0.24 \text{ kJ} \cdot \text{mol}^{-1}$ and $\Delta S^\ddagger = -107.76 \pm 0.87 \text{ J} \cdot \text{mol}^{-1} \cdot \text{K}^{-1}$.

An IP-HPLC method was developed to study the kinetics of the aquation of $[\text{Ir}^{\text{III}}\text{Cl}_6]^{3-}$ and $[\text{Ir}^{\text{III}}\text{Cl}_5(\text{H}_2\text{O})]^{2-}$ in 0.10 M HCl. A pseudo-first order rate model was simulated to the experimental data and the rate constants were calculated as $k_{\text{aq1}} = 3.50 (\pm 0.12) \times 10^{-5} \text{ sec}^{-1}$ and $k_{\text{aq2}} = 1.14 (\pm 0.10) \times 10^{-6} \text{ sec}^{-1}$. The kinetic runs at varying temperature were used to plot $\ln(k_1/T)$ vs $1/T$ to determine the ΔH^\ddagger and ΔS^\ddagger for the aquation of $[\text{Ir}^{\text{III}}\text{Cl}_6]^{3-}$. This resulted in the values $\Delta H^\ddagger = 99.41 \pm 0.09 \text{ kJ} \cdot \text{mol}^{-1}$ and $\Delta S^\ddagger = 40.70 \pm 0.17 \text{ J} \cdot \text{mol}^{-1} \cdot \text{K}^{-1}$.

An IP-HPLC method was developed for the separation of $[\text{Pt}^{\text{II}}\text{Cl}_4]^{2-}$, $[\text{Pt}^{\text{IV}}\text{Cl}_6]^{2-}$, $[\text{Ir}^{\text{III}}\text{Cl}_6]^{3-}$, $[\text{Ir}^{\text{IV}}\text{Cl}_6]^{2-}$ and their respective aquation products in order to elucidate the mechanism of the redox reaction between $[\text{Ir}^{\text{IV}}\text{Cl}_6]^{2-}$ and $[\text{Pt}^{\text{II}}\text{Cl}_4]^{2-}$. The chromatographic trace obtained from a sample containing $[\text{Ir}^{\text{IV}}\text{Cl}_6]^{2-}$ and $[\text{Pt}^{\text{II}}\text{Cl}_4]^{2-}$ in 0.10 M HCl indicates that no $[\text{Ir}^{\text{III}}\text{Cl}_6]^{3-}$ forms during the reaction but rather that $[\text{Ir}^{\text{III}}\text{Cl}_5(\text{H}_2\text{O})]^{2-}$ is formed. A reaction mechanism that takes chloride transfer into account was proposed.

Opsomming

'n Gedetailleerde kinetiese en meganistiese studie van die meervuldige-stap oksidasie van $[\text{Pt}^{\text{II}}\text{Cl}_4]^{2-}$ deur $[\text{Ir}^{\text{IV}}\text{Cl}_6]^{2-}$ in suurmedium was uitgevoer om die bydrae van hierdie redoksreaksie in die tyd afhanklike spesie evolusie van $[\text{Ir}^{\text{IV}}\text{Cl}_6]^{2-}$ en $[\text{Pt}^{\text{IV}}\text{Cl}_6]^{2-}$ gedurende die gelyktydige ClO_3^- oksidasie van $[\text{Ir}^{\text{III}}\text{Cl}_6]^{3-}$ en $[\text{Pt}^{\text{II}}\text{Cl}_4]^{2-}$ te ondersoek.

Die kinetiese ondersoek van die redoksreaksie tussen $[\text{Pt}^{\text{II}}\text{Cl}_4]^{2-}$ en $[\text{Ir}^{\text{IV}}\text{Cl}_6]^{2-}$ was uitgevoer as 'n funksie van reagens konsentrasie, ioniese sterkte en temperatuur uitgevoer en het getoon dat die reaksietempo afhanklik is van die konsentrasies van beide $[\text{Pt}^{\text{II}}\text{Cl}_4]^{2-}$ en $[\text{Ir}^{\text{IV}}\text{Cl}_6]^{2-}$. Verder, is dit vasgestel dat die stoïgiometrie van die reaksie $2 [\text{Ir}^{\text{IV}}\text{Cl}_6]^{2-} : 1 [\text{Pt}^{\text{II}}\text{Cl}_4]^{2-}$ is. Deur gebruik te maak van die bestendige toestands (steady state) benadering is die “diffusion-controlled rate model” afgelei. Hierdie tempo model (rate model) was gesimuleer op die kinetiese data en 'n tempokonstante (rate constant) $k_1 = 6.60 \pm 0.46 \text{ M}^{-1} \cdot \text{sec}^{-1}$ by 301.1 K in 'n 2.73 M HCl-oplossing was bereken. Die tempo van die reaksie tussen $[\text{Ir}^{\text{IV}}\text{Cl}_6]^{2-}$ en $[\text{Pt}^{\text{II}}\text{Cl}_4]^{2-}$ het getoon dat 'n beduidende afhanklikheid van die reaksietempo op die ioniese sterkte van die monster matriks is teenwoordig en dit is gepostuleer dat die afhanklikheid as gevolg van die vorming van oplosmiddel-geskeide ioon-pare (solvent-separated ion-pairs) met die katione in oplossing is, wat stabilisering van die oorgangs toestand (transition state) veroorsaak. Die gelyktydige ClO_3^- oksidasie van $[\text{Pt}^{\text{II}}\text{Cl}_4]^{2-}$ en $[\text{Ir}^{\text{III}}\text{Cl}_6]^{3-}$ was gesimuleer, met inagneming van die redox reaksie van $[\text{Ir}^{\text{IV}}\text{Cl}_6]^{2-}$ en $[\text{Pt}^{\text{II}}\text{Cl}_4]^{2-}$, $k_1 = 6.60 \pm 0.46 \text{ M}^{-1} \cdot \text{sec}^{-1}$. Die simulاسie toon dat 'n induksie tydperk in die oksidasie van $[\text{Ir}^{\text{IV}}\text{Cl}_6]^{2-}$ veroorsaak word en slegs nadat volledige oksidasie van $[\text{Pt}^{\text{II}}\text{Cl}_4]^{2-}$ plaasgevind het, die vorming van $[\text{Ir}^{\text{IV}}\text{Cl}_6]^{2-}$ waargeneem kan word.

Die “diffusion-controlled rate model” was gesimuleer op die kinetiese data met wisselende temperatuur en die tempokonstantes was gebruik om die plot van $\ln(k_1/T)$ vs $1/T$ te konstrueer vir die bepaling van die entalpie en entropie van aktivering (ΔH^\ddagger en ΔS^\ddagger). Die ΔH^\ddagger en ΔS^\ddagger was bepaal as $\Delta H^\ddagger = 36.65 \pm 0.24 \text{ kJ} \cdot \text{mol}^{-1}$ en $\Delta S^\ddagger = -107.76 \pm 0.87 \text{ J} \cdot \text{mol}^{-1} \cdot \text{K}^{-1}$.

'n IP-HPLC metode was ontwikkel om die kinetika van die “aquation” van $[\text{Ir}^{\text{III}}\text{Cl}_6]^{3-}$ en $[\text{Ir}^{\text{III}}\text{Cl}_5(\text{H}_2\text{O})]^{2-}$ in 0.10 M HCl te bestudeer. 'n “pseudo-first order rate model” was gesimuleer op die eksperimentele data en die tempokonstantes was bereken as $k_{\text{aq1}} = 3.50 (\pm 0.12) \times 10^{-5} \text{ sec}^{-1}$ en $k_{\text{aq2}} = 1.14 (\pm 0.10) \times 10^{-6} \text{ sec}^{-1}$. Die kinetiese experimente

met wisselende temperatuur was gebruik om $\ln(k_1/T)$ vs $1/T$ te stip en die ΔH^\ddagger en ΔS^\ddagger vir die “aquation” van $[\text{Ir}^{\text{III}}\text{Cl}_6]^{3-}$ was bepaal. Dit het gelei tot die waardes van $\Delta H^\ddagger = 99.41 \pm 0.09 \text{ kJ.mol}^{-1}$ en $\Delta S^\ddagger = 40.70 \pm 0.17 \text{ J.mol}^{-1}.\text{K}^{-1}$.

'n IP-HPLC metode was ontwikkel vir die skeiding van $[\text{Pt}^{\text{II}}\text{Cl}_4]^{2-}$, $[\text{Pt}^{\text{IV}}\text{Cl}_6]^{2-}$, $[\text{Ir}^{\text{III}}\text{Cl}_6]^{3-}$, $[\text{Ir}^{\text{IV}}\text{Cl}_6]^{2-}$ en hul onderskeie “aquation” produkte om ten einde die meganisme van die redoksreaksie tussen $[\text{Ir}^{\text{IV}}\text{Cl}_6]^{2-}$ en $[\text{Pt}^{\text{II}}\text{Cl}_4]^{2-}$ toe te lig. Die chromatografiese patroon verkry vanaf 'n oplossing met $[\text{Ir}^{\text{IV}}\text{Cl}_6]^{2-}$ en $[\text{Pt}^{\text{II}}\text{Cl}_4]^{2-}$ in 0.10 M HCl dui daarop dat geen $[\text{Ir}^{\text{III}}\text{Cl}_6]^{3-}$ tydens die reaksie gevorm word nie, maar eerder dat $[\text{Ir}^{\text{III}}\text{Cl}_5(\text{H}_2\text{O})]^{2-}$ as produk gevorm word. 'n reaksie meganisme wat chloried oordrag in ag neem kon opgestel word.

Table of Contents

Declaration.....	i
Manuscripts in Progress.....	ii
Acknowledgements.....	iii
List of Abbreviations	iv
Abstract.....	v
Opsomming.....	vii
Table of Contents.....	ix
List of Figures	xiii
List of Tables	xix
List of Schemes.....	xxi
Chapter 1. General Introduction, Background and Objectives.....	1
1.1. Uses of Platinum group metals (PGM).....	2
1.2. Refining of PGM in industry	4
1.3. Redox chemistry to consider in a mixture of Ir, Pt, and ClO_3^-	6
1.4. Objectives of this study.....	7
1.5. Background on electron transfer processes in transition metal chemistry.....	8
1.5.1. Eyring's transition state theory	9
1.5.2. Marcus theory.....	11
1.6. Description of Equikin, for the simulation of the kinetic rate model	12

Chapter 2. Experimental Procedures and Instrumentation	14
2.1. Preparation of kinetic samples	15
2.2. Analytical Instrumentation	15
2.2.1. UV-Vis spectrophotometer	15
2.2.2. Inductively coupled plasma-optical emission spectroscopy (ICP-OES)	15
2.2.3: Ion-pair high pressure liquid chromatography (IP-HPLC)	16
2.2.4. Electrospray ionization mass spectrometry (ESI MS)	19
2.3. Materials	19
Chapter 3. A detailed kinetic investigation of the oxidation of $[Pt^{II}Cl_4]^{2-}$ by $[Ir^{IV}Cl_6]^{2-}$	20
3.1. Introduction.....	21
3.2. UV-Vis characterization of the pure reagents ($[Ir^{IV}Cl_6]^{2-}$ and $[Pt^{II}Cl_4]^{2-}$) and products ($[Ir^{III}Cl_6]^{3-}$ and $[Pt^{IV}Cl_6]^{2-}$)	22
3.3. UV-Vis spectral changes for the redox reaction of $[Pt^{II}Cl_4]^{2-}$ and $[Ir^{IV}Cl_6]^{2-}$ as a function of time and reaction stoichiometry	24
3.4. Kinetic investigation of the redox reaction ($[Pt^{II}Cl_4]^{2-} + [Ir^{IV}Cl_6]^{2-}$)	27
3.4.1. Reaction rate as a function of $[Pt^{II}Cl_4]^{2-}$ concentration	27
3.4.2. Reaction rate as a function of $[Ir^{IV}Cl_6]^{2-}$ concentration	29
3.4.3. Reaction rate as a function of ionic strength.....	31
3.4.4. Reaction rate as a function of temperature.....	32
3.4.5. Reaction rate as a function of acid concentration	33
3.5. Proposed reaction rate model for the redox reaction between $[Pt^{II}Cl_4]^{2-}$ and $[Ir^{IV}Cl_6]^{2-}$	34

3.6. Evidence for the existence of Pt ^{III} chlorido species in the gas-phase by ESI-MS analysis of [Pt ^{IV} Cl ₆] ²⁻	49
3.7. Simulation of the ClO ₃ ⁻ oxidation of a mixed [Pt ^{II} Cl ₄] ²⁻ and [Ir ^{III} Cl ₆] ³⁻ solution	52
3.8. Concluding remarks	54
Chapter 4. A mechanistic investigation of the first oxidation reaction of [Pt^{II}Cl₄]²⁻ by [Ir^{IV}Cl₆]²⁻	57
4.1. Introduction.....	58
4.2. Aquation kinetics of [Pt ^{II} Cl ₄] ²⁻ , [Pt ^{IV} Cl ₆] ²⁻ and [Ir ^{IV} Cl ₆] ²⁻	59
4.3. IP-HPLC study of the aquation kinetics of [Ir ^{III} Cl ₆] ³⁻ and [Ir ^{III} Cl ₅ (H ₂ O)] ²⁻	61
4.3.1. Tentative assignment of the IP-HPLC chromatographic trace of the [Ir ^{III} Cl _n (H ₂ O) _{n-6}] ³⁻ⁿ (n= 4-6) series of complex anions.....	62
4.3.2. Kinetic investigation of the aquation of [Ir ^{III} Cl ₆] ³⁻ and [Ir ^{III} Cl ₅ (H ₂ O)] ²⁻	64
4.4. IP-HPLC separation of [Pt ^{IV} Cl ₆] ²⁻ , [Pt ^{II} Cl ₄] ²⁻ , [Ir ^{IV} Cl ₆] ²⁻ , [Ir ^{III} Cl ₆] ³⁻ and their respective aquation products.....	70
4.4.1. Reactions that must be taken into account for the investigation of the redox mechanism.....	70
4.4.2. IP-HPLC separation of [Pt ^{IV} Cl ₆] ²⁻ and [Pt ^{II} Cl ₄] ²⁻	71
4.4.3. IP-HPLC separation of [Ir ^{IV} Cl ₆] ²⁻ and [Ir ^{III} Cl ₆] ³⁻	74
4.4.4. IP-HPLC separation of a sample containing a mixture of [Pt ^{II} Cl ₄] ²⁻ , [Pt ^{IV} Cl ₆] ²⁻ , [Ir ^{III} Cl ₆] ³⁻ and their respective aquation products.....	75
4.5. IP-HPLC analysis of the formation of Pt ^{IV} and Ir ^{III} products in 0.1 M HCl.....	76
4.6. Concluding remarks	81

Chapter 5. Conclusions	83
5.1. General conclusion	84
5.2. A more detailed conclusion of this project	85
5.2.1. Kinetic investigation of the multi-step oxidation of $[\text{Pt}^{\text{II}}\text{Cl}_4]^{2-}$ by $[\text{Ir}^{\text{IV}}\text{Cl}_6]^{2-}$	85
5.2.2. A mechanistic investigation of the first oxidation reaction of $[\text{Pt}^{\text{II}}\text{Cl}_4]^{2-}$ by $[\text{Ir}^{\text{IV}}\text{Cl}_6]^{2-}$	87
References	89
Appendix A	A1

List of Figures

- Figure 1.1:** Map of the PGM mining and refining activity in the Bushveld complex of the North-West province, South Africa.
- Figure 1.2:** The demand of PGM in the different areas of industry from 1975 - 2008.
- Figure 1.3:** The energy profile of any spontaneous electron-exchange reaction showing the standard reaction Gibbs energy (ΔG^0_{rxn}) and Gibbs energy of activation (ΔG^\ddagger).
- Figure 1.4:** The energy profile of any spontaneous electron-exchange reaction as described by Transition State Theory showing the standard reaction Gibbs energy (ΔG^0_{rxn}) and Gibbs energy of activation (ΔG^\ddagger). Transition State Theory assumes that the activated complex ($[\text{AB}]^\ddagger$) is a stable molecular state.
- Figure 1.5:** The energy profile of any spontaneous electron-exchange reaction showing the standard reaction Gibbs energy (ΔG^0_{rxn}) and Gibbs energy of activation (ΔG^\ddagger) as represented by the Marcus theory.
- Figure 2.1:** Chromatographic trace of a sample containing $[\text{Ir}^{\text{IV}}\text{Cl}_6]^{2-}$, $[\text{Pt}^{\text{IV}}\text{Cl}_6]^{2-}$, $[\text{Pt}^{\text{II}}\text{Cl}_4]^{2-}$, $[\text{Ir}^{\text{III}}\text{Cl}_6]^{3-}$ and their respective aquation products at varying acetonitrile concentrations. (a) $[\text{Ir}^{\text{IV}}\text{Cl}_6]^{2-}$, (b) $[\text{Pt}^{\text{IV}}\text{Cl}_6]^{2-}$, (c) unknown Pt^{IV} species, (d) $[\text{Pt}^{\text{IV}}\text{Cl}_5(\text{H}_2\text{O})]^-$, (e) $[\text{Pt}^{\text{II}}\text{Cl}_4]^{2-}$, (f) $[\text{Ir}^{\text{III}}\text{Cl}_6]^{3-}$, (g) $[\text{Ir}^{\text{III}}\text{Cl}_5(\text{H}_2\text{O})]^{2-}$, (h) $[\text{Ir}^{\text{III}}\text{Cl}_4(\text{H}_2\text{O})_2]^-$.
- Figure 2.2:** Mobile phase gradient employed for the IP-HPLC separation of $[\text{Ir}^{\text{IV}}\text{Cl}_6]^{2-}$, $[\text{Pt}^{\text{II}}\text{Cl}_4]^{2-}$, $[\text{Pt}^{\text{IV}}\text{Cl}_6]^{2-}$, $[\text{Ir}^{\text{III}}\text{Cl}_6]^{3-}$ and their respective aquated products.
- Figure 3.1:** Molar extinction coefficient plots of the species; (a) $[\text{Ir}^{\text{IV}}\text{Cl}_6]^{2-}$, (b) $[\text{Pt}^{\text{II}}\text{Cl}_4]^{2-}$, (c) $[\text{Ir}^{\text{III}}\text{Cl}_6]^{3-}$ and (d) $[\text{Pt}^{\text{IV}}\text{Cl}_6]^{2-}$, all in a 6.0 M HCl matrix
- Figure 3.2:** Reduction of $[\text{Ir}^{\text{IV}}\text{Cl}_6]^{2-}$ by $[\text{Pt}^{\text{II}}\text{Cl}_4]^{2-}$ observed with UV-Vis spectroscopy, as a function of time. Spectra were recorded every 1.5 minutes.

- Figure 3.3:** UV-Vis spectrum of the reduction of $[\text{Ir}^{\text{IV}}\text{Cl}_6]^{2-}$ by $[\text{Pt}^{\text{II}}\text{Cl}_4]^{2-}$ after a reaction time of 5 hours. The peak at 262 nm, corresponds well with that of $[\text{Pt}^{\text{IV}}\text{Cl}_6]^{2-}$.
- Figure 3.4:** UV-Vis absorbance for the redox reaction of $[\text{Ir}^{\text{IV}}\text{Cl}_6]^{2-}$ and $[\text{Pt}^{\text{II}}\text{Cl}_4]^{2-}$ at 488 nm measured as a function of time. The $[\text{Pt}^{\text{II}}\text{Cl}_4]^{2-}$ concentration for each reaction are shown in the legend. $[\text{Ir}^{\text{IV}}\text{Cl}_6]^{2-}$ concentration = 0.213 ± 0.007 mM, HCl concentration = 2.730 M, monitored at a temperature of 301.1 ± 0.2 K
- Figure 3.5:** UV-Vis absorbance for the redox reaction between $[\text{Ir}^{\text{IV}}\text{Cl}_6]^{2-}$ and $[\text{Pt}^{\text{II}}\text{Cl}_4]^{2-}$ measured at 488 nm as a function of time. $[\text{Ir}^{\text{IV}}\text{Cl}_6]^{2-}$ concentrations are shown in the legend. $[\text{Pt}^{\text{II}}\text{Cl}_4]^{2-}$ concentration = 0.237 ± 0.003 mM and HCl concentration = 2.730 M, monitored at a temperature of 301.1 ± 0.2 K
- Figure 3.6:** Investigation of the effect of ionic strength on the redox reaction rate by means of UV-Vis spectroscopy at 488 nm. 0.217 ± 0.008 mM $[\text{Ir}^{\text{IV}}\text{Cl}_6]^{2-}$ and 0.241 ± 0.005 mM $[\text{Pt}^{\text{II}}\text{Cl}_4]^{2-}$ was reacted at a constant temperature of 301.1 ± 0.2 K.
- Figure 3.7:** Dependence of the reaction rate on temperature. The UV-Vis absorbance was measured at 488 nm as a function of time with samples containing 0.233 ± 0.001 mM $[\text{Pt}^{\text{II}}\text{Cl}_4]^{2-}$, 0.225 ± 0.002 mM $[\text{Ir}^{\text{IV}}\text{Cl}_6]^{2-}$ and 2.73 M HCl, Table 3.4.
- Figure 3.8:** Investigation of the effect of acid concentration on the reaction rate at 301.1 ± 0.2 K. 0.224 ± 0.005 mM $[\text{Ir}^{\text{IV}}\text{Cl}_6]^{2-}$ and 0.238 ± 0.003 mM $[\text{Pt}^{\text{II}}\text{Cl}_4]^{2-}$ was reacted at a constant Cl^- concentration of 2.73 M. The UV-Vis absorbance at 488 nm was measured as a function of time.
- Figure 3.9:** The non-linear least-squares fits of the multi-step reaction rate model described by Equations 3.14 - 3.18 at varying $[\text{Pt}^{\text{II}}\text{Cl}_4]^{2-}$ concentrations. The dotted plots represent the experimental data with the simulated functions represented by the solid lines.

- Figure 3.10:** The non-linear least-squares fit of the multi-step reaction rate model described by Equations 3.14 - 3.18 at varying $[\text{Ir}^{\text{IV}}\text{Cl}_6]^{2-}$ concentrations. The dotted plots represent the experimental data with the simulated functions represented by the solid lines.
- Figure 3.11:** The UV-Vis spectrum of the $[\text{Pt}^{\text{III}}\text{Cl}_5]^{2-}$ species (spectrum 5 of this figure) as obtained by laser flash photolysis and published by Glebov et al.
- Figure 3.12:** The non-linear least squares-fit of the diffusion controlled rate model, Equations 3.22 - 3.25, at varying $[\text{Pt}^{\text{II}}\text{Cl}_4]^{2-}$ concentrations. The dotted plots represent the experimental data with the simulated functions represented by the solid lines.
- Figure 3.13:** The non-linear least-squares fits of the diffusion controlled rate model, Equations 3.22 - 3.25, at varying $[\text{Ir}^{\text{IV}}\text{Cl}_6]^{2-}$ concentrations. The dotted plots represent the experimental data with the simulated functions represented by the solid lines.
- Figure 3.14:** Fits of the average rate constant and molar extinction coefficients, Table 3.6, to the kinetic data sets at varying $[\text{Pt}^{\text{II}}\text{Cl}_4]^{2-}$ concentrations.
- Figure 3.15:** Fits of the average rate constant and molar extinction coefficients, Table 3.6, to the kinetic data sets at varying $[\text{Ir}^{\text{IV}}\text{Cl}_6]^{2-}$ concentration.
- Figure 3.16:** The non-linear least-squares fits of the diffusion controlled rate model, Equations 3.22 - 3.25, at varying ionic strength. The dotted plots represent the experimental data with the simulated functions represented by the solid lines.
- Figure 3.17:** A plot of the calculated rate constant (k_1) listed in Table 3.7 vs. ionic strength representing the dependence of the reaction rate on the change in ionic strength.
- Figure 3.18:** The non-linear least-squares fits of the diffusion controlled rate model, Equations 3.22 - 3.25, at varying temperature. The dotted plots represent the experimental data with the simulated functions represented by the solid lines.

Figure 3.19: The Eyring plot of the calculate rate constants as obtained by the diffusion controlled rate model, Equations 3.22 - 3.25, at varying temperature.

Figure 3.20: The high resolution ESI mass spectra obtained from the direct infusion analysis of $[\text{Pt}^{\text{IV}}\text{Cl}_6]^{2-}$ as a function of cone voltage.

Figure 3.21: ESI-Mass Spectra of a $[\text{Pt}^{\text{IV}}\text{Cl}_6]^{2-}$ sample in acetonitrile. The experimental data for species (a) $[\text{Pt}^{\text{IV}}\text{Cl}_6]^{2-}$, (c) $[\text{Pt}^{\text{IV}}\text{Cl}_5]^-$, (e) $[\text{Pt}^{\text{III}}\text{Cl}_4]^-$ and (g) $[\text{Pt}^{\text{II}}\text{Cl}_3]^-$ is compared to their respective simulated spectra: (b) $[\text{Pt}^{\text{IV}}\text{Cl}_6]^{2-}$, (d) $[\text{Pt}^{\text{IV}}\text{Cl}_5]^-$, (f) $[\text{Pt}^{\text{III}}\text{Cl}_4]^-$ and (h) $[\text{Pt}^{\text{II}}\text{Cl}_3]^-$

Figure 3.22: Simulation of the ClO_3^- oxidation of a mixture of $[\text{Pt}^{\text{II}}\text{Cl}_4]^{2-}$ and $[\text{Ir}^{\text{III}}\text{Cl}_6]^{3-}$ with the consideration of the redox reaction between $[\text{Pt}^{\text{II}}\text{Cl}_4]^{2-}$ and $[\text{Ir}^{\text{IV}}\text{Cl}_6]^{2-}$. An induction period for the formation of $[\text{Ir}^{\text{IV}}\text{Cl}_6]^{2-}$ can be observed.

Figure 3.23: The effect of the redox reaction between $[\text{Ir}^{\text{IV}}\text{Cl}_6]^{2-}$ and $[\text{Pt}^{\text{II}}\text{Cl}_4]^{2-}$ on the species evolution of $[\text{Pt}^{\text{IV}}\text{Cl}_6]^{2-}$ and $[\text{Ir}^{\text{IV}}\text{Cl}_6]^{2-}$ during the simultaneous ClO_3^- oxidation of $[\text{Pt}^{\text{II}}\text{Cl}_4]^{2-}$ and $[\text{Ir}^{\text{III}}\text{Cl}_6]^{3-}$. (a) the change of $[\text{Ir}^{\text{III}}\text{Cl}_6]^{3-}$ concentration in the presence of $[\text{Pt}^{\text{II}}\text{Cl}_4]^{2-}$, (b) the change of $[\text{Ir}^{\text{III}}\text{Cl}_6]^{3-}$ concentration in the absence of $[\text{Pt}^{\text{II}}\text{Cl}_4]^{2-}$

Figure 4.1: Simulation illustrating the aquation of $[\text{Pt}^{\text{II}}\text{Cl}_4]^{2-}$ and aquation of $[\text{Pt}^{\text{II}}\text{Cl}_3(\text{H}_2\text{O})]^-$, Equation 4.3, in 0.5 M HClO_4 .

Figure 4.2: IP-HPLC separation of the $[\text{Ir}^{\text{III}}\text{Cl}_n(\text{H}_2\text{O})_{n-6}]^{3-n}$ ($n= 4-6$) series of complex anions in 4.1 M chloride after 33 days (4.0 M NaCl and 0.1 M HCl) detected at 254 nm. (a) shows the complete chromatogram and (b) shows the higher aquated species present at relatively low concentrations.

Figure 4.3: The change in the $[\text{Ir}^{\text{III}}\text{Cl}_n(\text{H}_2\text{O})_{n-6}]^{3-n}$ ($n= 4-6$) series of complex anion amounts as a function of time at 295.1. (Note: Reaction Time illustrated on a logarithmic scale)

- Figure 4.4:** Species concentration determined as a function of time. The symbols represent the data obtained from the chromatographic traces in Figure 4.3 and the solid lines represent the non-linear least-squares fit calculated with the program *Equikin*.
- Figure 4.5:** Plot of the natural logarithm of the absorbance measured for $[\text{Ir}^{\text{III}}\text{Cl}_6]^{3-}$ as a function of time, for the calculation of the rate constant, k_{aq1} .
- Figure 4.6:** Plot of $\ln(k_{\text{aq1}}/T)$ as a function of $(1/T)$. From this plot the thermodynamic parameters (ΔH^\ddagger and ΔS^\ddagger) were calculated.
- Figure 4.7:** Chromatographic separation of the $[\text{Pt}^{\text{IV}}\text{Cl}_n(\text{H}_2\text{O})_{6-n}]^{4-n}$ ($n=3-6$) series of complexes detected at 262 nm, (a) fac- and mer- $[\text{Pt}^{\text{IV}}\text{Cl}_3(\text{H}_2\text{O})_3]^+$.
- Figure 4.8:** Chromatographic separation of the $[\text{Pt}^{\text{II}}\text{Cl}_n(\text{H}_2\text{O})_{4-n}]^{2-n}$ ($n=3-4$) series of complex anions detected at 250 nm
- Figure 4.9:** Chromatographic separation of the $[\text{Ir}^{\text{III}}\text{Cl}_n(\text{H}_2\text{O})_{6-n}]^{3-n}$ ($n = 4-6$) species detected at 254 nm
- Figure 4.10:** Chromatographic trace of the simultaneous separation of $[\text{Ir}^{\text{III}}\text{Cl}_6]^{3-}$, $[\text{Pt}^{\text{II}}\text{Cl}_4]^{2-}$, $[\text{Pt}^{\text{IV}}\text{Cl}_6]^{2-}$ and their respective aquation products detected at 250 nm. (a) the $[\text{Ir}^{\text{III}}\text{Cl}_5(\text{H}_2\text{O})]^{2-}$ and cis or trans- $[\text{Pt}^{\text{IV}}\text{Cl}_4(\text{H}_2\text{O})_2]$ species co-eluting, (b) $[\text{Ir}^{\text{III}}\text{Cl}_4(\text{H}_2\text{O})_2]^-$, (c) unknown species, (d) cis or trans- $[\text{Pt}^{\text{IV}}\text{Cl}_4(\text{H}_2\text{O})_2]$, (e) fac and mer- $[\text{Pt}^{\text{IV}}\text{Cl}_3(\text{H}_2\text{O})_3]^+$.
- Figure 4.11:** Investigation of the Ir^{III} and Pt^{IV} reaction products in 0.10 M chloride after a reaction time of 5 min, for the rationalization of the reaction mechanism for the redox reaction between $[\text{Ir}^{\text{IV}}\text{Cl}_6]^{2-}$ and $[\text{Pt}^{\text{II}}\text{Cl}_4]^{2-}$, (a) unknown species, (b) small amounts of $[\text{Ir}^{\text{IV}}\text{Cl}_6]^{2-}$ observed.
- Figure 4.12:** PDA spectra of $[\text{Pt}^{\text{IV}}\text{Cl}_5(\text{H}_2\text{O})]^-$ obtained from Figure 4.7 and $[\text{Pt}^{\text{II}}\text{Cl}_4]^{2-}$ obtained from Figure 4.8.

Figure 4.13: The PDA spectrum of $[\text{Pt}^{\text{IV}}\text{Cl}_5(\text{H}_2\text{O})]^-$ in Figure 4.11 with the simulation of $0.05 \times [\text{Pt}^{\text{II}}\text{Cl}_4]^{2-} + 0.975 \times [\text{Pt}^{\text{IV}}\text{Cl}_5(\text{H}_2\text{O})]^-$ from the PDA spectra given in Figure 4.12.

List of Tables

- Table 3.1:** Summary of the molar extinction coefficients of species represented in Figure 3.1(a) - (b). Molar extinction coefficients at selected peak maxima and 488 nm are reported
- Table 3.2:** The concentration of $[\text{Ir}^{\text{IV}}\text{Cl}_6]^{2-}$, $[\text{Pt}^{\text{II}}\text{Cl}_4]^{2-}$ and HCl in the prepared samples for the investigation of the reaction rate dependence on $[\text{Pt}^{\text{II}}\text{Cl}_4]^{2-}$ concentration
- Table 3.3:** The concentrations of $[\text{Ir}^{\text{IV}}\text{Cl}_6]^{2-}$, $[\text{Pt}^{\text{II}}\text{Cl}_4]^{2-}$ and HCl in the prepared samples for the investigation of the reaction rate dependence on $[\text{Ir}^{\text{IV}}\text{Cl}_6]^{2-}$ concentration
- Table 3.4:** The concentrations of $[\text{Ir}^{\text{IV}}\text{Cl}_6]^{2-}$, $[\text{Pt}^{\text{II}}\text{Cl}_4]^{2-}$ and HCl in the prepared samples for the investigation of the reaction rate dependence on temperature
- Table 3.5:** Rate constants and molar extinction coefficients, calculated by simulation of the multi-step reaction rate model on the experimental data, Equations 3.14 - 3.18.
- Table 3.6:** Rate constants and molar extinction coefficients calculated by simulation of the diffusion controlled rate model, Equations 3.22 - 3.25, on the experimental data
- Table 3.7:** Rate constants and molar extinction coefficients calculated by simulation of the diffusion controlled rate model, Equations 3.22 - 3.25, on the experimental data at variable ionic strength
- Table 3.8:** Rate constants and molar extinction coefficients calculated by simulation of the diffusion controlled rate model, Equations 3.22 - 3.25, on the experimental data at variable temperature
- Table 4.1:** Calculated rate constants obtained with the pseudo-first order rate model, Equations 4.11 - 4.13, compared to rate constants reported in literature.
- Table 4.2:** Rate constants calculated for the aquation of $[\text{Ir}^{\text{III}}\text{Cl}_6]^{3-}$ as a function of temperature.

Table 4.3: Peak assignment for the chromatographic separation of $[\text{Pt}^{\text{IV}}\text{Cl}_n(\text{H}_2\text{O})_{6-n}]^{4-n}$ ($n = 3-6$) in Figure 4.7.

Table 4.4: Peak assignment for the chromatographic separation of $[\text{Pt}^{\text{II}}\text{Cl}_n(\text{H}_2\text{O})_{4-n}]^{2-n}$ ($n = 3-4$) in Figure 4.8

Table 4.5: Peak assignment for the chromatographic separation of $[\text{IrCl}_n(\text{H}_2\text{O})_{6-n}]^{3-n}$ ($n = 4-6$) in Figure 4.9.

List of Schemes

- Scheme 1.1:** General PGM Refining Scheme illustrating the step-wise removal of the PGM during the refining process.
- Scheme 1.2:** A Schematic representation of the redox reactions that can occur in a sample containing $[\text{Ir}^{\text{III}}\text{Cl}_6]^{3-}$, $[\text{Pt}^{\text{II}}\text{Cl}_4]^{2-}$ and ClO_3^- .
- Scheme 4.1:** Proposed reaction mechanism for the redox reaction between $[\text{Ir}^{\text{IV}}\text{Cl}_6]^{2-}$ and $[\text{Pt}^{\text{II}}\text{Cl}_4]^{2-}$. The relative nature of X will result in a mixture of $[\text{Ir}^{\text{III}}\text{Cl}_6]^{3-}$ and $[\text{Ir}^{\text{III}}\text{Cl}_5(\text{H}_2\text{O})]^{2-}$ depending on the free chloride concentration of the sample matrix.

Chapter 1

General Introduction, Background and Objectives

1

General Introduction, Background and Objectives

1.1. Uses of Platinum group metals (PGM)

The transition metals consisting of Pt, Pd, Ru, Os, Ir and Rh are commonly referred to as the platinum group metals (PGMs). The largest global deposits of PGMs are scattered around the Bushveld complex in the North-West province of South Africa, Figure 1.1, containing an estimated 82 % of the world's PGMs.¹ South Africa produces 85 % of the global production of PGMs.¹ PGMs as a commodity is extremely rare because of the relatively low abundances of these elements in the earth's crust (1 - 10 ng.g⁻¹ Pt and 0.3 - 5 ng.g⁻¹ Ir)² and the difficult, time consuming processes required for the extraction of PGMs.^{3,4}

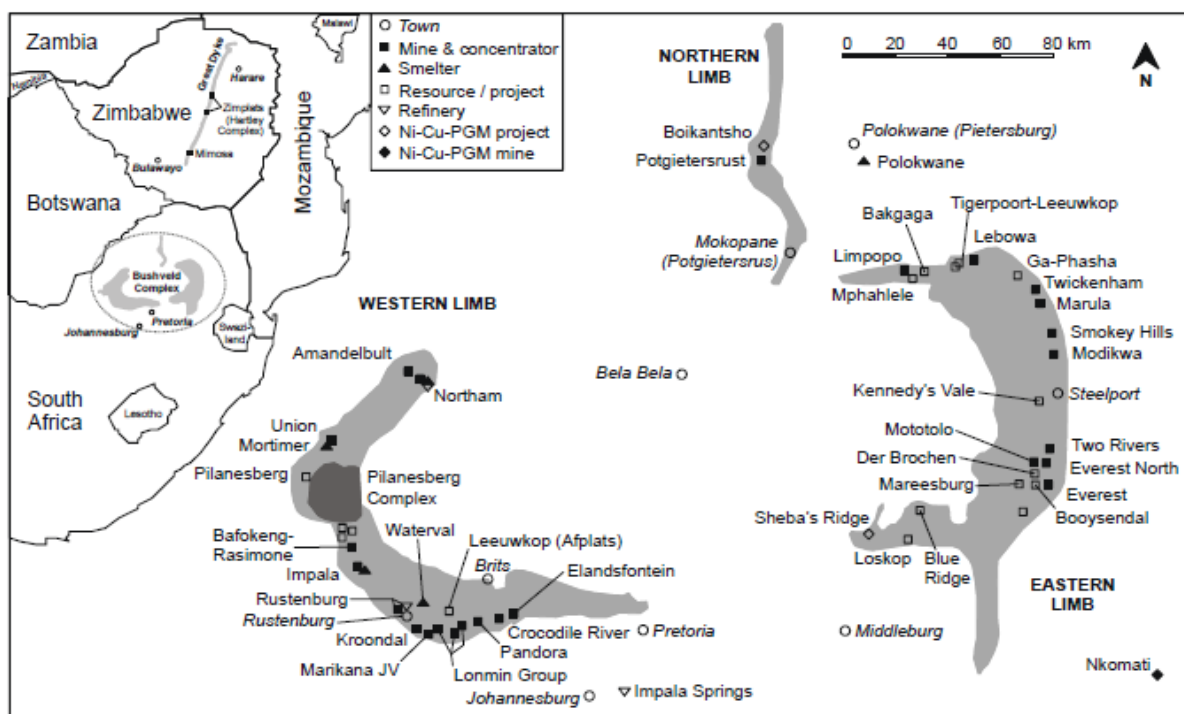


Figure 1.1: Map of the PGM mining and refining activity in the Bushveld complex of the North-West province, South Africa.⁵

Apart from the use of Pt as an investment metal and to produce jewellery, PGMs play a vital role in many industrial processes. PGMs are physiochemically inert² and are therefore used for the production of high temperature- and corrosion resistant materials, *i.e.* for the processing of corrosive molten glass⁶ and the production of turbine blade coatings for jet engines⁷. Many PGMs also have the unique ability to expedite redox reactions and form the basis of many industrially important catalysts,⁸ *e.g.* Pt catalysts are employed for the oxidation of ammonia to nitric acid.⁹ The catalytic properties of PGMs were known since 1823 and ensures the high demand for PGMs.² The petroleum refining and pharmaceutical industries are dependent on PGM catalysts for various organic reactions such as the reforming and hydrogenation of organic molecules.⁴ The largest consumer of PGMs is the automobile industry where as much as 10 g PGMs are employed as automobile catalytic converters. In 2004 the automobile industry consumed 43 % Pt, 50 % Pd and 85 % Rh of the global annual production of PGMs with a further increase reported each year, Figure 1.2.¹⁰ These catalytic converters are essential for the conversion of toxic exhaust fumes, such as carbon monoxide, volatile hydrocarbons and nitrogen oxides to more environmentally friendly compounds.² The limited availability and high market value of PGMs has stimulated PGM recycling industries. However, because of the increasing demand for PGMs, a substantial annual mining of PGMs is still required.⁵

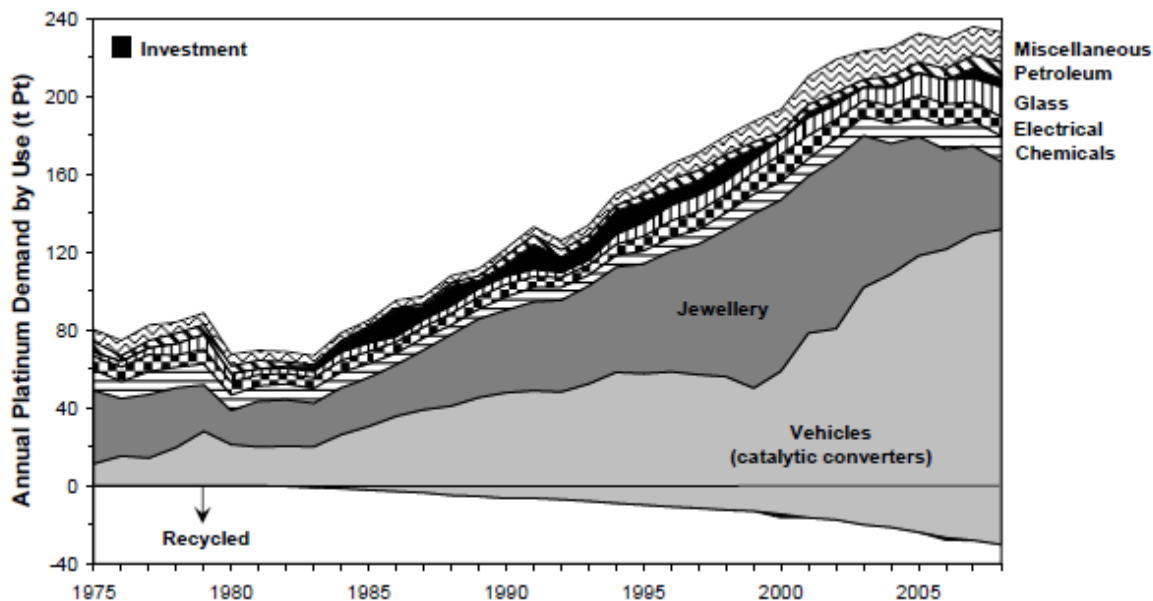
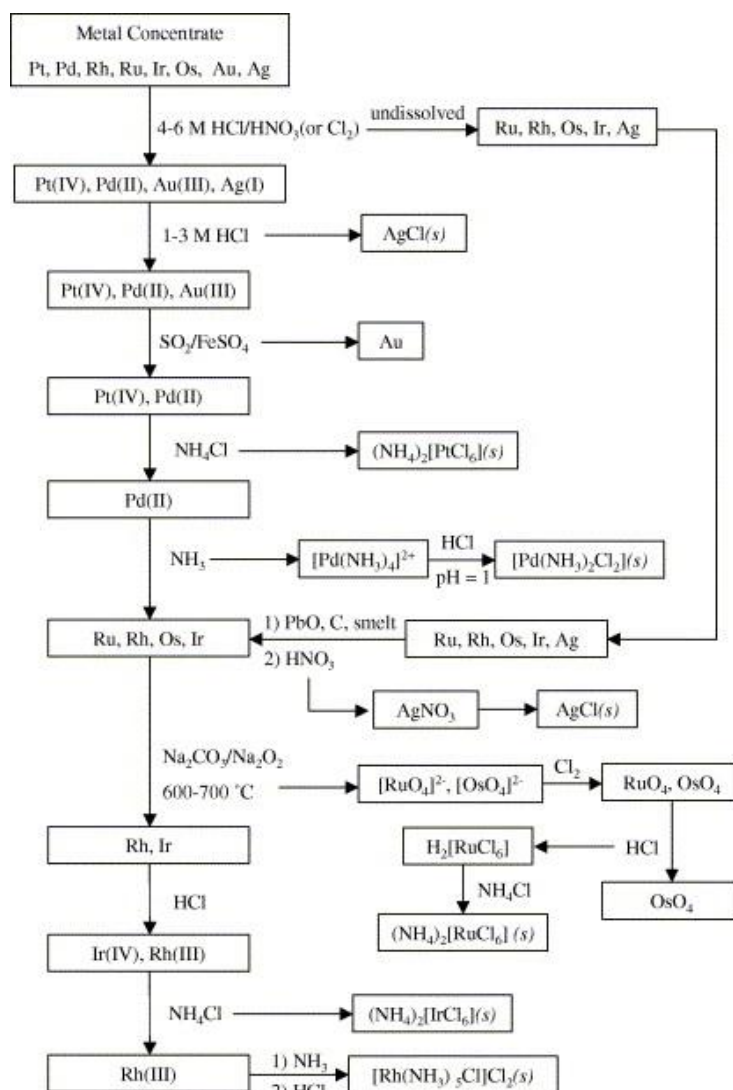


Figure 1.2: The demand of PGM in the different areas of industry from 1975 - 2008.⁵

1.2. Refining of PGM in industry

The ore found in the Bushveld complex contains PGMs at concentrations of less than 10 grams per ton (g/t) and several mechanical and metallurgical procedures (*i.e.* flotation and smelting) are required to concentrate the PGMs into the range of 100 g/t.^{4,5} The PGMs are then oxidized with Cl_2 or a mixture of ClO_3^- and BrO_3^- in relatively concentrated HCl solutions and results in the formation of water soluble PGM chlorido complexes, such as the $[\text{Pt}^{\text{IV}}\text{Cl}_6]^{2-}$, $[\text{Rh}^{\text{III}}\text{Cl}_6]^{3-}$, $[\text{Pd}^{\text{II}}\text{Cl}_4]^{2-}$, $[\text{Ir}^{\text{IV}}\text{Cl}_6]^{2-}$ and $[\text{Ir}^{\text{III}}\text{Cl}_6]^{3-}$ complex anions.^{11,12} Industrial separation and refining of the anionic PGM chlorido complexes are predominantly based on the subtle differences in the physicochemical properties of these PGM complexes, Scheme 1.1.² The separation of Ru and Os from the feed solution is achieved by oxidative distillation of these PGMs as uncharged volatile $[\text{Ru}^{\text{VIII}}\text{O}_4]$ and $[\text{Os}^{\text{VIII}}\text{O}_4]$ complexes.¹³ Refining of the 4 remaining PGMs demand techniques such as solvent extraction, ion exchange and selective precipitation to successfully isolate and purify these precious metals.⁴ The oxidation states of the different PGM complexes and hence their overall charge, are exploited to successfully carry out such refining techniques, since their physicochemical properties are different.

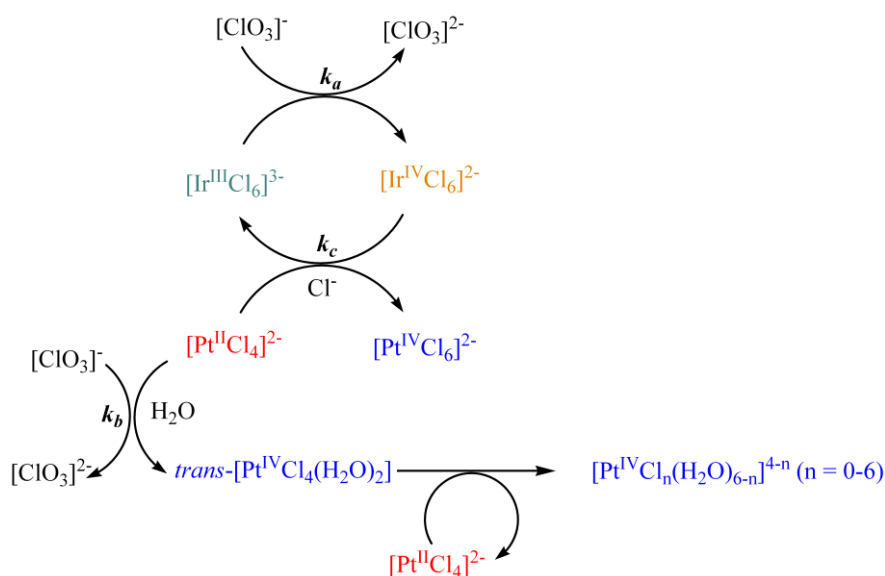


Scheme 1.1: General PGM Refining Scheme illustrating the step-wise removal of the PGM during the refining process.²

In many PGM refining processes, $[\text{Pt}^{\text{IV}}\text{Cl}_6]^{2-}$ is separated from $[\text{Ir}^{\text{III}}\text{Cl}_6]^{3-}$ by means of solvent extraction with the $[\text{Pt}^{\text{IV}}\text{Cl}_6]^{2-}$ species migrating to the organic phase.¹⁴ The high charge of the $[\text{Ir}^{\text{III}}\text{Cl}_6]^{3-}$ complex results in a relatively high hydration energy compared to $[\text{Pt}^{\text{IV}}\text{Cl}_6]^{2-}$ and requires more energy to desolvate and transfer to the organic phase. A similar method is employed for the subsequent separation of $[\text{Ir}^{\text{IV}}\text{Cl}_6]^{2-}$ from $[\text{Rh}^{\text{III}}\text{Cl}_6]^{3-}$ by oxidizing $[\text{Ir}^{\text{III}}\text{Cl}_6]^{3-}$ to $[\text{Ir}^{\text{IV}}\text{Cl}_6]^{2-}$. The careful control of the $[\text{Ir}^{\text{IV}}\text{Cl}_6]^{2-}$ and $[\text{Ir}^{\text{III}}\text{Cl}_6]^{3-}$ species in a mixed PGM sample is of critical importance for efficient separation of Pt, Ir and Rh. Therefore, a clear understanding of the redox processes taking place in such a mixed PGM solution is imperative.

1.3. Redox chemistry to consider in a mixture of Ir, Pt, and ClO_3^-

In industry the oxidation states of the respective PGM complexes are manipulated by rigorously controlling the oxidative potential of the solution. This is done by the addition of ClO_3^- to the mixed PGM solution. In the presence of ClO_3^- the $[\text{Pt}^{\text{II}}\text{Cl}_4]^{2-}$ complex will oxidize to *trans*- $[\text{Pt}^{\text{IV}}\text{Cl}_4(\text{H}_2\text{O})_2]$ at a rate of $k_b = 4.25 \times 10^{-3} \text{ M}^{-1}\cdot\text{sec}^{-1}$.¹⁵ The $[\text{Ir}^{\text{III}}\text{Cl}_6]^{3-}$ complex will also be oxidized by ClO_3^- to form $[\text{Ir}^{\text{IV}}\text{Cl}_6]^{2-}$ at a rate of $k_a = 8.25 \times 10^{-5} \text{ M}^{-1}\cdot\text{sec}^{-1}$.¹⁶ Furthermore, in 1968 Halpern and Pribanic have reported that a redox reaction between $[\text{Pt}^{\text{II}}\text{Cl}_4]^{2-}$ and $[\text{Ir}^{\text{IV}}\text{Cl}_6]^{2-}$ to form $[\text{Pt}^{\text{IV}}\text{Cl}_6]^{2-}$ and $[\text{Ir}^{\text{III}}\text{Cl}_6]^{3-}$ occurs in acidic matrices (k_c).¹⁷ However, no information regarding the kinetics and thermodynamics of this reaction was reported. The possible redox reactions that can take place in a sample containing $[\text{Ir}^{\text{III}}\text{Cl}_6]^{3-}$, $[\text{Pt}^{\text{II}}\text{Cl}_4]^{2-}$ and ClO_3^- are illustrated in Scheme 1.2. In light of the above it is of considerable interest to determine the $[\text{Pt}^{\text{II}}\text{Cl}_4]^{2-}$ and $[\text{Ir}^{\text{IV}}\text{Cl}_6]^{2-}$ redox kinetics to evaluate how the rate of formation of Ir^{IV} and Pt^{IV} will be affected.



Scheme 1.2: A Schematic representation of the redox reactions that can occur in a sample containing $[\text{Ir}^{\text{III}}\text{Cl}_6]^{3-}$, $[\text{Pt}^{\text{II}}\text{Cl}_4]^{2-}$ and ClO_3^- .

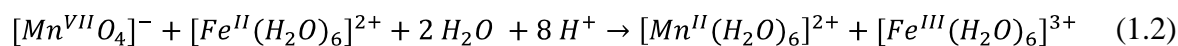
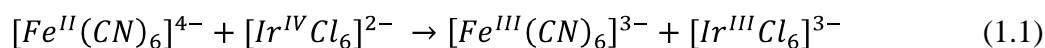
1.4. Objectives of this study

In order to evaluate the rate of Ir^{IV} and Pt^{IV} species formation during ClO₃⁻ oxidation of a mixed [Pt^{II}Cl₄]²⁻ and [Ir^{III}Cl₆]³⁻ solution in acidic matrices this project will focus on the investigation of the redox reaction between [Ir^{IV}Cl₆]²⁻ and [Pt^{II}Cl₄]²⁻. The specific aims of this project is listed below.

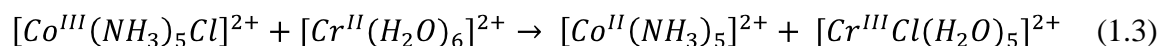
- Determination of the standard reaction Gibbs energy (ΔG_{rxn}^0) or equilibrium constant (K_{eq}) for the redox reaction between [Pt^{II}Cl₄]²⁻ and [Ir^{IV}Cl₆]²⁻.
- Obtain kinetic data for the redox reaction of [Pt^{II}Cl₄]²⁻ and [Ir^{IV}Cl₆]²⁻ in acidic, chloride rich matrices at varying reagent concentrations, ionic strengths and temperatures in order to derive and validate a suitable reaction rate model.
- Determination of the enthalpy-, entropy- and Gibbs energy of activation (ΔH^\ddagger , ΔS^\ddagger and ΔG^\ddagger) to obtain information regarding the mechanism of the redox reaction between [Pt^{II}Cl₄]²⁻ and [Ir^{IV}Cl₆]²⁻.
- The development of a chromatographic system for sufficient separation of [Ir^{IV}Cl₆]²⁻, [Pt^{II}Cl₄]²⁻, [Pt^{IV}Cl₆]²⁻, [Ir^{III}Cl₆]³⁻ and their respective aquation products to investigate which species form during the redox reaction of [Pt^{II}Cl₄]²⁻ and [Ir^{IV}Cl₆]²⁻.

1.5. Background on electron transfer processes in transition metal chemistry

There are two main classes of electron transfer processes, electron-exchange depicted as Reaction 1.1 and general redox reactions, *e.g.* Reaction 1.2. Electron-exchange reactions occur *via* two mechanisms, namely outer- and inner sphere.¹⁸ In an outer sphere electron-exchange reaction, only the charge of the complex changes with no bond formation or bond dissociation taking place. A good example of such an outer sphere electron-exchange reaction is the reaction between $[\text{Ir}^{\text{IV}}\text{Cl}_6]^{2-}$ and $[\text{Fe}^{\text{II}}(\text{CN})_6]^{4-}$, Reaction 1.1, where the electron-exchange rate is approximately 150 times larger than the ligand exchange rates at 298.1 K.¹⁸



Electron-exchange reactions can also proceed *via* an inner sphere mechanism. Inner sphere mechanisms comprise of the formation of an intermediate species from the two reagent complexes by means of a bridging ligand. Electron transfer occurs through this bridged ligand and in some cases the bridging ligand is also transferred, Reaction 1.3.¹⁹



The energy profile of electron-exchange processes proceeds through a transition state with an energy maximum, Figure 1.3. The Gibbs free energy of activation (ΔG^\ddagger) can be used to distinguish between inner- and outer sphere electron transfer processes and is given in Equation 1.4. The first term ($RT \ln(\frac{k_B T}{hZ})$) represents the loss of motional energy during the formation of the transition state and the ΔG_a^\ddagger term corresponds to the attraction or repulsion of the reactants.¹⁸ ΔG_o^\ddagger represents the change in energy caused by the rearrangement of the outer solvation sphere, whereas ΔG_i^\ddagger is defined as the change in energy for the rearrangement of the first- or inner coordination sphere (ligands). In outer sphere reactions, ΔG_i^\ddagger will be close to zero since the first coordination sphere does not rearrange during electron exchange and ΔG_o^\ddagger will predominate ΔG^\ddagger , *e.g.* Reaction 1.1. However, in inner sphere reactions the first coordination sphere rearranges, *e.g.* Reaction 1.3, and ΔG_i^\ddagger is the major contributing

term to ΔG^\ddagger . The ΔG_a^\ddagger term will contribute significantly to the ΔG^\ddagger in reactions with analytes of the same charge, *e.g.* Reactions 1.1 and 1.3.¹⁸

$$\Delta G^\ddagger = RT \ln \left(\frac{k_B T}{h Z} \right) + \Delta G_a^\ddagger + \Delta G_o^\ddagger + \Delta G_i^\ddagger \quad (1.4)$$

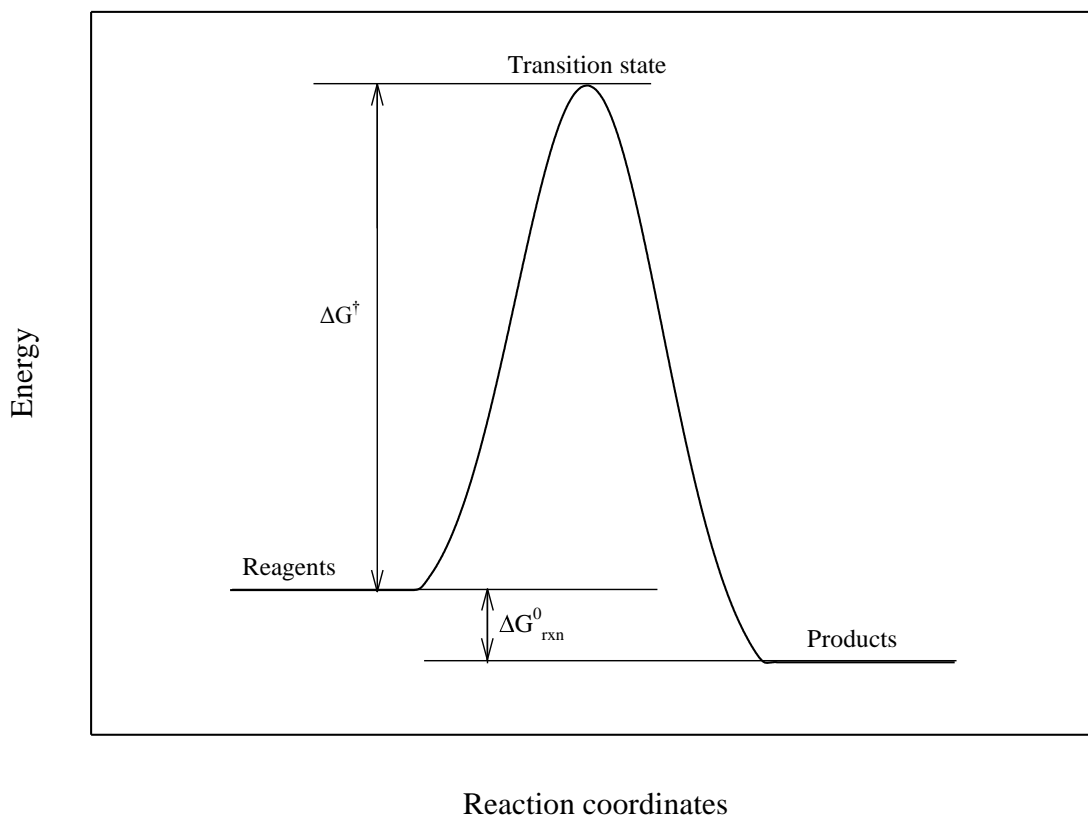


Figure 1.3: The energy profile of any spontaneous electron-exchange reaction showing the standard reaction Gibbs energy (ΔG_{rxn}^0) and Gibbs energy of activation (ΔG^\ddagger).

Several theories to analyse electron transfer reactions have been established and will be discussed:

1.5.1. Eyring's transition state theory

In 1935 Henry Eyring developed Transition State Theory (also referred to as activated complex theory) and this theory is considered as a significant improvement on the Arrhenius equation.²⁰ In contrast to the Arrhenius equation, activated complex theory assumes the existence of a quasi-equilibrium between the reactant species and activated complex, $[AB]^\ddagger$,

Reaction 1.5 and Equation 1.6.²¹ Moreover, activated complex theory states that the activated complex $[AB]^\ddagger$ is a stable molecular state. Activated complex theory allows for the calculation of the enthalpy of activation (ΔH^\ddagger) and entropy of activation (ΔS^\ddagger), which can be used to calculate the Gibbs energy of activation (ΔG^\ddagger), Equation 1.7. Determination of ΔH^\ddagger and ΔS^\ddagger results in a better understanding of how reactions occur. A schematic representation of the reaction energy profile as described by the activated complex theory is given in Figure 1.4.^{21,22}



$$K^\ddagger = e^{\left(\frac{\Delta S^\ddagger}{R}\right)} e^{-\left(\frac{\Delta H^\ddagger}{RT}\right)} \quad (1.6)$$

$$\Delta G^\ddagger = \Delta H^\ddagger - T\Delta S^\ddagger \quad (1.7)$$

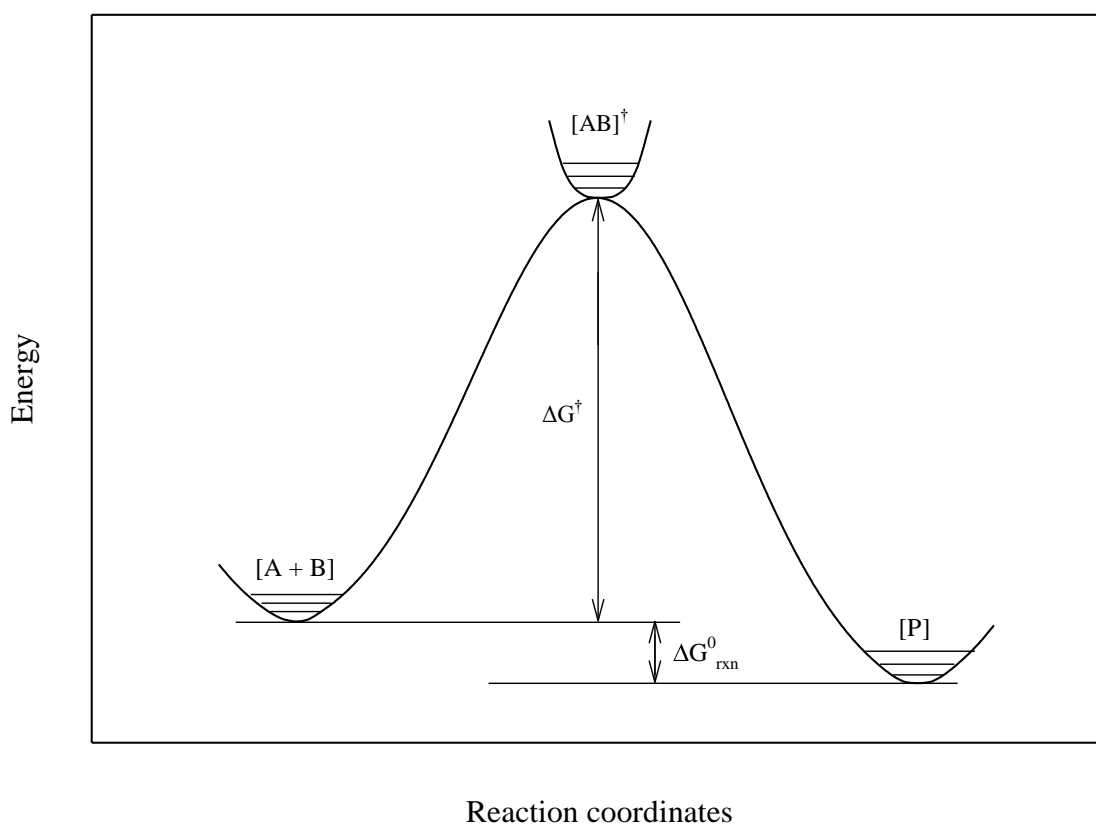


Figure 1.4: The energy profile of any spontaneous electron-exchange reaction as described by Transition State Theory showing the standard reaction Gibbs energy (ΔG_{rxn}^0) and Gibbs energy of activation (ΔG^\ddagger). Transition State Theory assumes that the activated complex ($[AB]^\ddagger$) is a stable molecular state.

1.5.2. Marcus theory

Marcus theory was developed by Rudolph A. Marcus, starting in 1956, in order to understand outer sphere electron-exchange reactions.²³ This theory was later extended to include inner sphere reactions.²⁴ In contrast to Eyring's transition state theory, Marcus theory states that the activated complex is defined by weak interactions between the reagent molecules and the outer coordination sphere and therefore the theory does not interpret the transition state as a stable molecular state, Figure 1.5. The reaction is driven by the vibrational mode of the reagents in the reaction coordinate and the existence of a lower energy pathway results in the formation of the products. Furthermore, Marcus theory demonstrates the importance of solvent interactions and defines the Gibbs energy of activation (ΔG^\ddagger) as a function of solvent polarization, Equation 1.8, where the reorganization term (λ) is defined as the sum of the outer coordination sphere rearrangement (λ_o) and the vibrational term of the inner coordination sphere (λ_i), Equation 1.9.²⁵

$$\Delta G^\ddagger = \frac{\lambda}{4} \left(1 + \frac{\Delta G_{rxn}^0}{\lambda} \right)^2 \quad (1.8)$$

$$\lambda = \lambda_o + \lambda_i \quad (1.9)$$

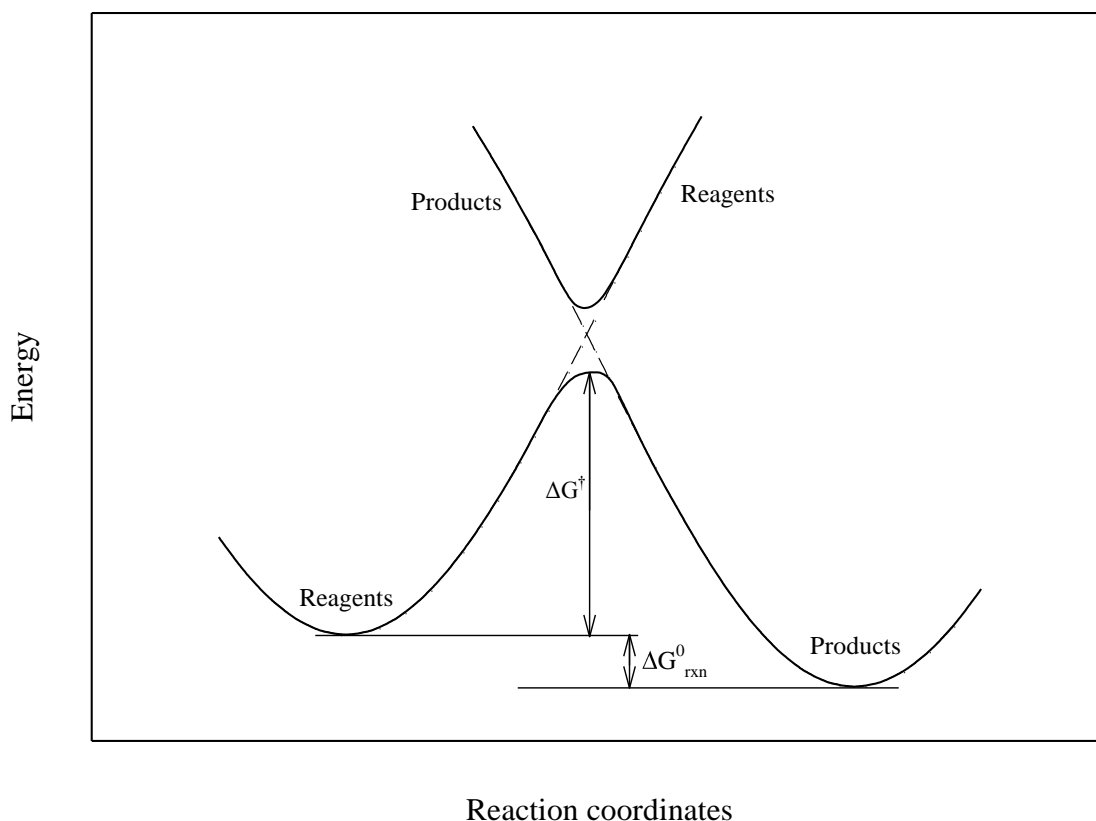


Figure 1.5: The energy profile of any spontaneous electron-exchange reaction showing the standard reaction Gibbs energy ($\Delta G^{\circ}_{\text{rxn}}$) and Gibbs energy of activation (ΔG^{\ddagger}) as represented by the Marcus theory.

In outer sphere reactions λ_o is the major contributing term and the ΔG^{\ddagger} is predominantly determined by solvent rearrangement in the outer coordination sphere, whereas in inner sphere reactions λ_i predominates and the ΔG^{\ddagger} is determined by the internal vibration of the first coordination sphere of the activated complex. This internal vibration of the activation state dictates whether the formation of the products or the dissociation back to the reagents will occur.

1.6. Description of Equikin, for the simulation of the kinetic rate model

An in-house developed program, *Equikin* (Visual Basic 6), will be implemented for the simulation of the proposed reaction rate model to the kinetic data.^{26,27} The program was originally developed for the analysis of $[\text{Rh}^{\text{III}}\text{Cl}_6]^{3-}$ aquation, however was extended to include the redox reaction of $[\text{Ir}^{\text{IV}}\text{Cl}_6]^{2-}$ and $[\text{Pt}^{\text{II}}\text{Cl}_4]^{2-}$. *Equikin* comprises of two main components working in tandem, a routine that integrates the differential rate equations by

means of a Runge-Kutta algorithm²⁸, and a Simplex algorithm²⁹ routine that carries out the non-linear least-squares fitting to the experimental data. The Runge-Kutta method used for the integration of the rate equations is equivalent to a 4th order Taylor method. These two methods differ in that the differential function is not differentiated four times with the Runge-Kutta method, resulting in the added advantage that less computational power is required. For simplicity an Euler method algorithm (1st order Taylor method) is illustrated by Equations 1.10 – 1.15. The Simplex method was used for minimization of the least-squares error between the calculated and experimental data. When the calculated rate constants are updated during a Simplex routine iteration, a constant in the Runge-Kutta routine has also changed. Therefore, the integration routine must recalculate the theoretical concentrations for the species with the updated rate constants. The iteration cycles termination is controlled by set input value in the interface of *Equikin*. This value is indicative of rate constants or molar extinction coefficients that do not differ for further iterations.

$$\frac{dy}{dt} = f(t_i, w_i) \text{ and } w_a = \alpha \quad (1.10)$$

$$h = \frac{(b-a)}{N} \text{ where } a \leq t \leq b \quad (1.11)$$

$$t_i = a + ih \quad (1.12)$$

$$\text{For } i = 1, 2, \dots, N \quad (1.13)$$

$$w_i = w_{i-1} + hf(t_i, w_i) \quad (1.14)$$

$$t_i = a + ih \quad (1.15)$$

End

Chapter 2

Experimental Procedures and Instrumentation

2

Experimental Procedures and Instrumentation

2.1. Preparation of kinetic samples

All kinetic samples were prepared by combining specified amounts of $[\text{Ir}^{\text{IV}}\text{Cl}_6]^{2-}$ and $[\text{Pt}^{\text{II}}\text{Cl}_4]^{2-}$ in the appropriate matrix (*see* Chapter 3). A water bath was used to regulate the temperature during sample preparation and subsequent analysis. The kinetic samples were covered with an aluminum foil casing to prohibit any ambient light from interacting with the complexes in solution.

2.2. Analytical Instrumentation

2.2.1. UV-Vis spectrophotometer

Ultraviolet-visible (UV-Vis) spectroscopy (GBC Cintra 10e) was used for all kinetic analyses. The spectrophotometer was connected to a water bath for the regulation of temperature during analyses.

2.2.2. Inductively coupled plasma-optical emission spectroscopy (ICP-OES)

An Ametek Spectro Arcos inductively coupled plasma-optical emission spectrometer (ICP-OES) was used for the quantification of Pt and Ir concentrations in all samples prepared for the kinetic experiments. The standard solutions were matrix matched to the acid concentration of the samples.

2.2.3: Ion-pair high pressure liquid chromatography (IP-HPLC)

An Agilent 1260 Infinity high pressure liquid chromatographic (HPLC) system with polydiode array (PDA) detection and a Phenomenex 250 x 4.6 mm column packed with a 5.0 μm C₁₈ stationary phase was used for the separation of $[\text{Ir}^{\text{IV}}\text{Cl}_6]^{2-}$, $[\text{Pt}^{\text{IV}}\text{Cl}_6]^{2-}$, $[\text{Pt}^{\text{II}}\text{Cl}_4]^{2-}$, $[\text{Ir}^{\text{III}}\text{Cl}_6]^{3-}$ and their respective aquation products. Successful separation of PGM chlorido aqua species were achieved through ion-pair liquid chromatography (IP-HPLC) with a high degree of success.^{26,30} The ion-pair chromatographic system utilizes the hydrophobicity and cationic charge of the tetrabutylammonium ions (TBA^+) to form ion-pairs with the anionic PGM complexes for the retention of the anionic complexes on the C₁₈ column. Therefore, the IP-HPLC system is limited to the separation of only the anionic species. With respect to the separation of $[\text{Ir}^{\text{IV}}\text{Cl}_6]^{2-}$, $[\text{Pt}^{\text{IV}}\text{Cl}_6]^{2-}$, $[\text{Pt}^{\text{II}}\text{Cl}_4]^{2-}$, $[\text{Ir}^{\text{III}}\text{Cl}_6]^{3-}$ and their respective aquation products an IP-HPLC method was developed. The mobile phase comprised of mixing HPLC grade acetonitrile with 15 mM TBA^+Cl^- acetate buffer solution at a pH of 4 from different reservoirs. The isocratic separation of a sample containing $[\text{Ir}^{\text{IV}}\text{Cl}_6]^{2-}$, $[\text{Pt}^{\text{IV}}\text{Cl}_6]^{2-}$, $[\text{Pt}^{\text{II}}\text{Cl}_4]^{2-}$, $[\text{Ir}^{\text{III}}\text{Cl}_6]^{3-}$ and their respective aquation products was carried out at varying concentrations of acetonitrile for optimization of the mobile phase composition Figure 2.1. A decrease in the acetonitrile concentration (increase in the TBA^+Cl^- concentration) results in an increased separation efficiency of the PGM species. At acetonitrile concentrations above 50 % the $[\text{Pt}^{\text{IV}}\text{Cl}_5(\text{H}_2\text{O})]^-$ and $[\text{Pt}^{\text{II}}\text{Cl}_4]^{2-}$ species co-elute and the acetonitrile concentration must be 50 % or lower to obtain separation of these two species. However, it was found that the separation efficiency of $[\text{Ir}^{\text{III}}\text{Cl}_6]^{3-}$ and $[\text{Pt}^{\text{IV}}\text{Cl}_5(\text{H}_2\text{O})]^-$ decreases as the acetonitrile concentration is decreased. Therefore, an acetonitrile concentration of 46 % was used to separate the $[\text{Ir}^{\text{III}}\text{Cl}_6]^{3-}$, $[\text{Pt}^{\text{IV}}\text{Cl}_5(\text{H}_2\text{O})]^-$ and $[\text{Pt}^{\text{II}}\text{Cl}_4]^{2-}$ species. Furthermore, at mobile phase conditions below 50 % acetonitrile precipitation of $[\text{Ir}^{\text{IV}}\text{Cl}_6]^{2-}$ occurs on the guard column and is further discussed in chapter 4.4.3. In order to decrease analysis time a mobile phase gradient was used as shown in Figure 2.2.

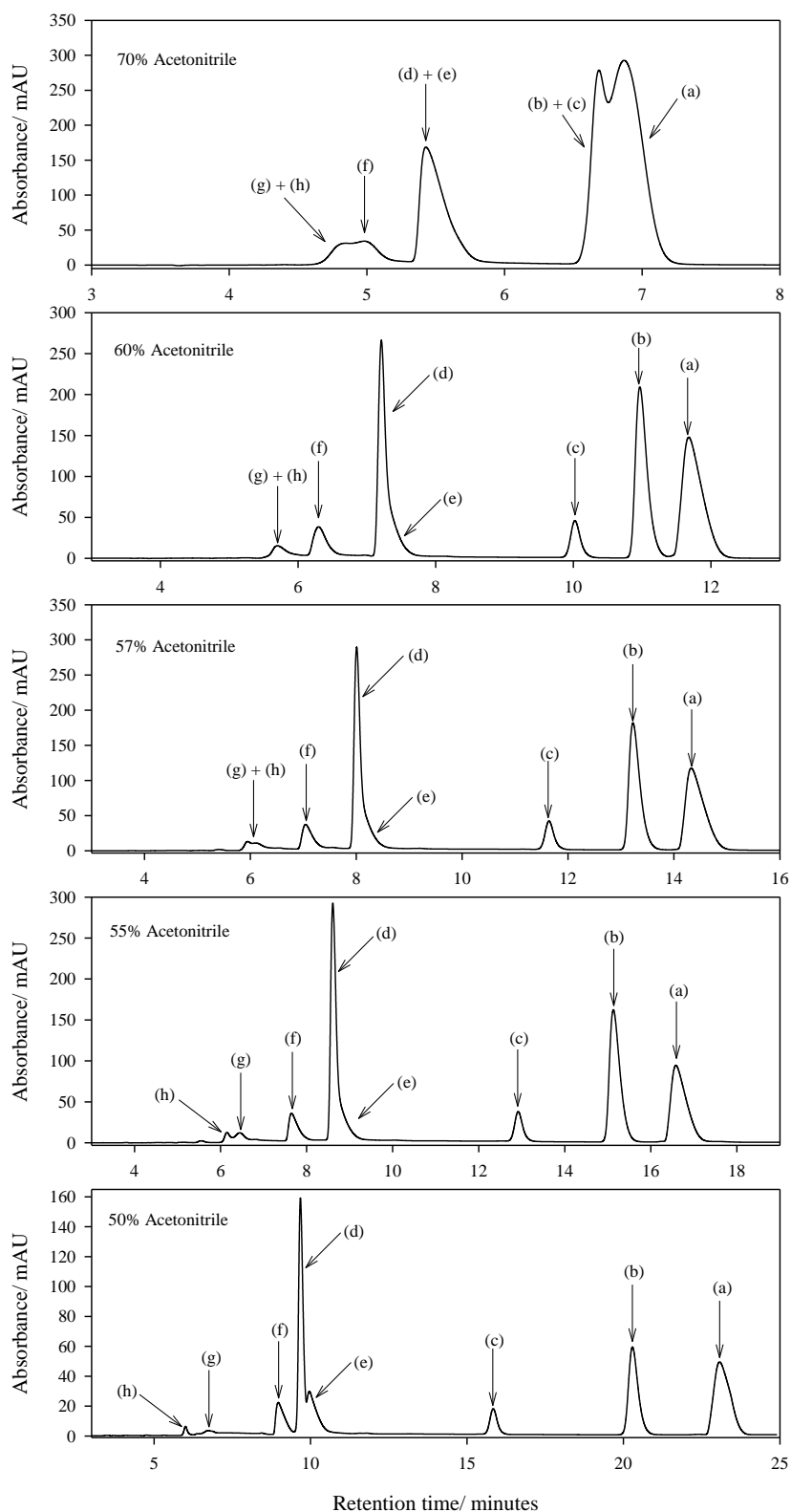


Figure 2.1: Chromatographic trace of a sample containing $[\text{Ir}^{\text{IV}}\text{Cl}_6]^{2-}$, $[\text{Pt}^{\text{IV}}\text{Cl}_6]^{2-}$, $[\text{Pt}^{\text{II}}\text{Cl}_4]^{2-}$, $[\text{Ir}^{\text{III}}\text{Cl}_6]^{3-}$ and their respective aquation products at varying acetonitrile concentrations. (a) $[\text{Ir}^{\text{IV}}\text{Cl}_6]^{2-}$, (b) $[\text{Pt}^{\text{IV}}\text{Cl}_6]^{2-}$, (c) unknown Pt^{IV} species, (d) $[\text{Pt}^{\text{IV}}\text{Cl}_5(\text{H}_2\text{O})]^-$, (e) $[\text{Pt}^{\text{II}}\text{Cl}_4]^{2-}$, (f) $[\text{Ir}^{\text{III}}\text{Cl}_6]^{3-}$, (g) $[\text{Ir}^{\text{III}}\text{Cl}_5(\text{H}_2\text{O})]^{2-}$, (h) $[\text{Ir}^{\text{III}}\text{Cl}_4(\text{H}_2\text{O})_2]^-$.

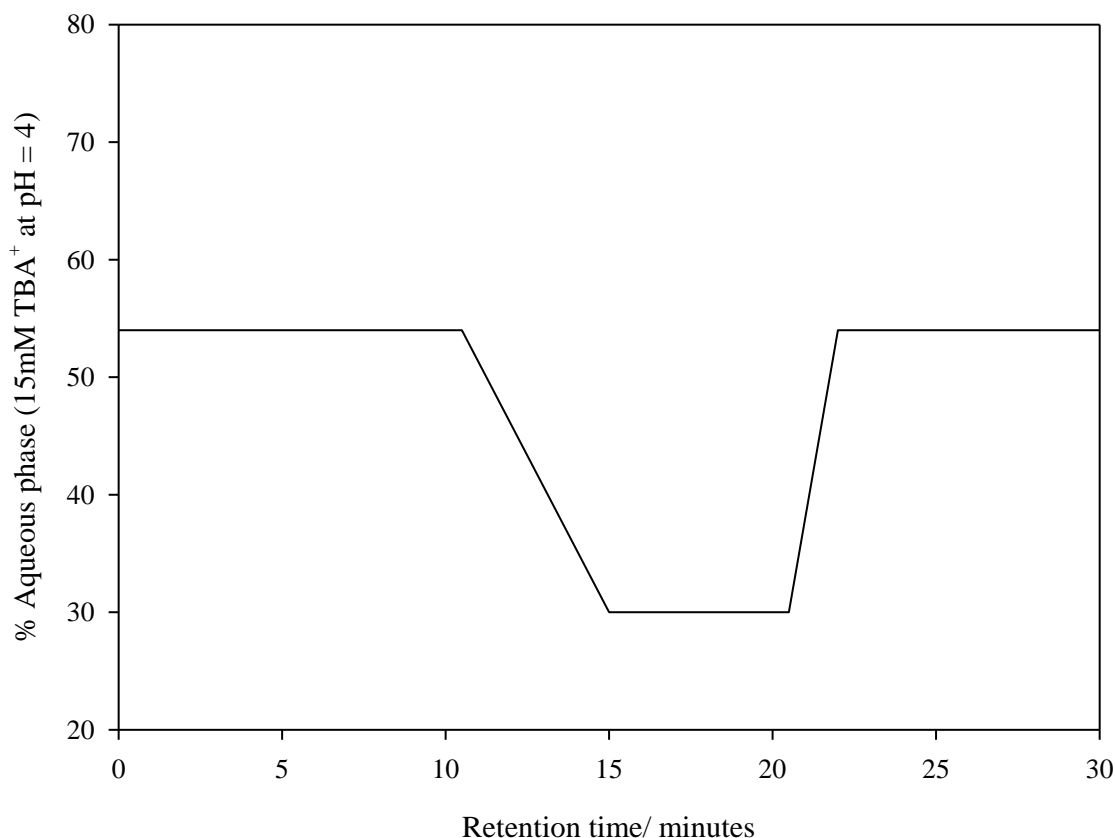


Figure 2.2: Mobile phase gradient employed for the IP-HPLC separation of $[\text{Ir}^{\text{IV}}\text{Cl}_6]^{2-}$, $[\text{Pt}^{\text{II}}\text{Cl}_4]^{2-}$, $[\text{Pt}^{\text{IV}}\text{Cl}_6]^{2-}$, $[\text{Ir}^{\text{III}}\text{Cl}_6]^{3-}$ and their respective aquated products.

The chromatographic analysis of $[\text{Ir}^{\text{III}}\text{Cl}_6]^{3-}$ aquation was carried out with a similar IP-HPLC setup. A Varian Polaris HPLC equipped with a Varian Polaris solvent delivery system (Model 210) and a Varian Polaris autosampler (Model 410) was used. Reverse phase (C_{18}) silica particles with an average particle diameter of 50 μm were packed into a 250 x 4.6 mm column *via* Kirkland's fill-tap method.³¹ This column was used for the separation of the $[\text{IrCl}_n(\text{H}_2\text{O})_{6-n}]^{3-n}$ ($n = 4-6$) series of complex anions (*see* Chapter 4.2.4). Sufficient separation of the $[\text{IrCl}_n(\text{H}_2\text{O})_{6-n}]^{3-n}$ ($n = 4-6$) species were achieved using an isocratic method with the mobile phase consisting of a 5mM TBA⁺ solution in 46 % acetonitrile. A Varian Polaris dual wavelength UV-Vis detector was coupled to the outlet of the column for detection of the analytes.

2.2.4. Electrospray ionization mass spectrometry (ESI MS)

The direct infusion electrospray ionization mass spectrometry (ESI MS) analysis of $[\text{Pt}^{\text{IV}}\text{Cl}_6]^{2-}$ was carried out on a Synapt G2 quadrupole time-of-flight mass spectrometer (Waters, Milford, MA, USA) in the negative mode (*see* Chapter 3.6). A capillary voltage of 2.5 kV with changing cone voltages (15 - 100 V) were used, (desolvation temperature = 275°C and desolvation gas (N_2) flow rate = 650 $\text{L}\cdot\text{h}^{-1}$).

2.3. Materials

The PGM chlorido salts used in this study ($\text{Na}_2\text{IrCl}_6\cdot 6\text{H}_2\text{O}$, $\text{K}_2\text{PtCl}_4\cdot x\text{H}_2\text{O}$, $\text{Na}_2\text{PtCl}_6\cdot 6\text{H}_2\text{O}$ and $\text{K}_3\text{IrCl}_6\cdot x\text{H}_2\text{O}$) were obtained from Sigma-Aldrich and Johnson Matthey. The purity of the PGM chlorido salts were verified with UV-Vis spectroscopy (*see* Chapter 3.2). HCl, HClO_4 , NaCl and NaClO_4 were acquired from Sigma-Aldrich and were used for the modification of the sample matrices during the kinetic investigations. HPLC grade acetonitrile and tetrabutyl ammoniumchloride (TBA^+Cl^-) were obtained from Sigma-Aldrich and were used for the preparation of mobile phases for the IP-HPLC analyses (*see* Chapter 2.3.3). Only Milli-Q water (0.22 μm membrane filter, 18 Ω) was used during the preparation of samples and mobile phases.

Chapter 3

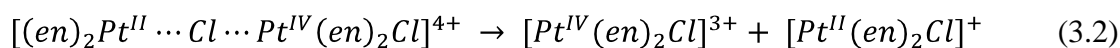
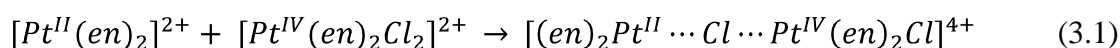
A detailed kinetic investigation of the oxidation of $[\text{Pt}^{\text{II}}\text{Cl}_4]^{2-}$
by $[\text{Ir}^{\text{IV}}\text{Cl}_6]^{2-}$

3

A detailed kinetic investigation of the oxidation of $[\text{Pt}^{\text{II}}\text{Cl}_4]^{2-}$ by $[\text{Ir}^{\text{IV}}\text{Cl}_6]^{2-}$

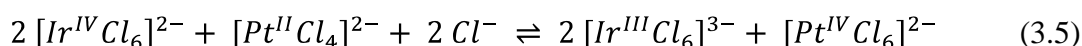
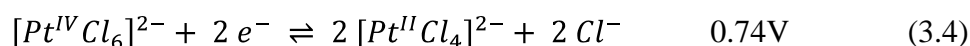
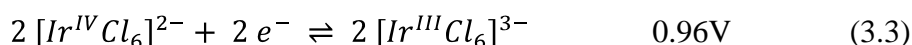
3.1. Introduction

Several investigations³²⁻³⁶ have shown that the rate of ligand exchange reactions with respect to Pt^{IV} complexes is significantly enhanced by the presence of Pt^{II} in the reaction mixture. In 1954, Rich and Taube proposed that the ligand exchange reaction between $[\text{Pt}^{\text{II}}\text{Cl}_4]^{2-}$ and $[\text{Pt}^{\text{IV}}\text{Cl}_6]^{2-}$ is catalysed by a Pt^{III} intermediate.³⁶ Evidence for the existence of such a Pt^{III} species in the form of a chlorido complex was found when $[\text{Pt}^{\text{IV}}\text{Cl}_6]^{2-}$ was reduced to $[\text{Pt}^{\text{II}}\text{Cl}_4]^{2-}$, by means of laser flash photolysis.³⁷ However, the mechanism proposed by Rich and Taube³⁶ came under scrutiny when Basolo and Pearson investigated the chloride exchange of $[\text{Pt}^{\text{IV}}(\text{en})_2\text{Cl}_2]^{2+}$ in the presence of $[\text{Pt}^{\text{II}}(\text{en})_2]^{2+}$, Reactions 3.1 and 3.2.³²⁻³⁴



In contrast to the mechanism proposed by Rich and Taube³⁶, Basolo and Pearson proposed the formation of a halide bridged intermediate complex that dissociates *via* a transfer of chloride and 2 electrons. In this process Pt^{II} is oxidized to Pt^{IV} and Pt^{IV} is reduced to Pt^{II} . The reaction mechanism proposed by Basolo and Pearson³²⁻³⁴ is now generally accepted and is not catalytic in nature but rather a redox reaction between Pt^{II} and Pt^{IV} .

In a subsequent study conducted by Taube³⁶, it was mentioned that the ligand exchange rate of $[\text{Pt}^{\text{IV}}\text{Cl}_6]^{2-}$ in the presence of $[\text{Pt}^{\text{II}}\text{Cl}_4]^{2-}$ is significantly slower when $[\text{Ir}^{\text{IV}}\text{Cl}_6]^{2-}$ is also present, with no explanation given. However, combination of the two reduction half reactions for $[\text{Ir}^{\text{IV}}\text{Cl}_6]^{2-}$ and $[\text{Pt}^{\text{IV}}\text{Cl}_6]^{2-}$, Reactions 3.3 and 3.4, yields Reaction 3.5 from which the standard reaction Gibbs energy (ΔG^0_{rxn}) can be calculated using Equation 3.6. From the relative large negative $\Delta G^0_{\text{rxn}} = -42.45 \text{ kJ}\cdot\text{mol}^{-1}$ ($K_{\text{eq}} = 2.73 \times 10^7$) it can be inferred that Ir^{IV} will be spontaneously reduced by Pt^{II} to form Ir^{III} . The depletion of the Pt^{II} concentration can therefore account for the above mentioned slower ligand exchange rate of $[\text{Pt}^{\text{IV}}\text{Cl}_6]^{2-}$ in the presence of $[\text{Pt}^{\text{II}}\text{Cl}_4]^{2-}$ observed by Taube.³⁶



$$\Delta G^0_{\text{rxn}} = nFE^0_{\text{Ir}^{\text{IV}}} - nFE^0_{\text{Pt}^{\text{IV}}} = -RT \ln(K_{\text{eq}}) \quad (3.6)$$

Apart from the potential significance of the reaction between $[\text{Pt}^{\text{II}}\text{Cl}_4]^{2-}$ and $[\text{Ir}^{\text{IV}}\text{Cl}_6]^{2-}$ for the PGM refining industry, it is anticipated that this redox reaction might have interesting analogous mechanistic aspects with the mechanisms proposed by both Taube³⁶ and Pearson³²⁻³⁴ for the Pt^{II} - Pt^{IV} system (*vide infra* Chapter 4). We report here a detailed kinetic study concerning the reduction of $[\text{Ir}^{\text{IV}}\text{Cl}_6]^{2-}$ by $[\text{Pt}^{\text{II}}\text{Cl}_4]^{2-}$ in well-defined acidic aqueous matrices with the aim of establishing whether a Pt^{III} intermediate forms during the conversion of Ir^{IV} to Ir^{III} and Pt^{II} to Pt^{IV} , and to ascertain how this reaction will influence the ClO_3^- oxidation scheme shown in Scheme 1.2.

3.2. UV-Vis characterization of the pure reagents ($[\text{Ir}^{\text{IV}}\text{Cl}_6]^{2-}$ and $[\text{Pt}^{\text{II}}\text{Cl}_4]^{2-}$) and products ($[\text{Ir}^{\text{III}}\text{Cl}_6]^{3-}$ and $[\text{Pt}^{\text{IV}}\text{Cl}_6]^{2-}$)

Individual solutions of $[\text{Ir}^{\text{IV}}\text{Cl}_6]^{2-}$, $[\text{Pt}^{\text{II}}\text{Cl}_4]^{2-}$, $[\text{Pt}^{\text{IV}}\text{Cl}_6]^{2-}$ and $[\text{Ir}^{\text{III}}\text{Cl}_6]^{3-}$ were prepared by dissolving the respective salts ($\text{Na}_2\text{IrCl}_6 \cdot 6\text{H}_2\text{O}$, $\text{K}_2\text{PtCl}_4 \cdot x\text{H}_2\text{O}$, $\text{Na}_2\text{PtCl}_6 \cdot 6\text{H}_2\text{O}$, $\text{K}_3\text{IrCl}_6 \cdot x\text{H}_2\text{O}$) in a 6.0 M HCl matrix. The relatively high HCl matrix is necessary to

suppress aquation reactions. All metal ions were standardized by means of ICP-OES analysis and the UV-Vis spectra for these solutions were recorded in the wavelength range from 200 - 700 nm, Figure 3.1 (a) - (d).

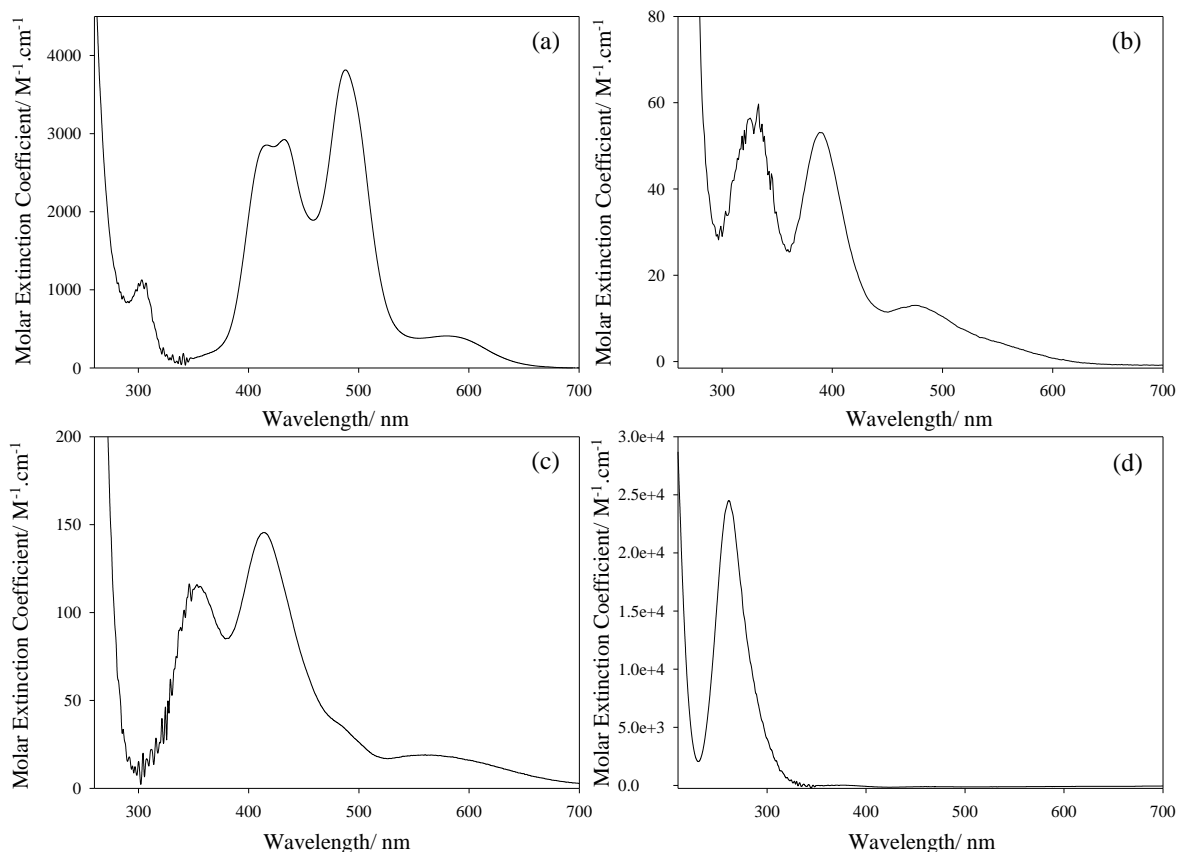


Figure 3.1: Molar extinction coefficient plots of the species; (a) $[\text{Ir}^{\text{IV}}\text{Cl}_6]^{2-}$, (b) $[\text{Pt}^{\text{II}}\text{Cl}_4]^{2-}$, (c) $[\text{Ir}^{\text{III}}\text{Cl}_6]^{3-}$ and (d) $[\text{Pt}^{\text{IV}}\text{Cl}_6]^{2-}$, all in a 6.0 M HCl matrix

The molar extinction coefficients determined for the $[\text{Ir}^{\text{IV}}\text{Cl}_6]^{2-}$, $[\text{Pt}^{\text{II}}\text{Cl}_4]^{2-}$, $[\text{Pt}^{\text{IV}}\text{Cl}_6]^{2-}$ and $[\text{Ir}^{\text{III}}\text{Cl}_6]^{3-}$ complexes compare well to those reported in literature at selected peak maxima, Table 3.1, except for $[\text{Ir}^{\text{III}}\text{Cl}_6]^{3-}$.³⁸⁻⁴⁰ The slightly higher molar extinction coefficient of $[\text{Ir}^{\text{III}}\text{Cl}_6]^{3-}$ at 413 nm may be due to the presence of Ir^{IV} . However, after the addition of hydrazine the same molar extinction coefficient was obtained.

Table 3.1: Summary of the molar extinction coefficients of species represented in Figure 3.1 (a) - (b). Molar extinction coefficients at selected peak maxima and 488 nm are reported

Chemical Species	Molar extinction coefficient at peak maximum/ $\text{M}^{-1}\cdot\text{cm}^{-1}$	Molar extinction coefficient as reported in literature/ $\text{M}^{-1}\cdot\text{cm}^{-1}$	wavelength of peak maximum/ nm	Molar extinction coefficient at 488 nm/ $\text{M}^{-1}\cdot\text{cm}^{-1}$
$[\text{Ir}^{\text{IV}}\text{Cl}_6]^{2-}$	3920 ± 23	3905 ³⁸	488	3920
$[\text{Pt}^{\text{II}}\text{Cl}_4]^{2-}$	57 ± 4	56 ³⁹	395	16
$[\text{Ir}^{\text{III}}\text{Cl}_6]^{3-}$	145 ± 26	90 ³⁸	413	33
$[\text{Pt}^{\text{IV}}\text{Cl}_6]^{2-}$	24349 ± 57	26062 ⁴⁰	262	< 1

The molar extinction coefficients of $[\text{Pt}^{\text{II}}\text{Cl}_4]^{2-}$, $[\text{Pt}^{\text{IV}}\text{Cl}_6]^{2-}$ and $[\text{Ir}^{\text{III}}\text{Cl}_6]^{3-}$ are significantly smaller compared to the molar extinction coefficient of $[\text{Ir}^{\text{IV}}\text{Cl}_6]^{2-}$ at 488 nm, Table 3.1. If equal quantities of each of the four species are present in a sample, the $[\text{Ir}^{\text{IV}}\text{Cl}_6]^{2-}$ species absorbance will account for 98.7 % of the total absorbance at 488 nm. The absorbance contribution from the remaining 3 species ($[\text{Pt}^{\text{II}}\text{Cl}_4]^{2-}$, $[\text{Pt}^{\text{IV}}\text{Cl}_6]^{2-}$ and $[\text{Ir}^{\text{III}}\text{Cl}_6]^{3-}$) is thus negligible^a and allows for the ‘direct’ determination of the $[\text{Ir}^{\text{IV}}\text{Cl}_6]^{2-}$ species concentration as the redox reaction progresses with time at 488 nm.

3.3. UV-Vis spectral changes for the redox reaction of $[\text{Pt}^{\text{II}}\text{Cl}_4]^{2-}$ and $[\text{Ir}^{\text{IV}}\text{Cl}_6]^{2-}$ as a function of time and reaction stoichiometry

The redox reaction of $[\text{Ir}^{\text{IV}}\text{Cl}_6]^{2-}$ and $[\text{Pt}^{\text{II}}\text{Cl}_4]^{2-}$ was initiated by the addition of 0.122 mM $[\text{Pt}^{\text{II}}\text{Cl}_4]^{2-}$ to 0.202 mM $[\text{Ir}^{\text{IV}}\text{Cl}_6]^{2-}$ in a 3.0 M HCl matrix. The resulting UV-Vis spectra are shown in Figure 3.2.

^a Especially when the reaction is far from completion.

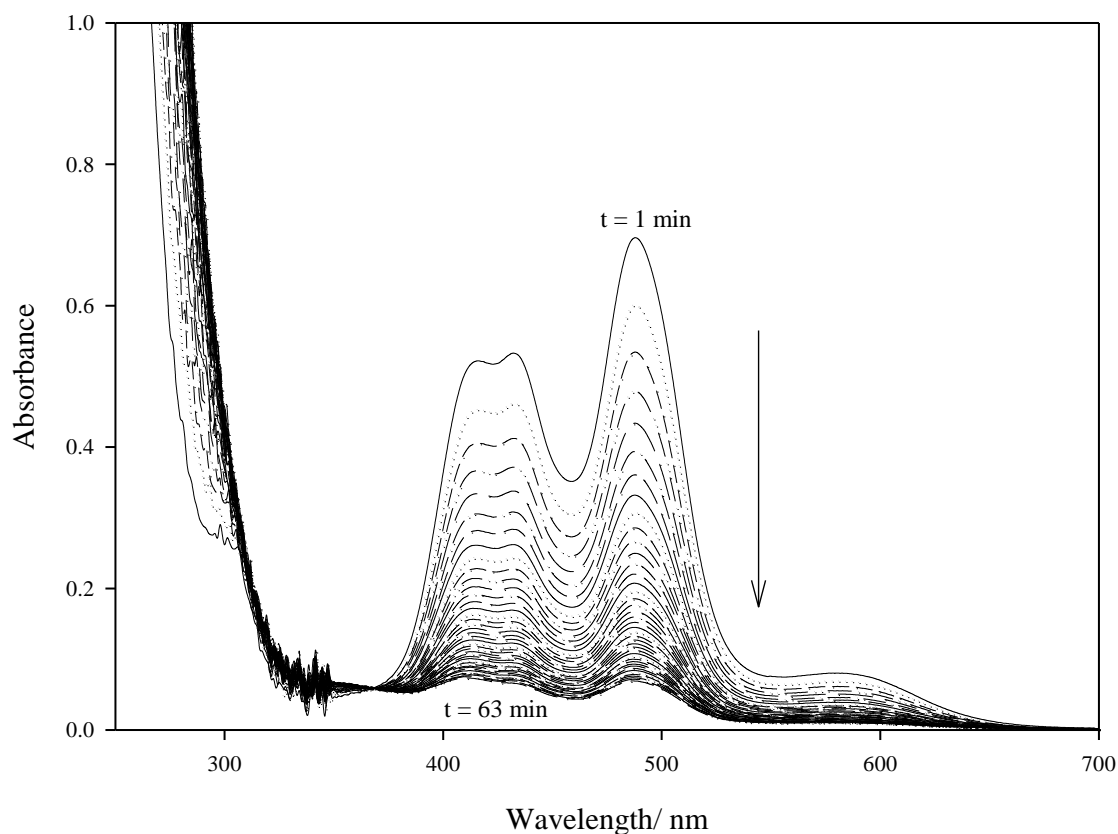


Figure 3.2: Reduction of $[\text{Ir}^{\text{IV}}\text{Cl}_6]^{2-}$ by $[\text{Pt}^{\text{II}}\text{Cl}_4]^{2-}$ observed with UV-Vis spectroscopy, as a function of time. Spectra were recorded every 1.5 minutes.

As the redox reaction progresses the absorbance at 488 nm gradually decreases, indicating the reduction of $[\text{Ir}^{\text{IV}}\text{Cl}_6]^{2-}$ to $[\text{Ir}^{\text{III}}\text{Cl}_6]^{3-}$. Only below 380 nm is an increase in absorbance observed. After 5 hours, the UV-Vis spectrum does not change anymore, indicating that the reaction has gone to completion, *i.e.* equilibrium is reached. The UV-Vis spectrum of a 5 fold dilution of this sample is shown in Figure 3.3. If it is taken into account that the equilibrium constant for this redox reaction is relatively large ($K_{\text{eq}} = 2.73 \times 10^7$), it is a good approximation that the absorbance at 262 nm due to $[\text{Ir}^{\text{IV}}\text{Cl}_6]^{2-}$ and $[\text{Pt}^{\text{II}}\text{Cl}_4]^{2-}$ are negligible, Equations 3.7 and 3.8. Moreover, the molar extinction coefficient of $[\text{Ir}^{\text{III}}\text{Cl}_6]^{3-}$ at 262 nm is equal to $583 \text{ M}^{-1}\cdot\text{cm}^{-1}$ and that of $[\text{Pt}^{\text{IV}}\text{Cl}_6]^{2-}$ is equal to $24349 \text{ M}^{-1}\cdot\text{cm}^{-1}$. It can therefore be approximated that the absorbance due to the $[\text{Ir}^{\text{III}}\text{Cl}_6]^{3-}$ species at 262 nm is about 4.8 % and that of $[\text{Pt}^{\text{IV}}\text{Cl}_6]^{2-}$ approximately 95.2 %.

$$K_{eq} = \frac{[[\text{Ir}^{\text{III}}\text{Cl}_6]^{3-}]^2[\text{Pt}^{\text{IV}}\text{Cl}_6]^{2-}}{[[\text{Ir}^{\text{IV}}\text{Cl}_6]^{2-}]^2[[\text{Pt}^{\text{II}}\text{Cl}_4]^{2-}][\text{Cl}^-]^2} \text{ and } [\text{Cl}^-] = 3.0 \text{ M} \quad (3.7)$$

$$9K_{eq} = \frac{[[\text{Ir}^{\text{III}}\text{Cl}_6]^{3-}]^2[\text{Pt}^{\text{IV}}\text{Cl}_6]^{2-}}{[[\text{Ir}^{\text{IV}}\text{Cl}_6]^{2-}]^2[[\text{Pt}^{\text{II}}\text{Cl}_4]^{2-}]} = 2.46 \times 10^8 \quad (3.8)$$

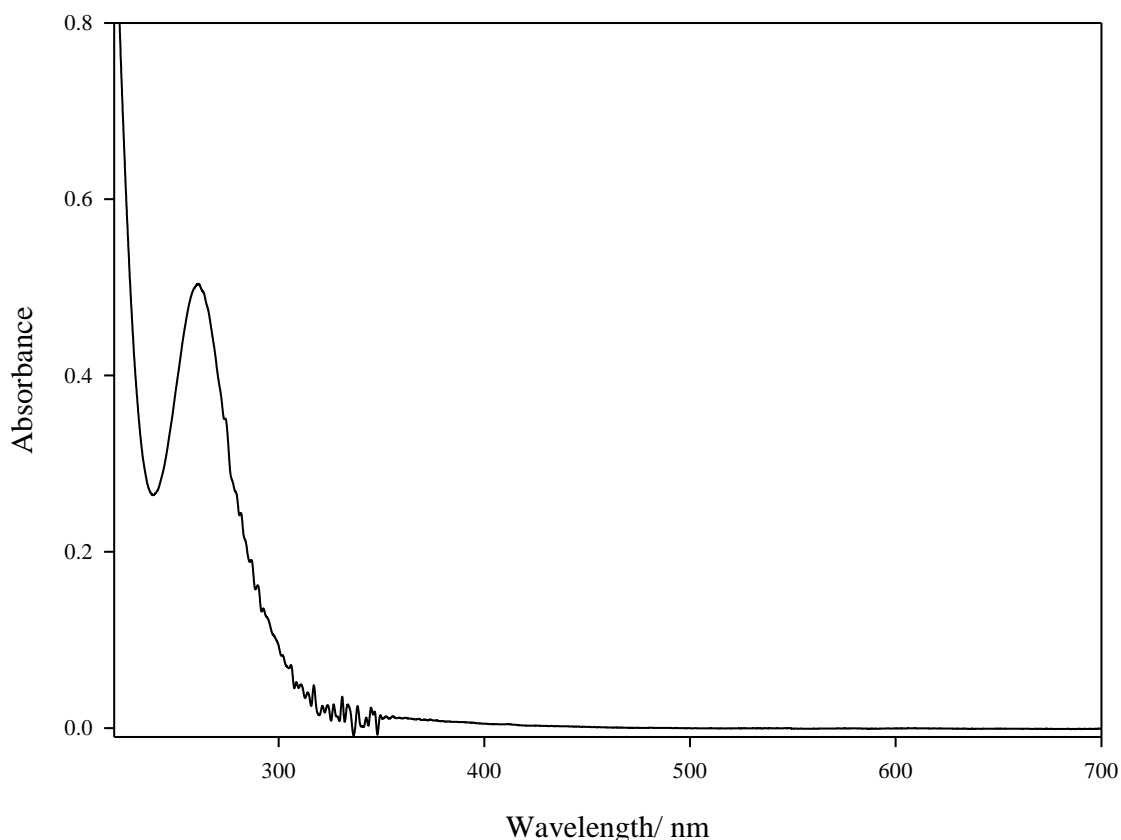


Figure 3.3: UV-Vis spectrum of the reduction of $[\text{Ir}^{\text{IV}}\text{Cl}_6]^{2-}$ by $[\text{Pt}^{\text{II}}\text{Cl}_4]^{2-}$ after a reaction time of 5 hours. The peak at 262 nm, corresponds well with that of $[\text{Pt}^{\text{IV}}\text{Cl}_6]^{2-}$.

The $[\text{Pt}^{\text{IV}}\text{Cl}_6]^{2-}$ concentration after the redox reaction is completed should be 0.101 mM and corresponds to an absorbance at 262 nm equal to 0.492. This compares well with the absorbance of 0.504 obtained experimentally at 262 nm for the reaction sample, Figure 3.3, and illustrates that approximately 0.101 mM of $[\text{Pt}^{\text{IV}}\text{Cl}_6]^{2-}$ formed. The stoichiometry for this redox reaction is therefore $2 [\text{Ir}^{\text{IV}}\text{Cl}_6]^{2-} : 1 [\text{Pt}^{\text{II}}\text{Cl}_4]^{2-}$.

3.4. Kinetic investigation of the redox reaction ($[\text{Pt}^{\text{II}}\text{Cl}_4]^{2-} + [\text{Ir}^{\text{IV}}\text{Cl}_6]^{2-}$)

The kinetic investigation of the redox reaction between $[\text{Ir}^{\text{IV}}\text{Cl}_6]^{2-}$ and $[\text{Pt}^{\text{II}}\text{Cl}_4]^{2-}$ will comprise of varying the reagent concentration, ionic strength and temperature in order to assess how these parameters influence the reaction rate.

3.4.1. Reaction rate as a function of $[\text{Pt}^{\text{II}}\text{Cl}_4]^{2-}$ concentration

In order to evaluate the effect of the $[\text{Pt}^{\text{II}}\text{Cl}_4]^{2-}$ concentration on the redox reaction rate, several samples were prepared that contained the same concentration of $[\text{Ir}^{\text{IV}}\text{Cl}_6]^{2-}$ and HCl (2.73 M) while varying the $[\text{Pt}^{\text{II}}\text{Cl}_4]^{2-}$ concentration, Table 3.2. For each sample the absorbance was recorded as a function of time, at 488 nm, Figure 3.4. Temperature was regulated during the sample preparation and subsequent kinetic runs at 301.1 ± 0.2 K.

Table 3.2: The concentration of $[\text{Ir}^{\text{IV}}\text{Cl}_6]^{2-}$, $[\text{Pt}^{\text{II}}\text{Cl}_4]^{2-}$ and HCl in the prepared samples for the investigation of the reaction rate dependence on $[\text{Pt}^{\text{II}}\text{Cl}_4]^{2-}$ concentration

Concentration of $[\text{Ir}^{\text{IV}}\text{Cl}_6]^{2-}$ / mM	Concentration of $[\text{Pt}^{\text{II}}\text{Cl}_4]^{2-}$ / mM	Concentration of HCl/ M
0.2149	0.0260	2.730
0.2128	0.0456	2.730
0.2143	0.1163	2.730
0.2240	0.2462	2.730
0.2077	0.4644	2.730
0.2167	0.9778	2.730
0.2014	1.4225	2.730

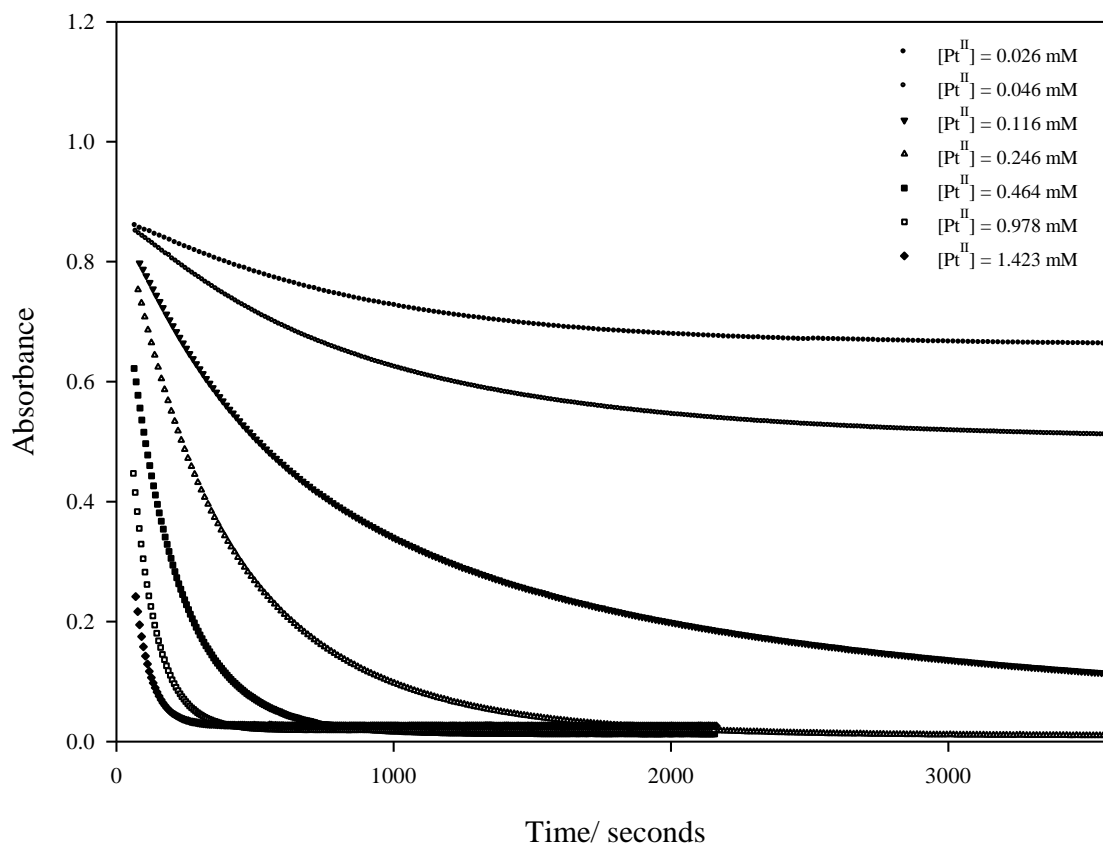


Figure 3.4: UV-Vis absorbance for the redox reaction of $[\text{Ir}^{\text{IV}}\text{Cl}_6]^{2-}$ and $[\text{Pt}^{\text{II}}\text{Cl}_4]^{2-}$ at 488 nm measured as a function of time. The $[\text{Pt}^{\text{II}}\text{Cl}_4]^{2-}$ concentration for each reaction are shown in the legend. $[\text{Ir}^{\text{IV}}\text{Cl}_6]^{2-}$ concentration = 0.213 ± 0.007 mM, HCl concentration = 2.730 M, monitored at a temperature of 301.1 ± 0.2 K

As the concentration of $[\text{Pt}^{\text{II}}\text{Cl}_4]^{2-}$ increases, the rate of the reaction increases. It is therefore clear that the rate of $[\text{Ir}^{\text{IV}}\text{Cl}_6]^{2-}$ reduction is dependent on the $[\text{Pt}^{\text{II}}\text{Cl}_4]^{2-}$ concentration, from which the preliminary rate law can be derived, Equation 3.9. The reaction order (x) with respect to the $[\text{Pt}^{\text{II}}\text{Cl}_4]^{2-}$ concentration must still be evaluated (*vide infra*).

$$\frac{d[\text{Ir}^{\text{IV}}]}{dt} = -k [\text{Pt}^{\text{II}}]^x \quad (3.9)$$

3.4.2. Reaction rate as a function of $[\text{Ir}^{\text{IV}}\text{Cl}_6]^{2-}$ concentration

To evaluate the effect of $[\text{Ir}^{\text{IV}}\text{Cl}_6]^{2-}$ concentration on the reaction rate a series of samples were prepared by keeping the final $[\text{Pt}^{\text{II}}\text{Cl}_4]^{2-}$ and HCl (2.73 M) concentrations constant while varying the $[\text{Ir}^{\text{IV}}\text{Cl}_6]^{2-}$ concentration, Table 3.3. For each sample the absorbance was recorded as a function of time at 488 nm, Figure 3.5. Temperature was regulated during the sample preparation and subsequent kinetic runs at 301.1 ± 0.2 K.

Table 3.3: The concentrations of $[\text{Ir}^{\text{IV}}\text{Cl}_6]^{2-}$, $[\text{Pt}^{\text{II}}\text{Cl}_4]^{2-}$ and HCl in the prepared samples for the investigation of the reaction rate dependence on $[\text{Ir}^{\text{IV}}\text{Cl}_6]^{2-}$ concentration

Concentration of $[\text{Ir}^{\text{IV}}\text{Cl}_6]^{2-}$ / mM	Concentration of $[\text{Pt}^{\text{II}}\text{Cl}_4]^{2-}$ / mM	Concentration of HCl/ M
0.0528	0.2381	2.730
0.1077	0.2403	2.730
0.2113	0.2334	2.730
0.4313	0.2374	2.730

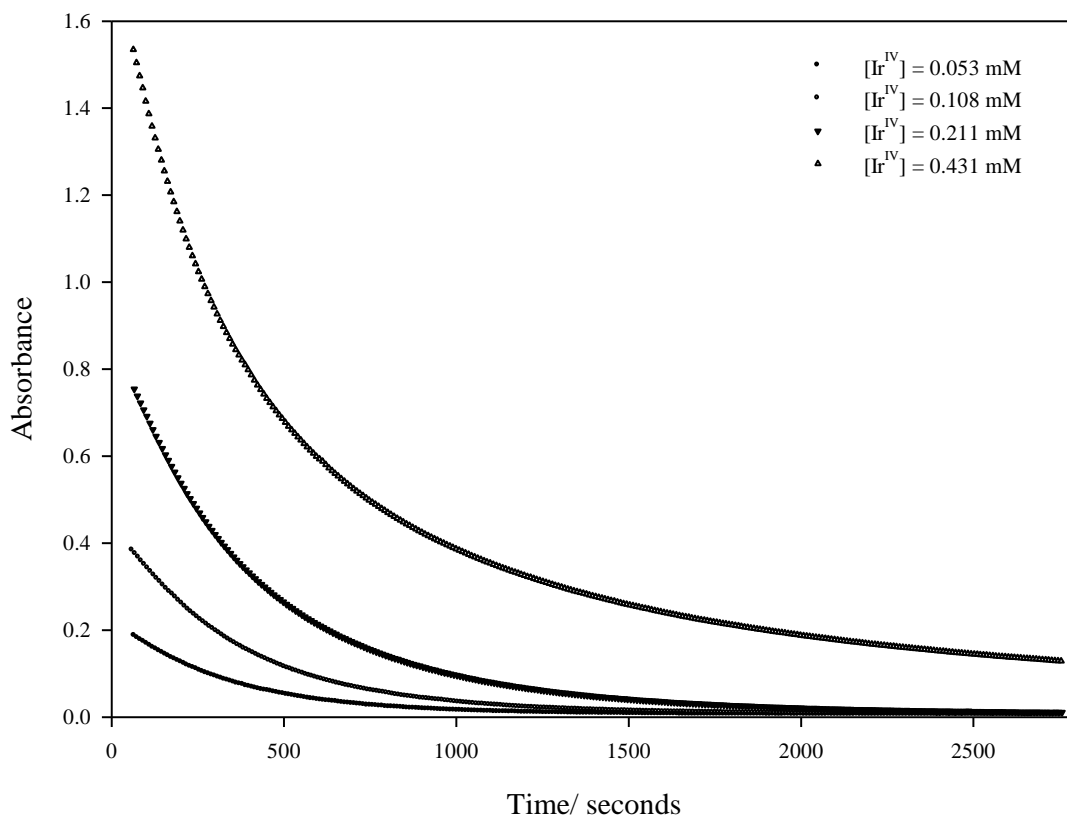


Figure 3.5: UV-Vis absorbance for the redox reaction between $[\text{Ir}^{\text{IV}}\text{Cl}_6]^{2-}$ and $[\text{Pt}^{\text{II}}\text{Cl}_4]^{2-}$ measured at 488 nm as a function of time. $[\text{Ir}^{\text{IV}}\text{Cl}_6]^{2-}$ concentrations are shown in the legend. $[\text{Pt}^{\text{II}}\text{Cl}_4]^{2-}$ concentration = 0.237 ± 0.003 mM and HCl concentration = 2.730 M, monitored at a temperature of 301.1 ± 0.2 K

With an increase in the $[\text{Ir}^{\text{IV}}\text{Cl}_6]^{2-}$ concentration, an increase in the reaction rate can be observed. This signifies that the rate of $[\text{Ir}^{\text{IV}}\text{Cl}_6]^{2-}$ reduction is dependent on the concentration of $[\text{Ir}^{\text{IV}}\text{Cl}_6]^{2-}$. The rate law, Equation 3.9, can be modified to include the dependence on $[\text{Ir}^{\text{IV}}\text{Cl}_6]^{2-}$ concentration, Equation 3.10. The reaction order (y) still needs to be evaluated (*vide infra*).

$$\frac{d[\text{Ir}^{\text{IV}}]}{dt} = -k[\text{Pt}^{\text{II}}]^x[\text{Ir}^{\text{IV}}]^y \quad (3.10)$$

3.4.3. Reaction rate as a function of ionic strength

Several samples were prepared such that the final concentration of $[\text{Ir}^{\text{IV}}\text{Cl}_6]^{2-}$, $[\text{Pt}^{\text{II}}\text{Cl}_4]^{2-}$ and HCl (0.80 M) remained constant at varying ionic strengths. The ionic strength was adjusted by the addition of NaClO_4 and the absorbance was recorded as a function of time, at 488 nm, Figure 3.6. Temperature was regulated during the sample preparation and subsequent kinetic runs at 301.1 ± 0.2 K.

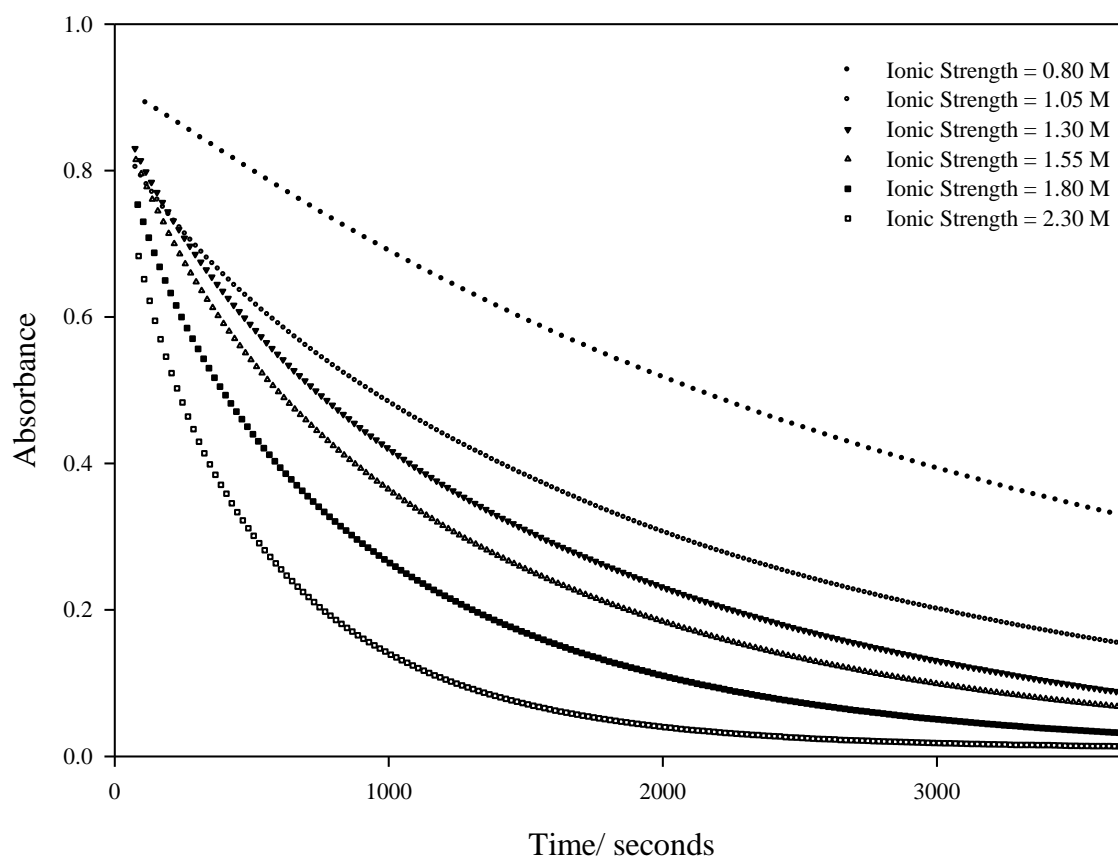


Figure 3.6: Investigation of the effect of ionic strength on the redox reaction rate by means of UV-Vis spectroscopy at 488 nm. 0.217 ± 0.008 mM $[\text{Ir}^{\text{IV}}\text{Cl}_6]^{2-}$ and 0.241 ± 0.005 mM $[\text{Pt}^{\text{II}}\text{Cl}_4]^{2-}$ was reacted at a constant temperature of 301.1 ± 0.2 K.

From Figure 3.6 it is clear that as the ionic strength increases a relatively large increase in the reaction rate is observed. As the ionic strength increases it is anticipated that the activity coefficients of $[\text{Ir}^{\text{IV}}\text{Cl}_6]^{2-}$ and $[\text{Pt}^{\text{II}}\text{Cl}_4]^{2-}$ would decrease and therefore the reaction rate should decrease. However, the opposite trend is experimentally observed and will be discussed later.

3.4.4. Reaction rate as a function of temperature

Identical samples of $[\text{Ir}^{\text{IV}}\text{Cl}_6]^{2-}$ and $[\text{Pt}^{\text{II}}\text{Cl}_4]^{2-}$ were prepared in a 2.73 M HCl matrix, Table 3.4. The redox reaction was monitored as a function of time at 488 nm, over the temperature interval of 301.1 - 310.1 \pm 0.2 K, Figure 3.7. As the temperature increases the reaction rate increases.

Table 3.4: The concentrations of $[\text{Ir}^{\text{IV}}\text{Cl}_6]^{2-}$, $[\text{Pt}^{\text{II}}\text{Cl}_4]^{2-}$ and HCl in the prepared samples for the investigation of the reaction rate dependence on temperature

Temperature/ K	Concentration of $[\text{Ir}^{\text{IV}}\text{Cl}_6]^{2-}$ / mM	Concentration of $[\text{Pt}^{\text{II}}\text{Cl}_4]^{2-}$ / mM	Concentration of HCl/ M
301.1	0.2275	0.2316	2.730
304.1	0.2224	0.2326	2.730
307.1	0.2251	0.2339	2.730
310.1	0.2232	0.2333	2.730

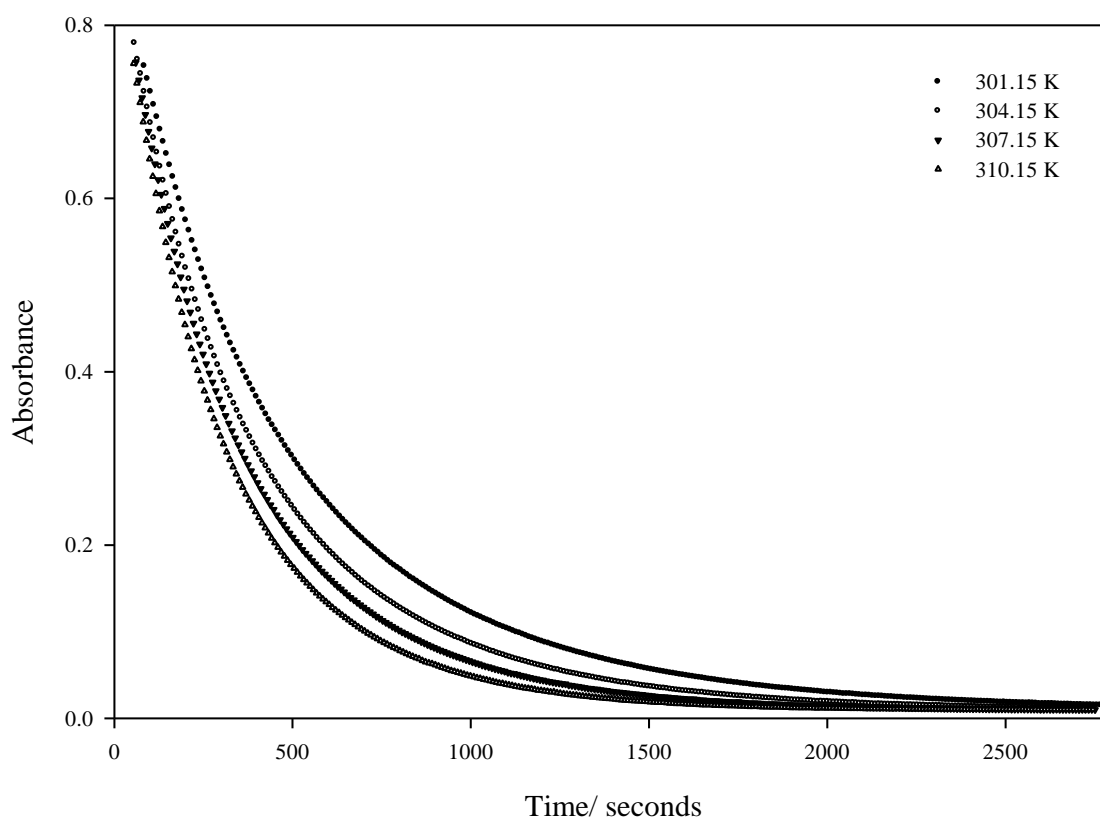


Figure 3.7: Dependence of the reaction rate on temperature. The UV-Vis absorbance was measured at 488 nm as a function of time with samples containing 0.233 ± 0.001 mM $[\text{Pt}^{\text{II}}\text{Cl}_4]^{2-}$, 0.225 ± 0.002 mM $[\text{Ir}^{\text{IV}}\text{Cl}_6]^{2-}$ and 2.73 M HCl, Table 3.4.

3.4.5. Reaction rate as a function of acid concentration

Varying the acid concentration of the sample matrix will help to determine if this redox reaction is acid catalyzed. A series of samples were prepared such that the final concentration of $[\text{Ir}^{\text{IV}}\text{Cl}_6]^{2-}$ and $[\text{Pt}^{\text{II}}\text{Cl}_4]^{2-}$ remained constant with varying mole fractions of HCl and NaCl. The sum of HCl concentration and NaCl concentration was always equal to 2.73 M. For each sample the absorbance was recorded as a function of time at 488 nm, Figure 3.8. Temperature was regulated during the sample preparation and subsequent kinetic runs at 301.1 ± 0.2 K

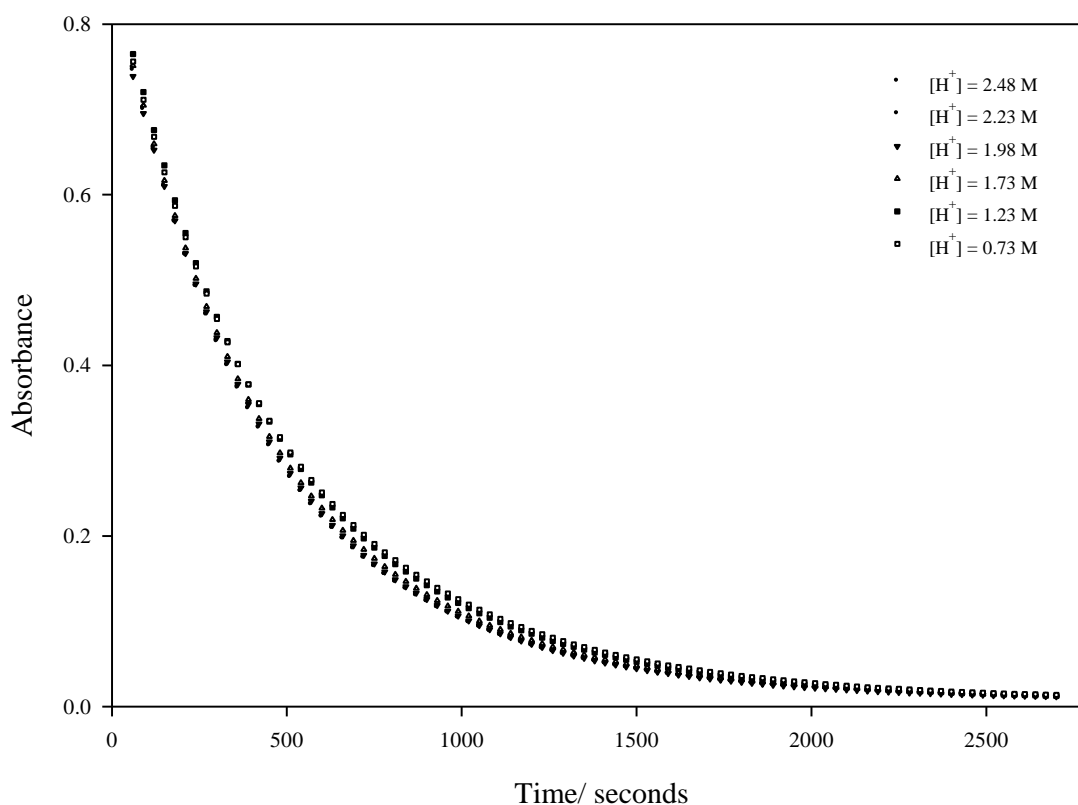


Figure 3.8: Investigation of the effect of acid concentration on the reaction rate at 301.1 ± 0.2 K. 0.224 ± 0.005 mM $[\text{Ir}^{\text{IV}}\text{Cl}_6]^{2-}$ and 0.238 ± 0.003 mM $[\text{Pt}^{\text{II}}\text{Cl}_4]^{2-}$ was reacted at a constant Cl^- concentration of 2.73 M. The UV-Vis absorbance at 488 nm was measured as a function of time.

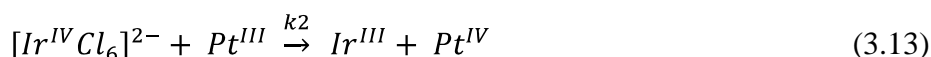
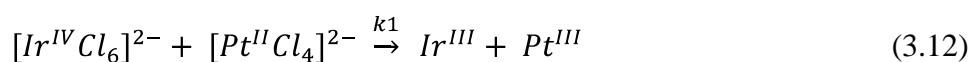
As the acid concentration increases, a negligible increase in the reaction rate is observed, Figure 3.8. The minor changes in reaction rate can be attributed to a slight change in ionic strength when HCl is replaced by NaCl. The negligible change in reaction rate implies that the redox reaction is not acid catalysed. This indicates that oxidizing agents such as OCl^- and OCl_2^- are not formed during the redox reaction since the rate of formation of such species is dependent on the acid concentration.

3.5. Proposed reaction rate model for the redox reaction between $[\text{Pt}^{\text{II}}\text{Cl}_4]^{2-}$ and $[\text{Ir}^{\text{IV}}\text{Cl}_6]^{2-}$

It is clear that the redox reaction stoichiometry of $[\text{Pt}^{\text{II}}\text{Cl}_4]^{2-}$ and $[\text{Ir}^{\text{IV}}\text{Cl}_6]^{2-}$ is $2 [\text{Ir}^{\text{IV}}\text{Cl}_6]^{2-} : 1 [\text{Pt}^{\text{II}}\text{Cl}_4]^{2-}$. If the redox reaction was to proceed through a single reaction step, the change in the $[\text{Ir}^{\text{IV}}\text{Cl}_6]^{2-}$ concentration will be second order with respect to $[\text{Ir}^{\text{IV}}\text{Cl}_6]^{2-}$ and first order with respect to $[\text{Pt}^{\text{II}}\text{Cl}_4]^{2-}$, Equation 3.11. However, this rate model yielded poor fits to the experimental data and was discarded.

$$\frac{d[\text{Ir}^{\text{IV}}]}{dt} = -k_1 [\text{Ir}^{\text{IV}}]^2 [\text{Pt}^{\text{II}}] \quad (3.11)$$

The first elementary step for this redox reaction is assumed to be a collision between $[\text{Ir}^{\text{IV}}\text{Cl}_6]^{2-}$ and $[\text{Pt}^{\text{II}}\text{Cl}_4]^{2-}$, Reaction 3.12. During the reduction of Ir^{IV} to Ir^{III} 1 electron can be transferred to the Pt^{II} complex to form a postulated Pt^{III} species. The postulated Pt^{III} species reacts with another Ir^{IV} complex, Reaction 3.13, and in the process Pt^{III} is transformed to the observed Pt^{IV} species.



From Reactions 3.12 and 3.13 the multi-step reaction rate model, Equations 3.14 - 3.18, can be derived. The reaction order with respect to $[\text{Ir}^{\text{IV}}\text{Cl}_6]^{2-}$ and $[\text{Pt}^{\text{II}}\text{Cl}_4]^{2-}$ (x and y) are both equal to one if the assumption holds that Reactions 3.12 and 3.13 are elementary steps.

$$\frac{d[\text{Ir}^{\text{IV}}]}{dt} = -k_1 [\text{Ir}^{\text{IV}}] [\text{Pt}^{\text{II}}] - k_2 [\text{Ir}^{\text{IV}}] [\text{Pt}^{\text{III}}] \quad (3.14)$$

$$\frac{d[\text{Pt}^{\text{II}}]}{dt} = -k_1 [\text{Ir}^{\text{IV}}] [\text{Pt}^{\text{II}}] \quad (3.15)$$

$$\frac{d[\text{Pt}^{\text{III}}]}{dt} = k_1 [\text{Ir}^{\text{IV}}] [\text{IrPt}^{\text{II}}] - k_2 [\text{Ir}^{\text{IV}}] [\text{Pt}^{\text{III}}] \quad (3.16)$$

$$\frac{d[\text{Ir}^{\text{III}}]}{dt} = k_1 [\text{Ir}^{\text{IV}}] [\text{Pt}^{\text{II}}] + k_2 [\text{Ir}^{\text{IV}}] [\text{Pt}^{\text{III}}] \quad (3.17)$$

$$\frac{d[\text{Pt}^{\text{IV}}]}{dt} = k_2 [\text{Ir}^{\text{IV}}] [\text{Pt}^{\text{III}}] \quad (3.18)$$

Using the program *Equikin*, the multi-step reaction rate model, Equations 3.14 - 3.18, was simulated and the non-linear least squares fits obtained are shown in Figures 3.9 and 3.10. The calculated rate constants and molar extinction coefficients are listed in Table 3.5.

Table 3.5: Rate constants and molar extinction coefficients, calculated by simulation of the multi-step reaction rate model on the experimental data, Equations 3.14 - 3.18.

Concentration of Analytes/ mM		Calculated Rate Constants/ $\text{M}^{-1}\cdot\text{sec}^{-1}$		Calculated Molar Extinction Coefficients/ $\text{M}^{-1}\cdot\text{cm}^{-1}$				
$[\text{Ir}^{\text{IV}}\text{Cl}_6]^{2-}$	$[\text{Pt}^{\text{II}}\text{Cl}_4]^{2-}$	k_1	k_2	Ir^{IV}	Ir^{III}	Pt^{II}	Pt^{III}	Pt^{IV}
0.2149	0.0260	7.51	15.43	4046	15	1	1	7
0.2128	0.0456	6.96	27.74	4091	7	30	2	18
0.2143	0.1163	6.70	52.02	4033	16	19	0	1
0.2240	0.2462	7.05	54.18	3966	31	15	1	1
0.2077	0.4644	7.32	90.56	3950	36	16	1	1
0.2167	0.9778	6.54	359.27	3932	32	14	1	1
0.2014	1.4225	6.58	20995.75	3889	33	15	1	1
0.0528	0.2381	7.33	243.81	4009	33	15	1	1
0.1077	0.2403	7.17	105.38	4013	30	15	1	1
0.2113	0.2334	7.39	52.95	4089	29	14	1	1
0.4313	0.2374	6.87	32.25	4013	17	33	1	0
Average		7.04	2002.67	4003	25	17	1	3
Standard Deviation		0.34	6300.18	63	10	9	0	5

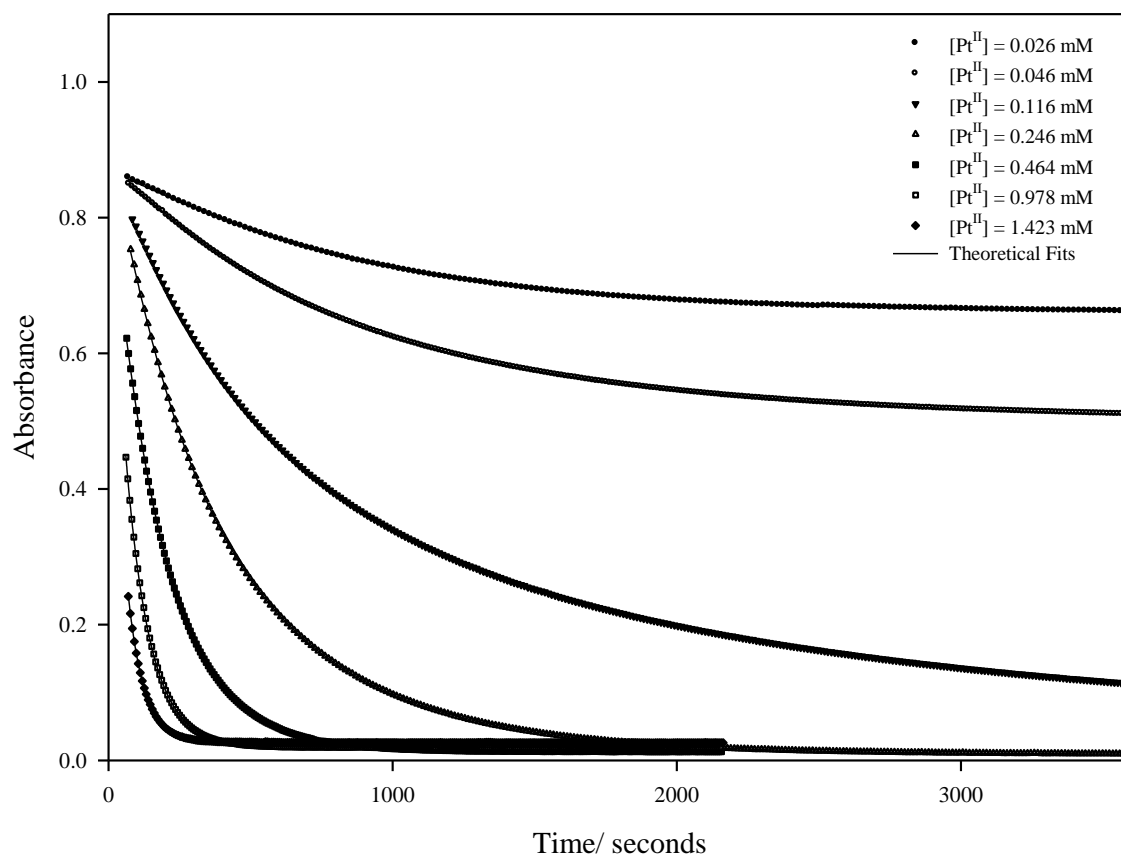


Figure 3.9: The non-linear least-squares fits of the multi-step reaction rate model described by Equations 3.14 - 3.18 at varying $[\text{Pt}^{\text{II}}\text{Cl}_4]^{2-}$ concentrations. The dotted plots represent the experimental data with the simulated functions represented by the solid lines.

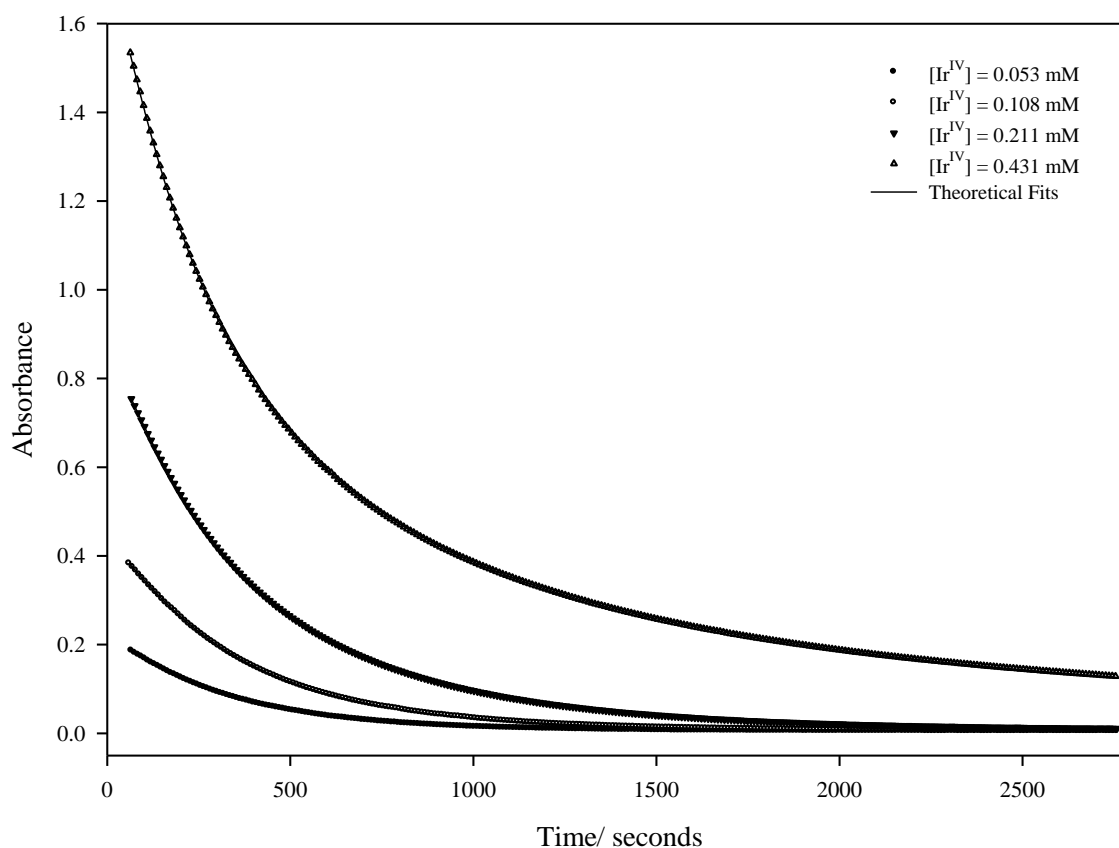


Figure 3.10: The non-linear least-squares fit of the multi-step reaction rate model described by Equations 3.14 - 3.18 at varying $[\text{Ir}^{\text{IV}}\text{Cl}_6]^{2-}$ concentrations. The dotted plots represent the experimental data with the simulated functions represented by the solid lines.

For each individual kinetic data set, excellent fits between the experimental and calculated data is obtained. Consistent k_1 values, Table 3.5, were obtained with an average value of $7.04 \pm 0.34 \text{ M}^{-1}.\text{sec}^{-1}$. However, the calculated k_2 varies considerably with an average value of $2002.67 \pm 6300.18 \text{ M}^{-1}.\text{sec}^{-1}$. The average calculated molar extinction coefficient of $[\text{Ir}^{\text{IV}}\text{Cl}_6]^{2-}$ at 488 nm is $4003 \pm 63 \text{ M}^{-1}.\text{cm}^{-1}$ and compares well with the molar extinction coefficient of $[\text{Ir}^{\text{IV}}\text{Cl}_6]^{2-}$ obtained experimentally at 488 nm ($3920 \text{ M}^{-1}.\text{cm}^{-1}$). Because $k_2 > k_1$ and in some cases $k_2 \gg k_1$, it is clear that the first oxidation reaction of Pt^{II} , Reaction 3.12, is the rate determining step. In order to explain the relatively large variation in the calculated k_2 values an understanding of the chemical nature, or rather the reactivity of each species postulated is required, in particular, the Pt^{III} species.

Several detailed studies concerning the photo-reduction of $[\text{Pt}^{\text{IV}}\text{Cl}_6]^{2-}$ to produce $[\text{Pt}^{\text{III}}\text{Cl}_5]^{2-}$ in well-defined HCl matrices, have been reported.^{36,37,41-43} Glebov *et al.* were able to record the spectrum of the $[\text{Pt}^{\text{III}}\text{Cl}_5]^{2-}$ complex anion in the range of 300 - 500 nm by means of laser flash photolysis, Figure 3.11.⁴² Moreover, Lawrence³⁷ and Balashev⁴⁴ have reported molar extinction coefficients for the $[\text{Pt}^{\text{III}}\text{Cl}_5]^{2-}$ complex at 410 nm of $3700 \text{ M}^{-1}.\text{cm}^{-1}$ and $3500 \text{ M}^{-1}.\text{cm}^{-1}$ respectively.

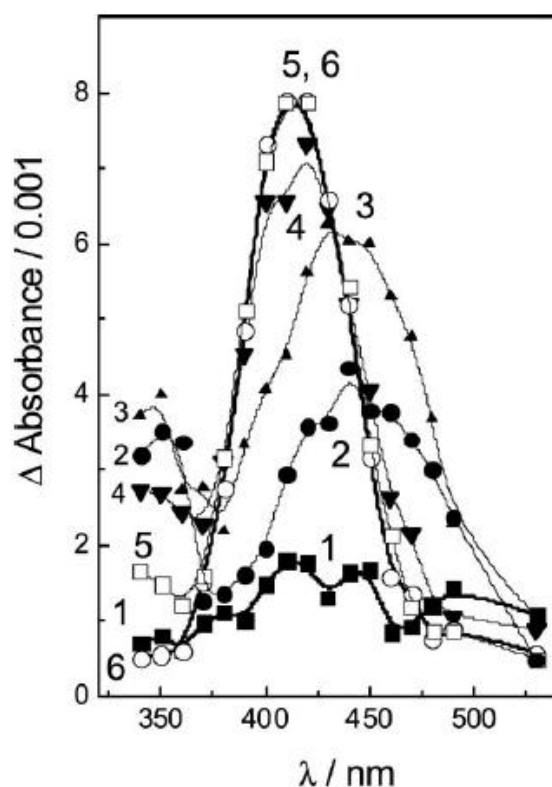


Figure 3.11: The UV-Vis spectrum of the $[\text{Pt}^{\text{III}}\text{Cl}_5]^{2-}$ species (spectrum 5 of this figure) as obtained by laser flash photolysis and published by Glebov *et al.*⁴²

The $[\text{Pt}^{\text{III}}\text{Cl}_5]^{2-}$ complex anion is reported to have a short lifetime of 100 μs , and that Pt^{III} form a wide variety of aqua-hydroxido-chlorido complexes.^{42,45} Moreover, the rate constant obtained for the reaction of $[\text{Pt}^{\text{III}}\text{Cl}_5]^{2-}$ with Creatinine was found to be $3.4 \times 10^7 \text{ M}^{-1}.\text{sec}^{-1}$.⁴³ In addition, the rate constant reported for the disproportionation reaction of Pt^{III} is $4.6 \times 10^6 \text{ M}^{-1}.\text{sec}^{-1}$.³⁷ Both reactions were described as diffusion controlled/ limited. If the disproportionation reaction of Pt^{III} , to produce Pt^{II} and Pt^{IV} , occurs to a significant extent in our redox system a relatively large deviation from the 2 $[\text{Ir}^{\text{IV}}\text{Cl}_6]^{2-}$: 1 $[\text{Pt}^{\text{II}}\text{Cl}_4]^{2-}$ stoichiometry would be observed, which is clearly not the case here. We rationalize this result in terms of the relatively high concentration of $[\text{Ir}^{\text{IV}}\text{Cl}_6]^{2-}$ in the sample compared with the relatively low

Pt^{III} concentration present. In essence the probability that Pt^{III} will encounter $[\text{Ir}^{\text{IV}}\text{Cl}_6]^{2-}$ is much larger than a $\text{Pt}^{\text{III}} - \text{Pt}^{\text{III}}$ encounter and explains why this disproportionation reaction does not occur to a significant extent in our redox system.

Taking into account that Pt^{III} is a highly reactive species allows for further refinement of the reaction rate model. If we now assume that the second redox reaction, Reaction 3.13, is diffusion controlled, then k_2 is at least 10^6 times larger than k_1 , Reaction 3.12. To this end, k_2 can be described as infinitely large with respect to k_1 , which will have a considerable effect on the formulation of the rate law for this redox reaction. As soon as the rate limiting reaction takes place, Reaction 3.12, the subsequent reaction, Reaction 3.13, will occur almost instantaneously ($k_2 = \infty$). Therefore, the Pt^{III} concentration at any given time during the redox reaction is insignificantly small ($\text{Pt}^{\text{III}} = 0$) and the rate model can be approximated by applying the steady state approximation, Equations 3.19 - 3.22. The multi-step reaction rate model given by Equations 3.14 - 3.18 then transform to the diffusion controlled rate model, Equations 3.22 - 3.25. The notion that the stoichiometry of the redox reactions are $2 [\text{Ir}^{\text{IV}}\text{Cl}_6]^{2-} : 1 [\text{Pt}^{\text{II}}\text{Cl}_4]^{2-}$ is retained since the concentration of $[\text{Ir}^{\text{IV}}\text{Cl}_6]^{2-}$ decreases essentially twice as fast as the concentration of $[\text{Pt}^{\text{II}}\text{Cl}_4]^{2-}$.

$$\frac{d[\text{Pt}^{\text{III}}]}{dt} = k_1 [\text{Ir}^{\text{IV}}] [\text{Pt}^{\text{II}}] - k_2 [\text{Ir}^{\text{IV}}] [\text{Pt}^{\text{III}}] = 0 \quad (3.19)$$

$$[\text{Pt}^{\text{III}}] = \frac{k_1 [\text{Ir}^{\text{IV}}] [\text{Pt}^{\text{II}}]}{k_2 [\text{Ir}^{\text{IV}}]} = 0 \quad (3.20)$$

$$\frac{d[\text{Ir}^{\text{IV}}]}{dt} = -k_1 [\text{Ir}^{\text{IV}}] [\text{Pt}^{\text{II}}] - k_2 [\text{Ir}^{\text{IV}}] \left[\frac{k_1 [\text{Ir}^{\text{IV}}] [\text{Pt}^{\text{II}}]}{k_2 [\text{Ir}^{\text{IV}}]} \right] \quad (3.21)$$

$$\frac{d[\text{Ir}^{\text{IV}}]}{dt} = -2 k_1 [\text{Ir}^{\text{IV}}] [\text{Pt}^{\text{II}}] \quad (3.22)$$

$$\frac{d[\text{Pt}^{\text{II}}]}{dt} = -k_1 [\text{Ir}^{\text{IV}}] [\text{Pt}^{\text{II}}] \quad (3.23)$$

$$\frac{d[\text{Ir}^{\text{III}}]}{dt} = 2 k_1 [\text{Ir}^{\text{IV}}] [\text{Pt}^{\text{II}}] \quad (3.24)$$

$$\frac{d[\text{Pt}^{\text{IV}}]}{dt} = k_1 [\text{Ir}^{\text{IV}}] [\text{Pt}^{\text{II}}] \quad (3.25)$$

Using the program *Equikin*, the diffusion controlled rate model (Equations 3.22 - 3.25) was simulated. The non-linear least-squares fits are illustrated in Figures 3.12 and 3.13 and the calculated rate constants and molar extinction coefficients are listed in Table 3.6.

Table 3.6: Rate constants and molar extinction coefficients calculated by simulation of the diffusion controlled rate model, Equations 3.22 - 3.25, on the experimental data

Concentration of Analytes/ mM		Calculated Rate Constant/ $\text{M}^{-1}\cdot\text{sec}^{-1}$	Calculated Molar Extinction Coefficients/ $\text{M}^{-1}\cdot\text{cm}^{-1}$			
$[\text{Ir}^{\text{IV}}\text{Cl}_6]^{2-}$	$[\text{Pt}^{\text{II}}\text{Cl}_4]^{2-}$		Ir^{IV}	Ir^{III}	Pt^{II}	Pt^{IV}
0.2149	0.0260	5.81	4040	5	4	2
0.2128	0.0456	5.64	3977	0	754	1
0.2143	0.1163	6.79	4273	3	1	1
0.2240	0.2462	6.85	4385	34	1	1
0.2077	0.4644	6.94	4469	46	8	0
0.2167	0.9778	6.49	4232	32	14	1
0.2014	1.4225	6.50	3856	32	15	1
0.0528	0.2381	6.95	4364	21	16	1
0.1077	0.2403	6.76	4384	19	17	1
0.2113	0.2334	6.94	4468	7	3	26
0.4313	0.2374	6.94	4385	2	1	5
Average		6.60	4258	18	76	4
Standard Deviation		0.46	209	16	225	7

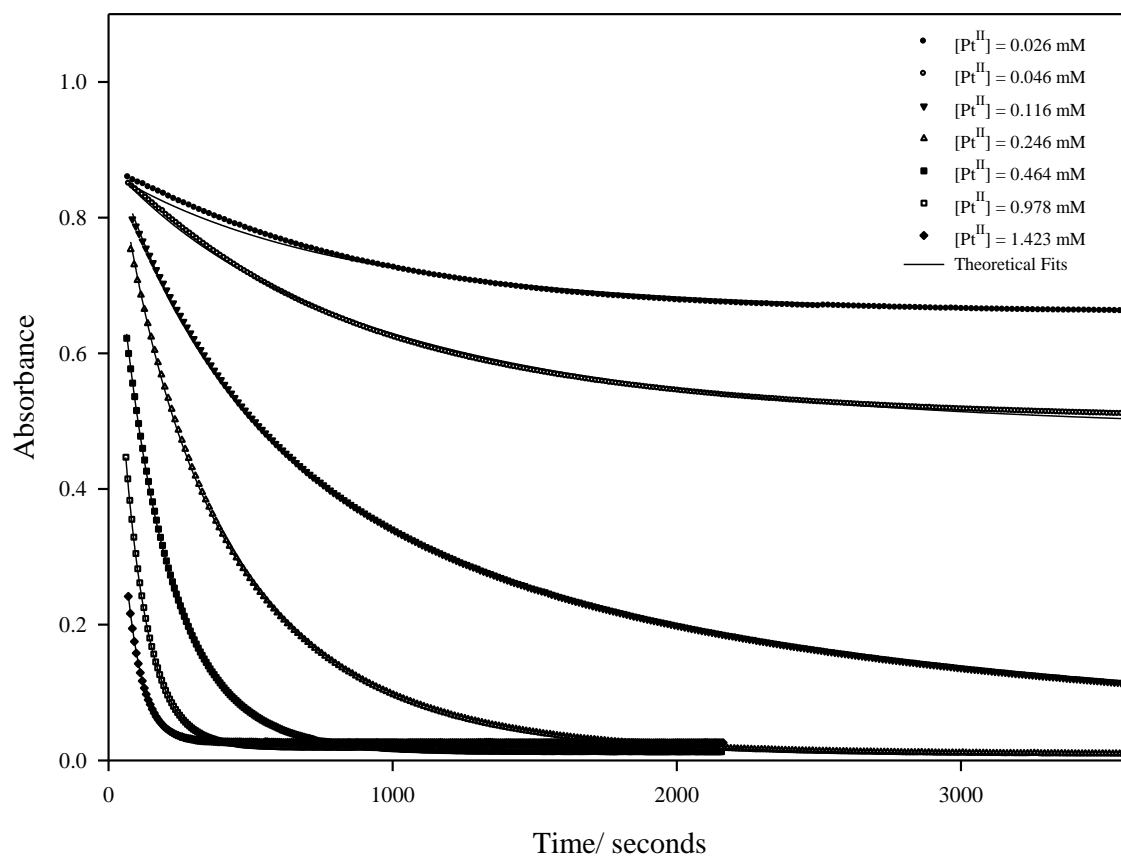


Figure 3.12: The non-linear least squares-fit of the diffusion controlled rate model, Equations 3.22 - 3.25, at varying $[\text{Pt}^{\text{II}}\text{Cl}_4]^{2-}$ concentrations. The dotted plots represent the experimental data with the simulated functions represented by the solid lines.

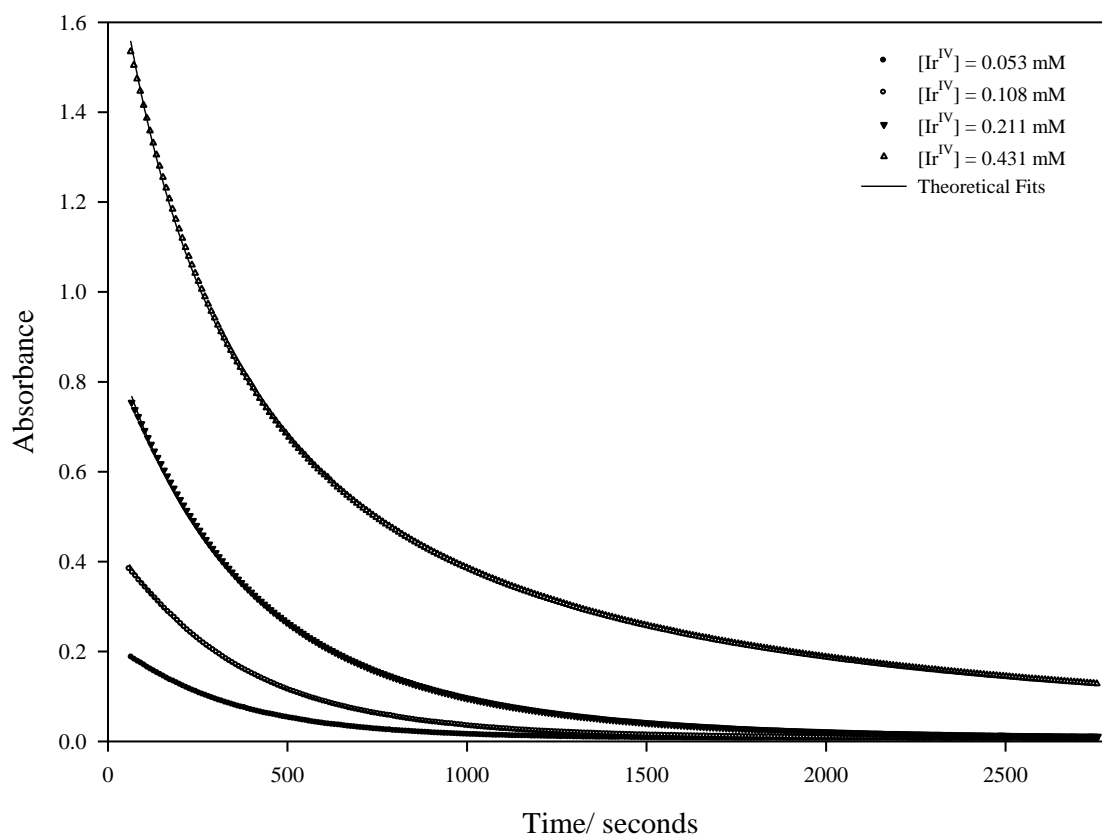


Figure 3.13: The non-linear least-squares fits of the diffusion controlled rate model, Equations 3.22 - 3.25, at varying $[\text{Ir}^{\text{IV}}\text{Cl}_6]^{2-}$ concentrations. The dotted plots represent the experimental data with the simulated functions represented by the solid lines.

The fits obtained for the kinetic data sets are excellent with only minor deviations observed at relatively low $[\text{Pt}^{\text{II}}\text{Cl}_4]^{2-}$ concentration, Figure 3.12. The calculated values obtained for k_1 , Table 3.6, are consistent and yield an average value of $6.60 \pm 0.46 \text{ M}^{-1} \cdot \text{sec}^{-1}$. This value compares well to the k_1 value obtained with the multi-step reaction rate model, Equations 3.14 - 3.18, ($k_1 = 7.04 \pm 0.34 \text{ M}^{-1} \cdot \text{sec}^{-1}$). The calculated molar extinction coefficients for the $[\text{Ir}^{\text{IV}}\text{Cl}_6]^{2-}$ complex anion at 488 nm are also consistent, with an average value of $4258 \pm 209 \text{ M}^{-1} \cdot \text{cm}^{-1}$. This molar extinction coefficient is slightly higher in comparison to the value reported for the $[\text{Ir}^{\text{IV}}\text{Cl}_6]^{2-}$ species at 488 nm ($3920 \text{ M}^{-1} \cdot \text{cm}^{-1}$). In reality the decrease in $[\text{Ir}^{\text{IV}}\text{Cl}_6]^{2-}$ concentration during the second redox reaction, Reaction 3.13, is slightly slower than proposed by the diffusion controlled rate model, Equations 3.22 - 3.25. The least squares fitting routine in the program *Equikin* compensates for this by increasing the calculated molar extinction coefficient of $[\text{Ir}^{\text{IV}}\text{Cl}_6]^{2-}$. Moreover, the difference between the calculated and experimental molar extinction coefficients of $[\text{Ir}^{\text{IV}}\text{Cl}_6]^{2-}$

is less than 8 % and is reasonably small when compared to the uncertainty in the calculated molar extinction coefficient of 5 %. The average rate constant (k_1) and molar extinction coefficients numerical values, listed in Table 3.6, were then used to simulate all the experimental data, Figures 3.14 and 3.15.

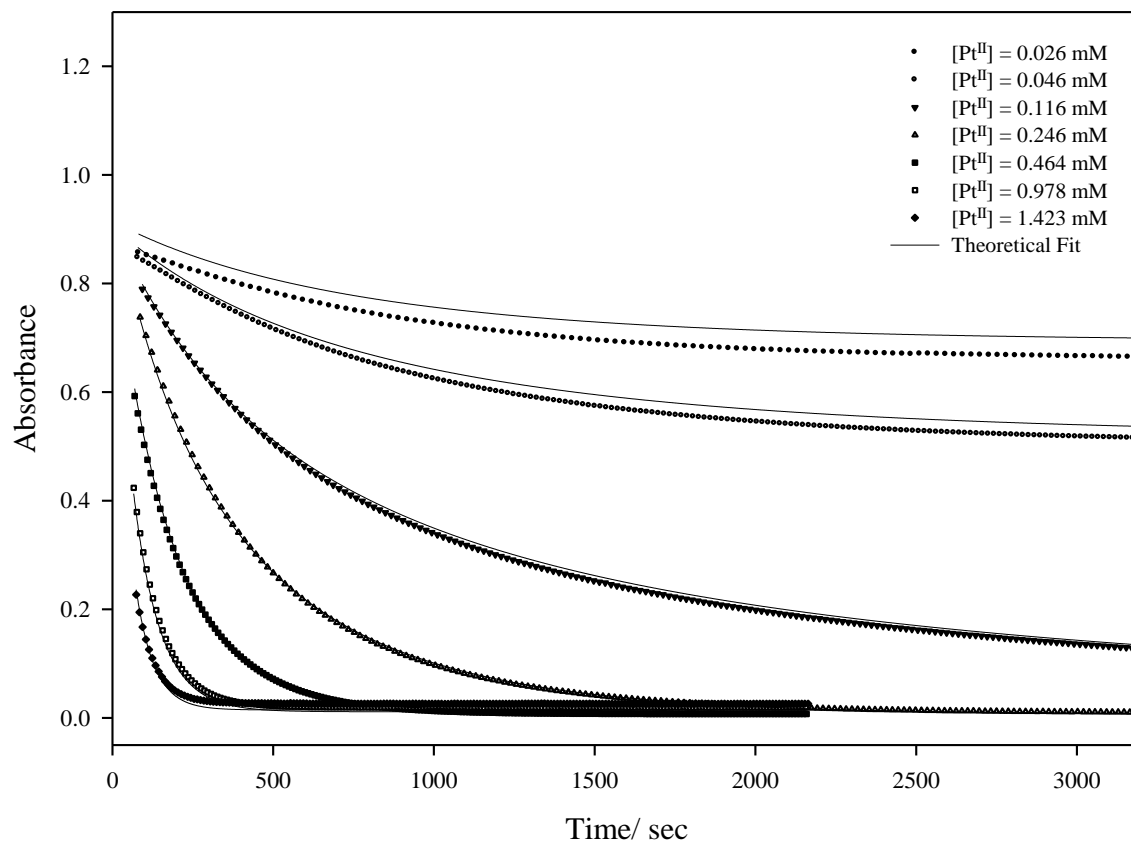


Figure 3.14: Fits of the average rate constant and molar extinction coefficients, Table 3.6, to the kinetic data sets at varying $[\text{Pt}^{\text{II}}\text{Cl}_4]^{2-}$ concentrations.

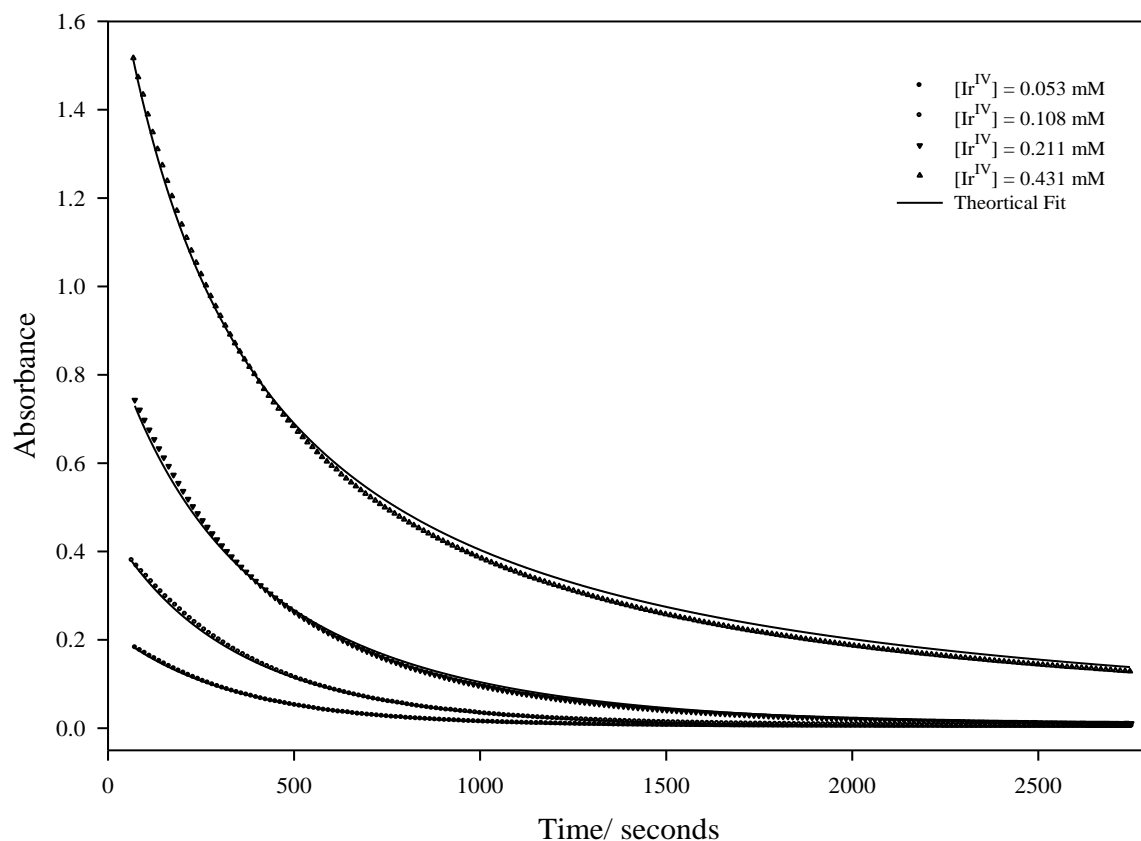


Figure 3.15: Fits of the average rate constant and molar extinction coefficients, Table 3.6, to the kinetic data sets at varying $[\text{Ir}^{\text{IV}}\text{Cl}_6]^{2-}$ concentration.

The correlation between the simulated and experimental data, Figures 3.14 and 3.15, using the average rate constant (k_1) and molar extinction coefficients are in good agreement. However, at low concentrations of $[\text{Pt}^{\text{II}}\text{Cl}_4]^{2-}$, Figure 3.14, the calculated data do not exactly overlay with the experimental data. This can be explained in terms of the larger average molar extinction coefficient for $[\text{Ir}^{\text{IV}}\text{Cl}_6]^{2-}$ calculated with the diffusion controlled rate model, Table 3.6. However, the good fits support the assumption made with respect to the diffusion controlled rate model, Equations 3.22 - 3.25, that the Pt^{III} concentration is negligible at any given time during the kinetic run. Moreover, the experimental data can only be accounted for by the postulation of a Pt^{III} species in the rate model, albeit at low concentrations.

Using the program *Equikin*, the kinetic data set at variable ionic strength was simulated with the diffusion controlled rate model, Equations 3.22 - 3.25. The non-linear least squares fits are shown in Figure 3.16 with the calculated rate constant (k_1) and molar extinction coefficients listed in Table 3.7.

Table 3.7: Rate constants and molar extinction coefficients calculated by simulation of the diffusion controlled rate model, Equations 3.22 - 3.25, on the experimental data at variable ionic strength

Concentration of Analytes/ mM		Concentration of Ionic strength modifiers/ M		Calculated Rate Constant/ $\text{M}^{-1} \cdot \text{sec}^{-1}$	Calculated Molar Extinction Coefficients/ $\text{M}^{-1} \cdot \text{cm}^{-1}$			
$[\text{Ir}^{\text{IV}}\text{Cl}_6]^{2-}$	$[\text{Pt}^{\text{II}}\text{Cl}_4]^{2-}$	HCl	NaClO_4	k_1	Ir^{IV}	Ir^{III}	Pt^{II}	Pt^{IV}
0.220	0.240	0.80	0.00	0.713	4284	3	1	0
0.220	0.240	0.80	0.25	1.366	3803	82	23	2
0.220	0.240	0.80	0.50	1.802	3896	18	16	1
0.220	0.240	0.80	0.75	2.195	3937	27	14	1
0.220	0.240	0.80	1.00	3.108	3815	39	14	0
0.220	0.240	0.80	1.50	5.329	3817	47	9	1

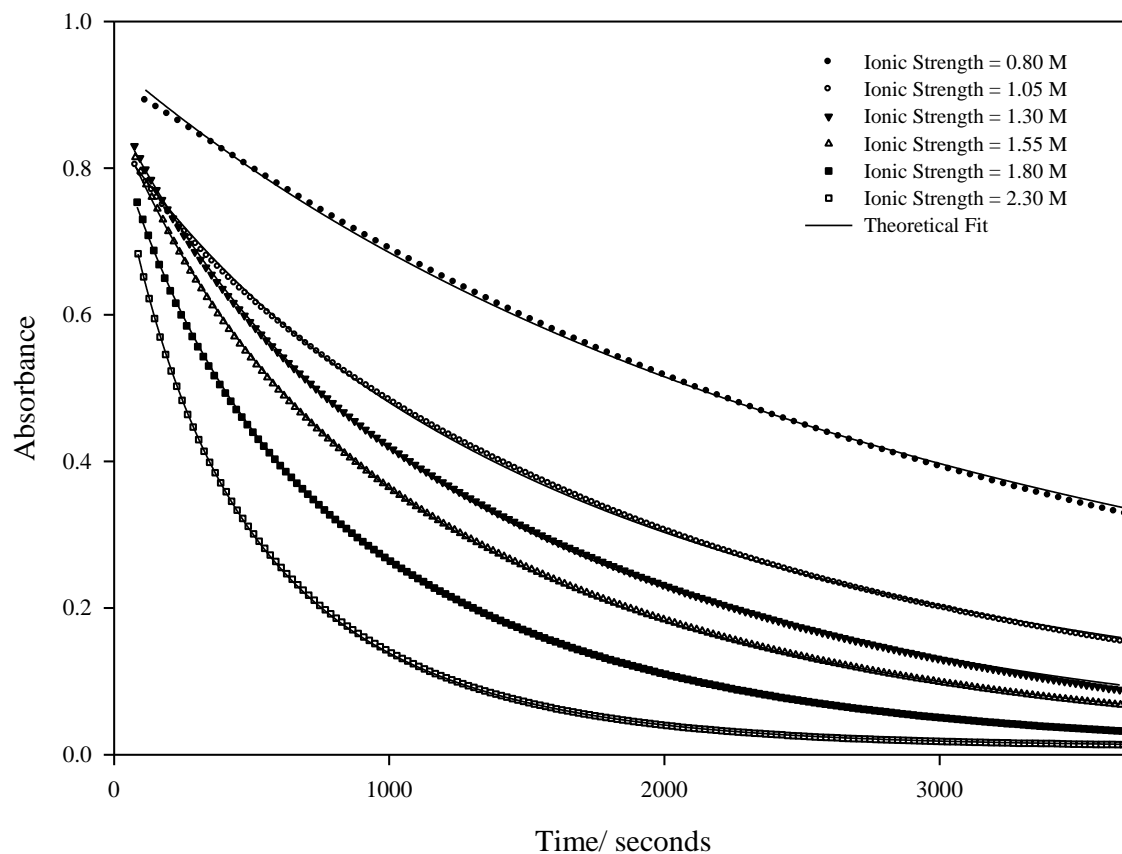


Figure 3.16: The non-linear least-squares fits of the diffusion controlled rate model, Equations 3.22 - 3.25, at varying ionic strength. The dotted plots represent the experimental data with the simulated functions represented by the solid lines.

The calculated rate constant (k_1) increases with an increase in NaClO_4 concentration as illustrated in Figure 3.17. To account for this counterintuitive trend it should be noted that both reactants are negatively charged and will repel each other. With an increase in ionic strength the Na^+ concentration increases, leading to the formation of presumably solvent separated ion-pairs that can lower the repulsion between reactants.¹⁸ This will cause a decrease in the Gibbs energy of activation (ΔG^\ddagger), Equation 1.4, resulting in an increase of the reaction rate, which is consistent with the results observed in Table 3.7. This trend is also reflected in the data reported by Taube and Myers for a similar redox system.¹⁹ Quantitative validation of this postulation is currently underway with a density functional theory-molecular dynamics (DFT-MD) simulation.

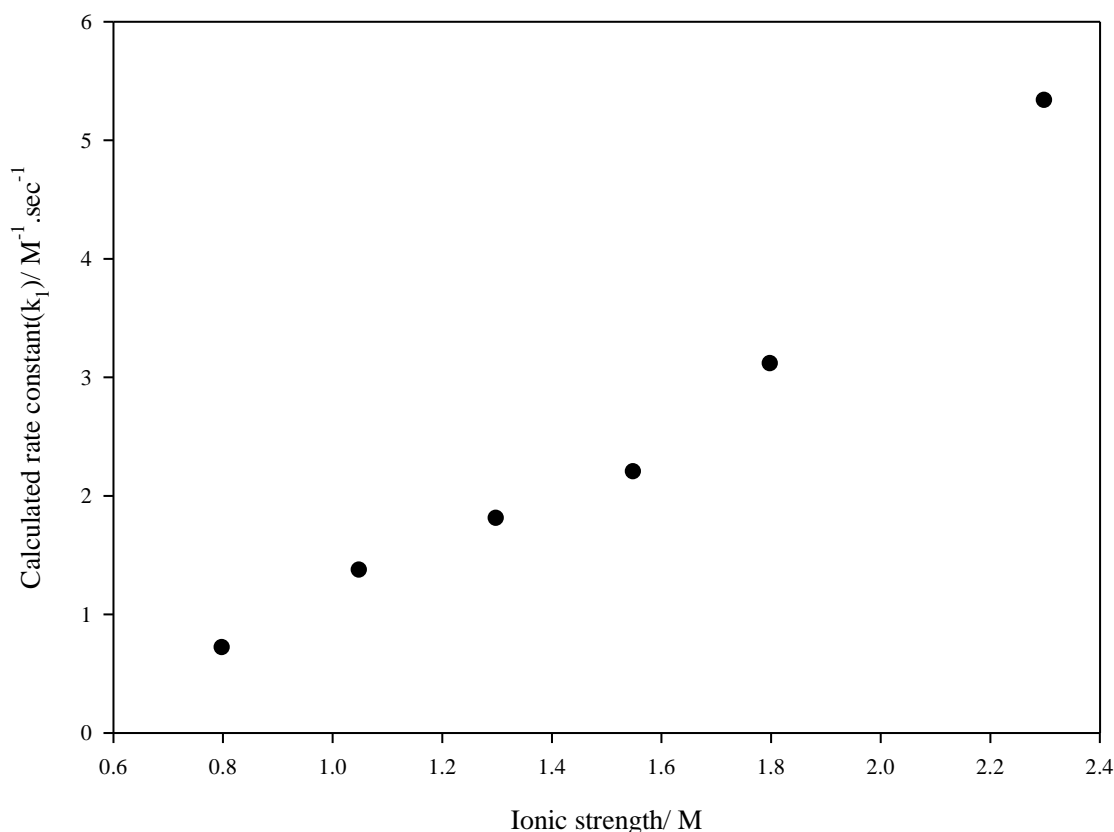


Figure 3.17: A plot of the calculated rate constant (k_1) listed in Table 3.7 vs. ionic strength representing the dependence of the reaction rate on the change in ionic strength.

Using the program *Equikin*, the variable temperature data set was simulated with the diffusion controlled rate model, Equations 3.22 - 3.25, and the non-linear least squares fits are illustrated in Figure 3.18. The fits obtained for each individual kinetic run is excellent. The calculated rate constant (k_1) and molar extinction coefficients are listed in Table 3.8.

Table 3.8: Rate constants and molar extinction coefficients calculated by simulation of the diffusion controlled rate model, Equations 3.22 - 3.25, on the experimental data at variable temperature

Temperature/ K	Concentration of Analytes/ mM		Calculated Rate Constant/ $\text{M}^{-1}.\text{sec}^{-1}$	Calculated Molar Extinction Coefficients/ $\text{M}^{-1}.\text{cm}^{-1}$			
	$[\text{Ir}^{\text{IV}}\text{Cl}_6]^{2-}$	$[\text{Pt}^{\text{II}}\text{Cl}_4]^{2-}$		k_1	Ir^{IV}	Ir^{III}	Pt^{II}
301.1	0.2275	0.2316	6.42	4189	8	55	1
304.1	0.2224	0.2326	7.71	4270	1	51	1
307.1	0.2251	0.2339	8.80	4269	2	52	0
310.1	0.2232	0.2333	10.17	4351	2	57	0

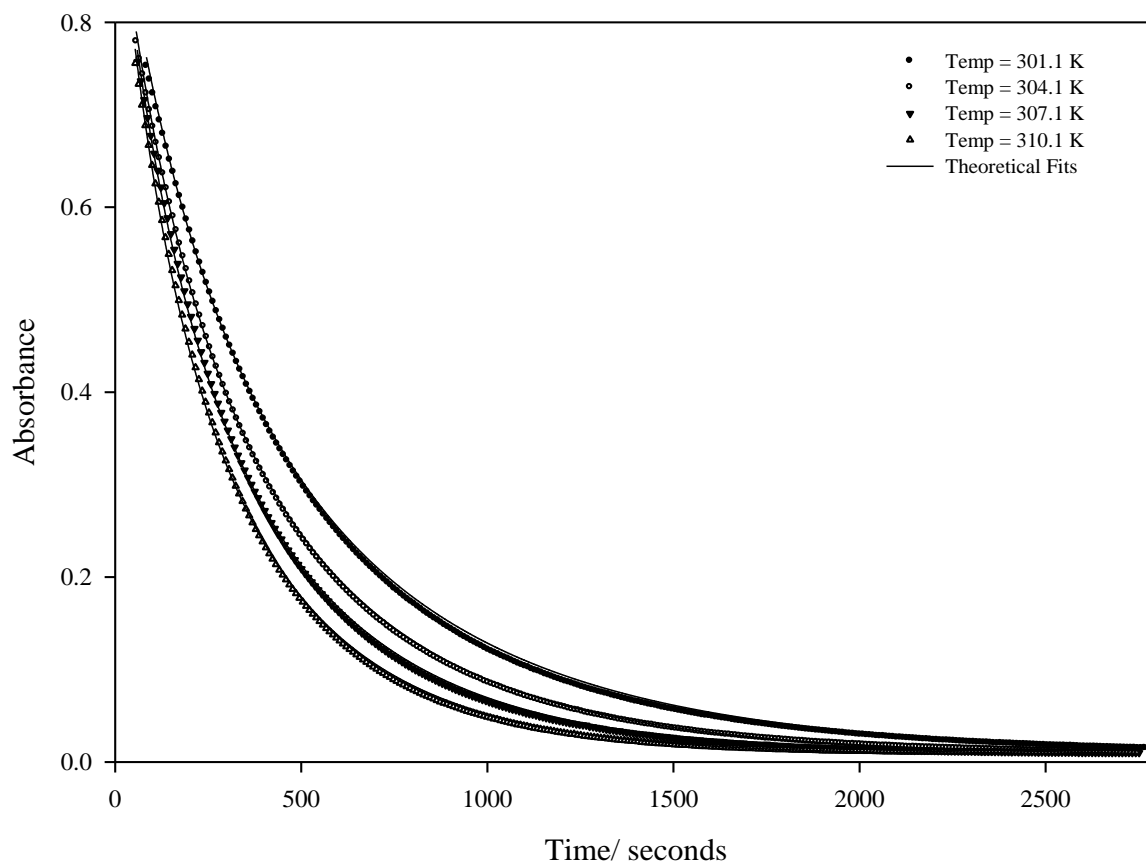


Figure 3.18: The non-linear least-squares fits of the diffusion controlled rate model, Equations 3.22 - 3.25, at varying temperature. The dotted plots represent the experimental data with the simulated functions represented by the solid lines.

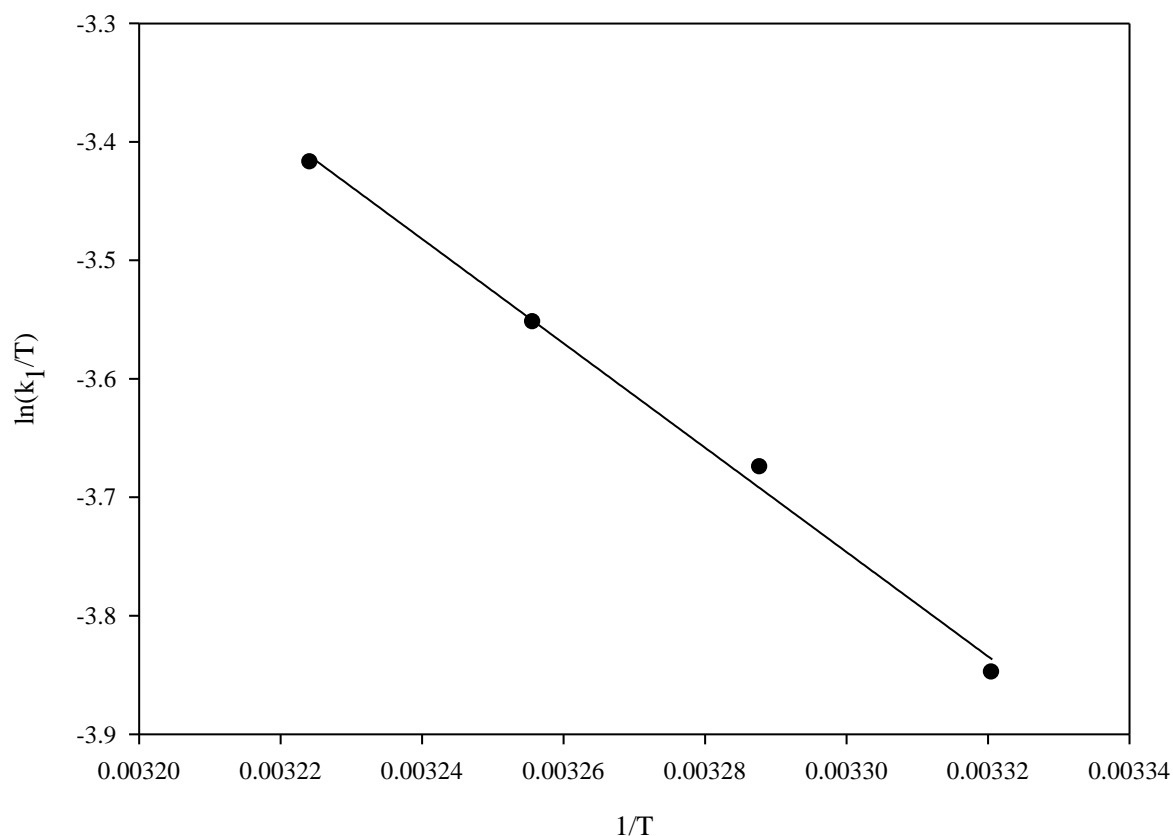


Figure 3.19: The Eyring plot of the calculate rate constants as obtained by the diffusion controlled rate model, Equations 3.22 - 3.25, at varying temperature.

Using the Eyring equation²², Equations 3.26 and 3.27, a plot of $\ln(k_1/T)$ vs $1/T$ is shown in Figure 3.19. A linear trend was obtained, indicating that the enthalpy of activation (ΔH^\ddagger) is not dependent on temperature in the range of 301.1 - 310.1 K. Moreover, the linear relationship further support the proposed diffusion controlled rate model. From the slope and intercept the enthalpy of activation ($\Delta H^\ddagger = 36.65 \pm 0.24 \text{ kJ.mol}^{-1}$) and entropy of activation ($\Delta S^\ddagger = -107.76 \pm 0.87 \text{ J.mol}^{-1}.\text{K}^{-1}$) were calculated. The Gibbs energy of activation (ΔG^\ddagger) can be calculated using Equation 3.28. This correlates to a value of $\Delta G^\ddagger = 68.77 \pm 0.15 \text{ kJ.mol}^{-1}$ at 298.1 K. The relatively large negative value obtained for ΔS^\ddagger is indicative of a reaction that occurs via an associative mechanism.⁴⁶ During formation of the activated complex the reagent complexes 'combine', therefore decreasing the range of vibrational, translational and rotational states that are available for the partitioning of energy and therefore results in a negative ΔS^\ddagger .⁴⁶

$$k_1 = \frac{k_B T}{h} e^{(\Delta S^\ddagger/R)} e^{(-\Delta H^\ddagger/RT)} \quad (3.26)$$

$$\ln\left(\frac{k_1}{T}\right) = -\left(\frac{\Delta H^\ddagger}{R}\right) \frac{1}{T} + \left(\ln\left(\frac{k_B}{h}\right) + \frac{\Delta S^\ddagger}{R}\right) \quad (3.27)$$

$$\Delta G^\ddagger = \Delta H^\ddagger - T\Delta S^\ddagger \quad (3.28)$$

3.6. Evidence for the existence of Pt^{III} chlorido species in the gas-phase by ESI-MS analysis of $[\text{Pt}^{\text{IV}}\text{Cl}_6]^{2-}$

A 1 mM $[\text{Pt}^{\text{IV}}\text{Cl}_6]^{2-}$ was prepared in acetonitrile and analysed by high resolution ESI-Q-TOF-MS. The analysis was carried out in the cone voltage range of 15 to 100 V and the acquired mass spectral data are shown in Figure 3.20 (a) - (d). The $[\text{Pt}^{\text{IV}}\text{Cl}_6]^{2-}$ complex anion undergoes substantial fragmentation during analysis, the extent of which increases with an increase in cone voltage.⁴⁷ The natural abundance of the stable isotopes of Pt (^{194}Pt , ^{195}Pt , ^{196}Pt) and Cl (^{35}Cl , ^{37}Cl) results in a characteristic isotopologue^b peak pattern for each anionic complex, which in conjunction with high resolution spectral data produces a ‘fingerprint’ that can be used to identify a given species. The isotopologue peak pattern in the m/z range of 201.891 - 206.889, Figure 3.20 (a), is separated by half m/z units, signifying a doubly charged ion, and was reported by Henderson *et. al.* to represent the $[\text{Pt}^{\text{IV}}\text{Cl}_6]^{2-}$ parent ion.⁴⁷ However, there is a lack of agreement between the m/z values of the experimental and calculated data with an m/z deviation of 1. Therefore, we propose that this isotopologue peak pattern ($m/z = 201.891 - 206.889$) corresponds to the $[\text{H}_2\text{Pt}^{\text{II}}\text{Cl}_6]^{2-}$ complex anion, supported by the excellent agreement between the experimental isotopologue peak pattern intensities and m/z ratios with those calculated, Figure 3.21 (a) and (b). The parent ion is instead observed as the sodium ion-pair adduct ($[\text{M}+\text{Na}]$) at the m/z range of 426.765 - 434.757.

^b Isotopologues refer to complexes with the same chemical formula but differ in the isotope content of the complexes.

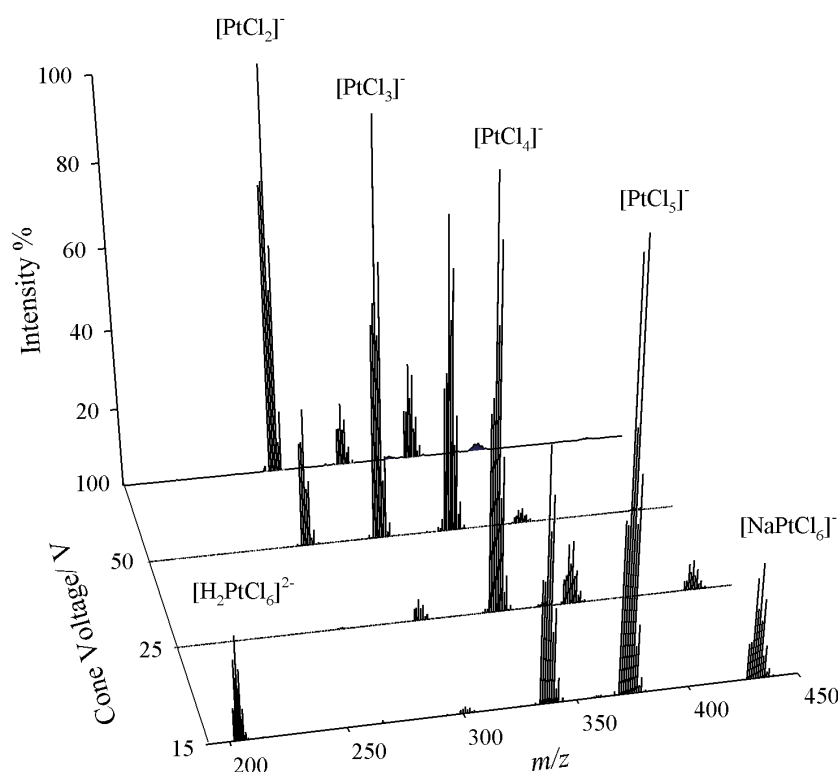


Figure 3.20: The high resolution ESI mass spectra obtained from the direct infusion analysis of $[\text{Pt}^{\text{IV}}\text{Cl}_6]^{2-}$ as a function of cone voltage.

Assignment of the other fragments observed in Figure 3.20 are given in Figure 3.21 (c) - (h) and for each fragment excellent agreement between the experimental isotopologue peak pattern intensities and m/z ratios with those calculated are obtained. With an increase in the applied cone voltage the abundance of the parent fragment decreases and the relative percentage of the lower oxidation state Pt species increase, through the stepwise reduction of $[\text{PtCl}_6]^{2-}$ in the gas phase.⁴⁷ The Pt complex in the m/z range of 333.838 - 341.838 corresponds to $[\text{Pt}^{\text{III}}\text{Cl}_4]^-$, Figure 3.21 (e), and gives supporting evidence for the existence of a Pt^{III} chlorido complex in the gas phase.

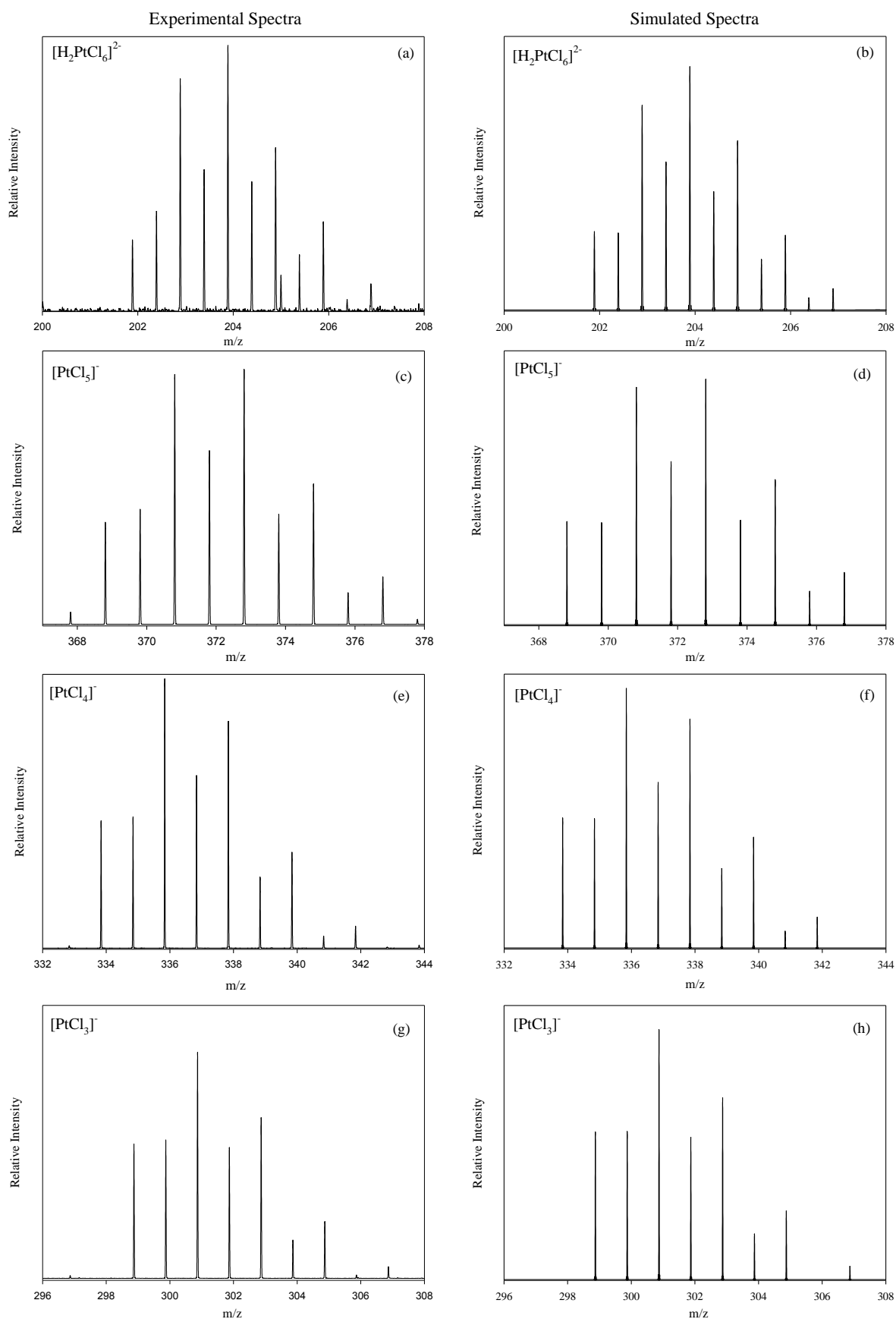


Figure 3.21: ESI-Mass Spectra of a $[\text{Pt}^{\text{IV}}\text{Cl}_6]^{2-}$ sample in acetonitrile. The experimental data for species (a) $[\text{Pt}^{\text{IV}}\text{Cl}_6]^{2-}$, (c) $[\text{Pt}^{\text{IV}}\text{Cl}_5]^-$, (e) $[\text{Pt}^{\text{III}}\text{Cl}_4]^-$ and (g) $[\text{Pt}^{\text{II}}\text{Cl}_3]^-$ is compared to their respective simulated spectra: (b) $[\text{Pt}^{\text{IV}}\text{Cl}_6]^{2-}$, (d) $[\text{Pt}^{\text{IV}}\text{Cl}_5]^-$, (f) $[\text{Pt}^{\text{III}}\text{Cl}_4]^-$ and (h) $[\text{Pt}^{\text{II}}\text{Cl}_3]^-$

3.7. Simulation of the ClO_3^- oxidation of a mixed $[\text{Pt}^{\text{II}}\text{Cl}_4]^{2-}$ and $[\text{Ir}^{\text{III}}\text{Cl}_6]^{3-}$ solution

The oxidation of $[\text{Pt}^{\text{II}}\text{Cl}_4]^{2-}$ with ClO_3^- ($4.25 \times 10^{-3} \text{ M}^{-1} \cdot \text{sec}^{-1}$)¹⁵ is approximately 50 times faster compared to the oxidation of $[\text{Ir}^{\text{III}}\text{Cl}_6]^{3-}$ with ClO_3^- ($8.25 \times 10^{-5} \text{ M}^{-1} \cdot \text{sec}^{-1}$)¹⁶. The redox reaction between $[\text{Ir}^{\text{IV}}\text{Cl}_6]^{2-}$ and $[\text{Pt}^{\text{II}}\text{Cl}_4]^{2-}$ will have a significant effect on the evolution of $[\text{Ir}^{\text{IV}}\text{Cl}_6]^{2-}$ and $[\text{Pt}^{\text{IV}}\text{Cl}_6]^{2-}$ as a function of time during the simultaneous oxidation of $[\text{Ir}^{\text{III}}\text{Cl}_6]^{3-}$ and $[\text{Pt}^{\text{II}}\text{Cl}_4]^{2-}$ with ClO_3^- . It has been established that the redox reaction rate between $[\text{Ir}^{\text{IV}}\text{Cl}_6]^{2-}$ and $[\text{Pt}^{\text{II}}\text{Cl}_4]^{2-}$ occurs at a rate of $k_1 = 6.60 \pm 0.46 \text{ M}^{-1} \cdot \text{sec}^{-1}$, which is much faster than the chlorate oxidation rates of both $[\text{Pt}^{\text{II}}\text{Cl}_4]^{2-}$ and $[\text{Ir}^{\text{III}}\text{Cl}_6]^{3-}$. Therefore, in a sample containing $[\text{Pt}^{\text{II}}\text{Cl}_4]^{2-}$, $[\text{Ir}^{\text{III}}\text{Cl}_6]^{3-}$ and ClO_3^- , as soon as $[\text{Ir}^{\text{IV}}\text{Cl}_6]^{2-}$ is formed through the ClO_3^- oxidation of $[\text{Ir}^{\text{III}}\text{Cl}_6]^{3-}$ the $[\text{Ir}^{\text{IV}}\text{Cl}_6]^{2-}$ will react with $[\text{Pt}^{\text{II}}\text{Cl}_4]^{2-}$ and be reduced back to $[\text{Ir}^{\text{III}}\text{Cl}_6]^{3-}$. This will result in a type of induction period in the formation of $[\text{Ir}^{\text{IV}}\text{Cl}_6]^{2-}$. Only after quantitative oxidation of $[\text{Pt}^{\text{II}}\text{Cl}_4]^{2-}$ will $[\text{Ir}^{\text{IV}}\text{Cl}_6]^{2-}$ be formed in relatively high concentrations. The simulation of the ClO_3^- oxidation of a mixture of $[\text{Pt}^{\text{II}}\text{Cl}_4]^{2-}$ and $[\text{Ir}^{\text{III}}\text{Cl}_6]^{3-}$ is shown in Figure 3.22.

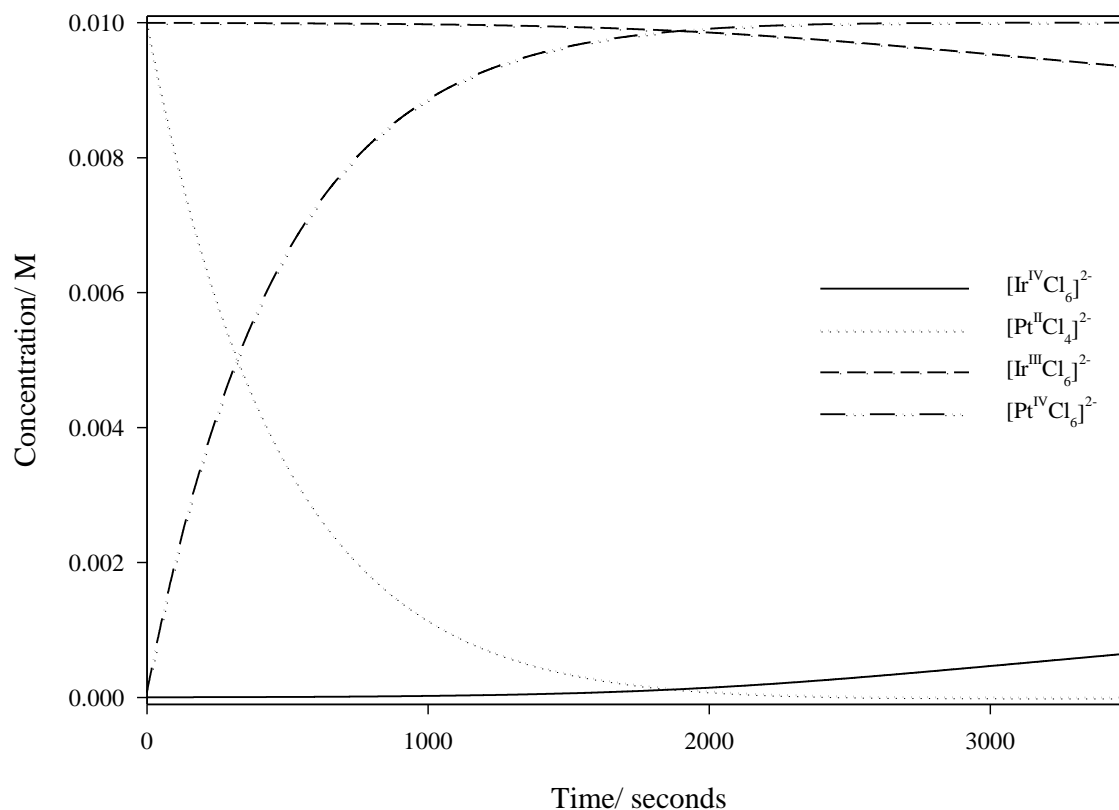


Figure 3.22: Simulation of the ClO_3^- oxidation of a mixture of $[\text{Pt}^{\text{II}}\text{Cl}_4]^{2-}$ and $[\text{Ir}^{\text{III}}\text{Cl}_6]^{3-}$ with the consideration of the redox reaction between $[\text{Pt}^{\text{II}}\text{Cl}_4]^{2-}$ and $[\text{Ir}^{\text{IV}}\text{Cl}_6]^{2-}$. An induction period for the formation of $[\text{Ir}^{\text{IV}}\text{Cl}_6]^{2-}$ can be observed.

The ClO_3^- oxidation of $[\text{Ir}^{\text{III}}\text{Cl}_6]^{3-}$ in the absence of $[\text{Pt}^{\text{II}}\text{Cl}_4]^{2-}$ was simulated to further illustrate the effect of the redox reaction between $[\text{Ir}^{\text{IV}}\text{Cl}_6]^{2-}$ and $[\text{Pt}^{\text{II}}\text{Cl}_4]^{2-}$ on the species evolution of $[\text{Pt}^{\text{IV}}\text{Cl}_6]^{2-}$ and $[\text{Ir}^{\text{IV}}\text{Cl}_6]^{2-}$ during the simultaneous ClO_3^- oxidation of $[\text{Pt}^{\text{II}}\text{Cl}_4]^{2-}$ and $[\text{Ir}^{\text{III}}\text{Cl}_6]^{3-}$, Figure 3.23. The trend obtained for the change in $[\text{Ir}^{\text{III}}\text{Cl}_6]^{3-}$ concentration in Figure 3.22 is illustrated in Figure 3.23 (a) and indicates that a distinct induction of the oxidation of $[\text{Ir}^{\text{III}}\text{Cl}_6]^{3-}$ is present. This is compared to the ClO_3^- oxidation of $[\text{Ir}^{\text{III}}\text{Cl}_6]^{3-}$ in the absence of $[\text{Pt}^{\text{II}}\text{Cl}_4]^{2-}$, Figure 3.23 (b), where no induction period is observed.

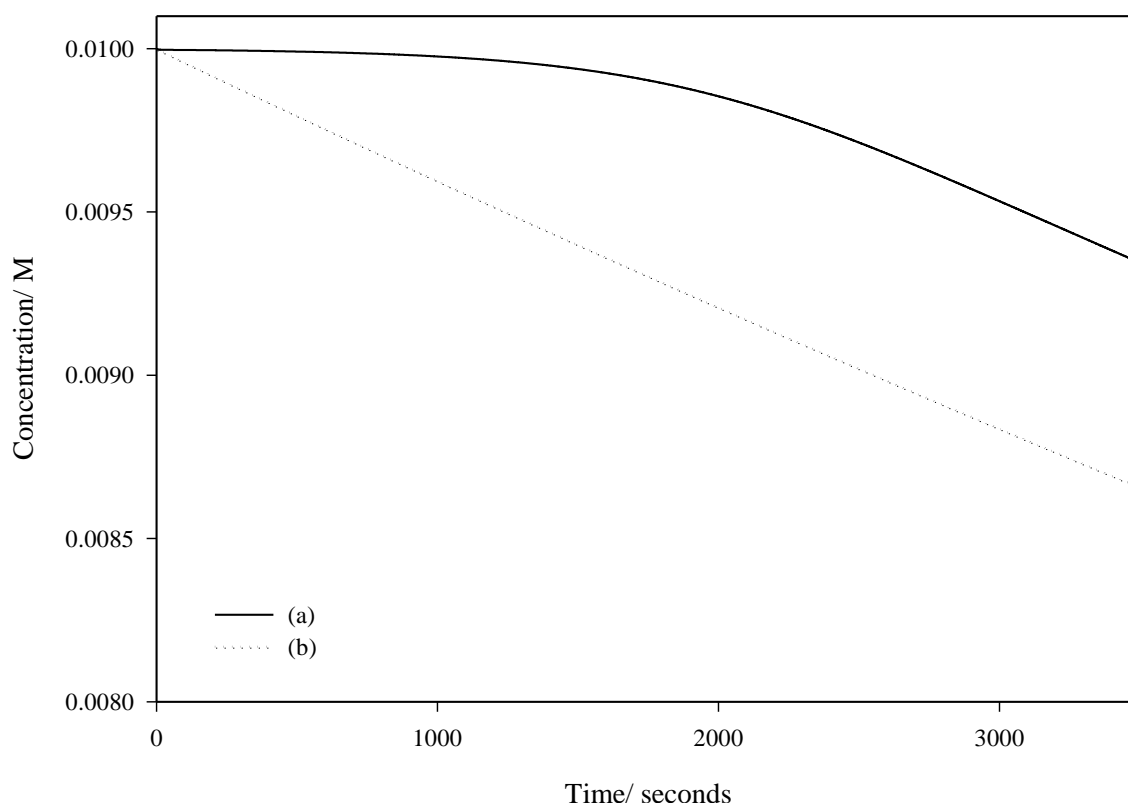


Figure 3.23: The effect of the redox reaction between $[\text{Ir}^{\text{IV}}\text{Cl}_6]^{2-}$ and $[\text{Pt}^{\text{II}}\text{Cl}_4]^{2-}$ on the species evolution of $[\text{Pt}^{\text{IV}}\text{Cl}_6]^{2-}$ and $[\text{Ir}^{\text{IV}}\text{Cl}_6]^{2-}$ during the simultaneous ClO_3^- oxidation of $[\text{Pt}^{\text{II}}\text{Cl}_4]^{2-}$ and $[\text{Ir}^{\text{III}}\text{Cl}_6]^{3-}$. (a) the change of $[\text{Ir}^{\text{III}}\text{Cl}_6]^{3-}$ concentration in the presence of $[\text{Pt}^{\text{II}}\text{Cl}_4]^{2-}$, (b) the change of $[\text{Ir}^{\text{III}}\text{Cl}_6]^{3-}$ concentration in the absence of $[\text{Pt}^{\text{II}}\text{Cl}_4]^{2-}$

3.8. Concluding remarks

By combining the reduction half cell potentials of $[\text{Ir}^{\text{IV}}\text{Cl}_6]^{2-}$ and $[\text{Pt}^{\text{IV}}\text{Cl}_6]^{2-}$, Reactions 3.3 and 3.4, the standard reaction Gibbs energy for Reaction 3.5 ($\Delta G^0_{\text{rxn}} = -42.45 \text{ kJ. mol}^{-1}$) was calculated. The large negative ΔG^0_{rxn} indicates that spontaneous oxidation of $[\text{Pt}^{\text{II}}\text{Cl}_4]^{2-}$ will take place in the presence of $[\text{Ir}^{\text{IV}}\text{Cl}_6]^{2-}$. The balanced redox reaction of $[\text{Ir}^{\text{IV}}\text{Cl}_6]^{2-}$ and $[\text{Pt}^{\text{II}}\text{Cl}_4]^{2-}$, Reaction 3.5, yields a stoichiometric relationship of 2 $[\text{Ir}^{\text{IV}}\text{Cl}_6]^{2-}$: 1 $[\text{Pt}^{\text{II}}\text{Cl}_4]^{2-}$. This stoichiometric relationship was verified by monitoring the UV-Vis spectral changes of the redox reaction as a function of time, Figure 3.2 and 3.3, until equilibrium was reached. The molar extinction coefficients of the reagent and product species were experimentally determined at 488 nm, Figure 3.1 (a) - (d). The $[\text{Ir}^{\text{IV}}\text{Cl}_6]^{2-}$ complex anion has a relatively large molar extinction coefficient compared to $[\text{Pt}^{\text{II}}\text{Cl}_4]^{2-}$, $[\text{Pt}^{\text{IV}}\text{Cl}_6]^{2-}$ and $[\text{Ir}^{\text{IV}}\text{Cl}_6]^{3-}$ which allows

for the ‘direct’ determination of the $[\text{Ir}^{\text{IV}}\text{Cl}_6]^{2-}$ species concentration during a kinetic run at 488 nm.

The kinetic study as a function of reagent concentration ($[\text{Pt}^{\text{II}}\text{Cl}_4]^{2-}$ and $[\text{Ir}^{\text{IV}}\text{Cl}_6]^{2-}$) illustrates that the reaction rate is dependent on the concentration of both species, with an increase in the rate observed as the concentration of either $[\text{Ir}^{\text{IV}}\text{Cl}_6]^{2-}$ or $[\text{Pt}^{\text{II}}\text{Cl}_4]^{2-}$ is increased, Figures 3.4 and 3.5. Moreover, the redox reaction is first order with respect to both $[\text{Ir}^{\text{IV}}\text{Cl}_6]^{2-}$ and $[\text{Pt}^{\text{II}}\text{Cl}_4]^{2-}$. An increase in temperature increases the reaction rate, Figure 3.7, whereas an increase in acid concentration has a negligible effect on the reaction rate, Figure 3.8. It was found that the redox reaction is not acid catalysed. Increasing the ionic strength considerably enhances the reaction rate, Figure 3.7, and it is postulated that the Na^+ ions form solvent-separated ion-pairs with the reagents. These solvent-separated ion-pairs decrease the activation Gibbs energy barrier (ΔG^\ddagger) by decreasing the repulsion between the reactants. Reactions 3.12 and 3.13, was used to derive the multi-step reaction redox rate model, Equations 3.14 - 3.18. With this rate model consistent rate constants for k_1 ($7.04 \pm 0.34 \text{ M}^{-2}.\text{sec}^{-1}$) and consistent molar extinction coefficient for the $[\text{Ir}^{\text{IV}}\text{Cl}_6]^{2-}$ species ($4003 \pm 63 \text{ M}^{-1}.\text{cm}^{-1}$) were obtained. However, inconsistent k_2 values ($k_2 = 2002.67 \pm 6300.18 \text{ M}^{-2}.\text{sec}^{-1}$) were calculated. Taking into account that the Pt^{III} species is highly reactive the steady state approximation, Equations 3.19 - 3.21, was applied and resulted in the diffusion limited rate model, Equations 3.22 - 3.25. The calculated rate constant ($k_1 = 6.60 \pm 0.46 \text{ M}^{-1}.\text{sec}^{-1}$) and molar extinction coefficient for $[\text{Ir}^{\text{IV}}\text{Cl}_6]^{2-}$ ($\epsilon = 4258 \pm 209 \text{ M}^{-1}.\text{cm}^{-1}$) obtained with the diffusion controlled rate model were consistent and compared well with those obtained by the multi-step reaction rate model, Equations 3.14 - 3.18. Furthermore, the assumption that $k_2 \gg k_1$ is verified by the consistency of the calculated values and the excellent least squares fits, Figures 3.12 and 3.13, to the data. The calculated rate constants (k_1) at different temperatures were used to construct an Eyring plot, Figure 3.19. A linear trend was obtained, validating the diffusion controlled rate model. The gradient and intercept of the Eyring plot were used to determine the enthalpy of activation ($\Delta H^\ddagger = 36.65 \pm 0.24 \text{ kJ.mol}^{-1}$) and entropy of activation ($\Delta S^\ddagger = -107.76 \pm 0.87 \text{ J.mol}^{-1}.\text{K}^{-1}$) and the Gibbs energy of activation was calculated using Equation 3.28, ($\Delta G^\ddagger = 68.77 \pm 0.15 \text{ kJ.mol}^{-1}$ at 298.1K). The relatively large negative value obtained for ΔS^\ddagger is indicative of a reaction that occurs *via* an associative mechanism. In addition, the good fits obtained with the diffusion controlled rate model prove the formation and subsequent reaction of a Pt^{III} species during Reactions 3.12 and 3.13. The redox reaction

between $[\text{Ir}^{\text{IV}}\text{Cl}_6]^{2-}$ and $[\text{Pt}^{\text{II}}\text{Cl}_4]^{2-}$ will have a significant influence on the $[\text{Ir}^{\text{IV}}\text{Cl}_6]^{2-}$ and $[\text{Pt}^{\text{IV}}\text{Cl}_6]^{2-}$ product formation during the simultaneous oxidation of $[\text{Pt}^{\text{II}}\text{Cl}_4]^{2-}$ and $[\text{Ir}^{\text{III}}\text{Cl}_6]^{3-}$ with ClO_3^- . The rate of $[\text{Ir}^{\text{III}}\text{Cl}_6]^{3-}$ oxidation with ClO_3^- ($8.25 \times 10^{-5} \text{ M}^{-1} \cdot \text{sec}^{-1}$) is much slower than the reduction of $[\text{Ir}^{\text{IV}}\text{Cl}_4]^{2-}$ by $[\text{Pt}^{\text{II}}\text{Cl}_4]^{2-}$ ($k_1 = 6.60 \pm 0.46 \text{ M}^{-1} \cdot \text{sec}^{-1}$) which implies that in a mixed $[\text{Ir}^{\text{III}}\text{Cl}_6]^{3-}$, $[\text{Pt}^{\text{II}}\text{Cl}_4]^{2-}$ and ClO_3^- sample, $[\text{Ir}^{\text{IV}}\text{Cl}_6]^{2-}$ will only form after complete oxidation of $[\text{Pt}^{\text{II}}\text{Cl}_4]^{2-}$ to $[\text{Pt}^{\text{IV}}\text{Cl}_6]^{2-}$. This is shown in the simulation of this reaction system, Figures 3.22 and 3.23

Evidence for the existence of a Pt^{III} chlorido complex in the gas-phase was obtained by direct infusion ESI-Q-TOF-MS analysis of $[\text{Pt}^{\text{IV}}\text{Cl}_6]^{2-}$. The analysis was carried out over a cone voltage range of 15 - 100 V. The extent of $[\text{Pt}^{\text{IV}}\text{Cl}_6]^{2-}$ fragmentation increases as the cone voltage is raised. The doubly charged complex $[\text{H}_2\text{Pt}^{\text{II}}\text{Cl}_6]^{2-}$ was assigned based on the isotopologue peak pattern and high resolution m/z data at 201.891 - 206.889.

Chapter 4

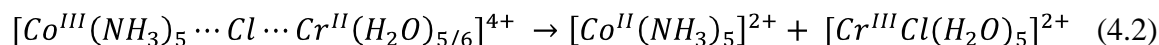
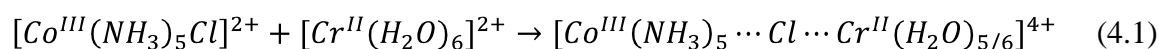
A mechanistic investigation of the first oxidation reaction of
 $[\text{Pt}^{\text{II}}\text{Cl}_4]^{2-}$ by $[\text{Ir}^{\text{IV}}\text{Cl}_6]^{2-}$

4

A mechanistic investigation of the first oxidation reaction of [Pt^{II}Cl₄]²⁻ by [Ir^{IV}Cl₆]²⁻

4.1. Introduction

In the 1950's Taube and co-workers investigated the mechanistic aspects of several redox reactions between transition metal complexes, *e.g.* the reduction of [Co^{III}(NH₃)₅Cl]²⁺ with complexes containing Fe^{II} and Cr^{II} metal centers.^{19,48,49} In one of these studies, it was shown that the *kinetically labile* [Cr^{II}(H₂O)₆]²⁺ complex cation reacts with the *kinetically inert* [Co^{III}(NH₃)₅Cl]²⁺ complex cation to form the [Cr^{III}Cl(H₂O)₅]²⁺ and [Co^{II}(NH₃)₅]²⁺ species. According to Taube and Myers, the chloride bound to Co^{III} was transferred from the [Co^{III}(NH₃)₅Cl]²⁺ complex through a chloride bridged intermediate, Reactions 4.1 and 4.2.¹⁹



In the following 2 decades the interest in this topic of halide bridged intermediates steadily increased⁵⁰⁻⁵⁴ with the largest emphasis on the Pt^{II} - Pt^{IV} redox system, Reactions 3.1 and 3.2.^{32-36,55} It is postulated that halide bridged intermediates decreases the Gibbs energy activation barrier for electron transfer.⁵⁶

Furthermore, this process circumvents the formation of high-energy intermediates as is exemplified by the reduction rate of $[\text{Co}^{\text{III}}(\text{NH}_3)_5\text{Cl}]^{2+}$, Reactions 4.1 and 4.2, which is approximately 10^{11} times larger than the outer sphere reduction of $[\text{Co}^{\text{III}}(\text{NH}_3)_6]^{3+}$ with $[\text{Cr}^{\text{II}}(\text{H}_2\text{O})_6]^{2+}$.^{54,56}

The temperature dependence investigation of the first redox reaction step between $[\text{Ir}^{\text{IV}}\text{Cl}_6]^{2-}$ and $[\text{Pt}^{\text{II}}\text{Cl}_4]^{2-}$, Reaction 3.12, yielded a negative entropy of activation ($\Delta S^\ddagger = -107.76 \pm 0.87 \text{ J}\cdot\text{mol}^{-1}\cdot\text{K}^{-1}$). This relatively large negative ΔS^\ddagger value is indicative of an associative reaction mechanism and supports the notion that the reaction between $[\text{Pt}^{\text{II}}\text{Cl}_4]^{2-}$ and $[\text{Ir}^{\text{IV}}\text{Cl}_6]^{2-}$ proceeds via a chloride bridged intermediate. If chloride transfer from $[\text{Ir}^{\text{IV}}\text{Cl}_6]^{2-}$ to $[\text{Pt}^{\text{II}}\text{Cl}_4]^{2-}$ does not take place during this reaction, the product species that form in chloride deficient matrices will be $[\text{Ir}^{\text{III}}\text{Cl}_6]^{3-}$ and *trans*- $[\text{Pt}^{\text{II}}\text{Cl}_4(\text{H}_2\text{O})_2]$. On the contrary, if the reduction of $[\text{Ir}^{\text{IV}}\text{Cl}_6]^{2-}$ by $[\text{Pt}^{\text{II}}\text{Cl}_4]^{2-}$ proceeds via a chloride transfer mechanism, the product species are expected to be $[\text{Ir}^{\text{III}}\text{Cl}_5(\text{H}_2\text{O})]^{2-}$ and $[\text{Pt}^{\text{IV}}\text{Cl}_6]^{2-}$. In order to ascertain whether chloride transfer occurs it is the aim of this chapter to develop an IP-HPLC method to unambiguously identify the Ir^{III} and Pt^{IV} product species that form during the reaction of $[\text{Ir}^{\text{IV}}\text{Cl}_6]^{2-}$ and $[\text{Pt}^{\text{II}}\text{Cl}_4]^{2-}$, Reaction 3.12, in a chloride deficient matrix. However, in the time span that reduction takes place aquation can also occur and therefore the rate of aquation with respect to the $[\text{Pt}^{\text{II}}\text{Cl}_4]^{2-}$, $[\text{Pt}^{\text{IV}}\text{Cl}_6]^{2-}$, $[\text{Ir}^{\text{IV}}\text{Cl}_6]^{2-}$ and $[\text{Ir}^{\text{III}}\text{Cl}_6]^{3-}$ complex anions were also investigated.

4.2. Aquation kinetics of $[\text{Pt}^{\text{II}}\text{Cl}_4]^{2-}$, $[\text{Pt}^{\text{IV}}\text{Cl}_6]^{2-}$ and $[\text{Ir}^{\text{IV}}\text{Cl}_6]^{2-}$.

Lars I. Elding has extensively studied the aquation of $[\text{Pt}^{\text{II}}\text{Cl}_4]^{2-}$ in acidic matrices, Reactions 4.3 and 4.4.³⁹ In a 0.50 M HCl matrix the extent of aquation is limited and at equilibrium ($K_{\text{eq}} = 1.30 \times 10^{-2}$) only 2.5% of $[\text{Pt}^{\text{II}}\text{Cl}_4]^{2-}$ aquates to form the $[\text{Pt}^{\text{II}}\text{Cl}_3(\text{H}_2\text{O})]^-$ complex anion with no higher aquated species detected.³⁹ At HCl concentrations above 0.10 M, further aquation of $[\text{Pt}^{\text{II}}\text{Cl}_3(\text{H}_2\text{O})]^-$ is negligible, Reaction 4.4. The aquation (k_a) and anation (k_{-a}) rate constants for Reaction 4.3 (at 0.5 M HClO_4) reported by Elding are: $k_a = 3.69 \times 10^{-5} \text{ sec}^{-1}$, $k_{-a} = 2.81 \times 10^{-3} \text{ M}^{-1}\cdot\text{sec}^{-1}$ and a concentration time profile is shown in Figure 4.1.

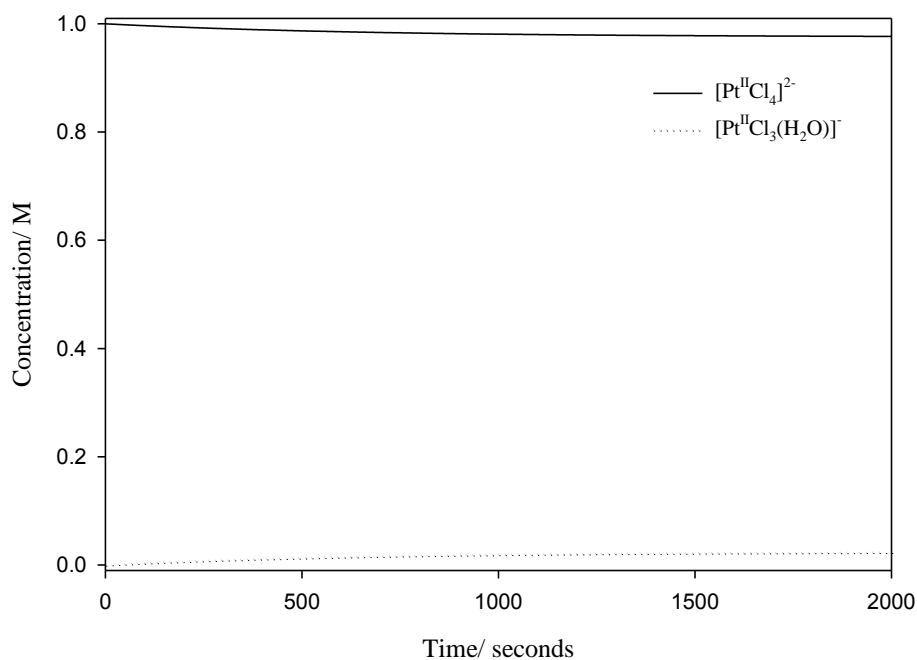
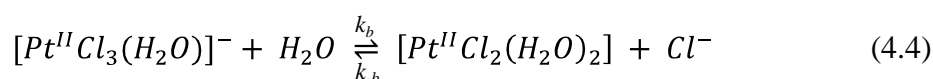
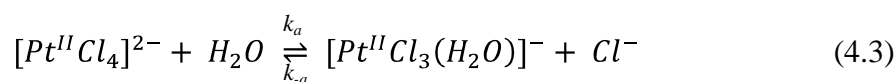


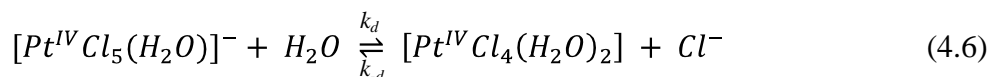
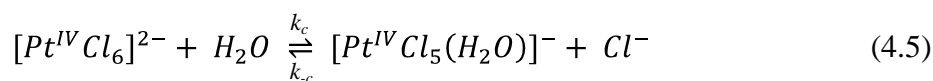
Figure 4.1: Simulation illustrating the aquation of $[\text{Pt}^{\text{II}}\text{Cl}_4]^{2-}$ and anation of $[\text{Pt}^{\text{IV}}\text{Cl}_5(\text{H}_2\text{O})]^-$, Equation 4.3, in 0.5 M HClO_4 .

Figure 4.1 shows that aquation of the $[\text{Pt}^{\text{II}}\text{Cl}_4]^{2-}$ complex in 0.5 M HClO_4 is relatively slow and that only 3 % $[\text{Pt}^{\text{IV}}\text{Cl}_5(\text{H}_2\text{O})]^-$ forms in a timeframe of 1500 seconds (25 minutes).



Several investigations report that the aquation of $[\text{Pt}^{\text{IV}}\text{Cl}_6]^{2-}$ in acidic media is relatively slow.⁵⁷⁻⁶¹ After dissolution of Na_2PtCl_6 crystals in water we found that after 5 hours no aquated species could be detected using UV-Vis and ^{195}Pt NMR.⁶² However, the effect of light on this reaction rate has been the topic of many investigations^{42,58-61} and it has been shown that when $[\text{Pt}^{\text{IV}}\text{Cl}_6]^{2-}$ is irradiated at 313 nm a significant enhancement in the rate of aquation is observed. In addition, the aquation rate of $[\text{Pt}^{\text{IV}}\text{Cl}_6]^{2-}$ significantly increases in the presence of $[\text{Pt}^{\text{II}}\text{Cl}_4]^{2-}$ ($k \approx 5 \times 10^5 \text{ sec}^{-1}$).^{32,36,41} Koch *et.al.* determined the stability constants for Reactions 4.5 and 4.6 as $\log(k_c/k_{-c}) = 1.75 \pm 0.05$ and $\log(k_d/k_{-d}) = 2.71 \pm 0.15$ respectively.⁵⁷ At equilibrium the $[\text{Pt}^{\text{IV}}\text{Cl}_6]^{2-}$ fraction is equal to 0.85 and the fraction of

$[\text{Pt}^{\text{IV}}\text{Cl}_5(\text{H}_2\text{O})]^-$ is equal to 0.14 (in a 0.10 M HCl matrix) with the higher aquated species contributing less than 0.01.

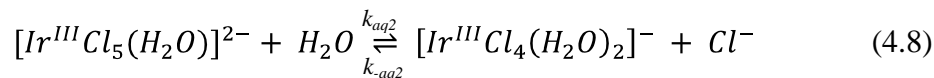
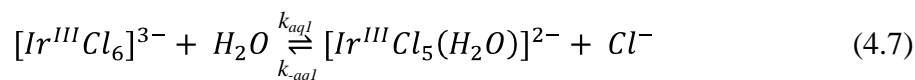


The $[\text{Ir}^{\text{IV}}\text{Cl}_6]^{2-}$ complex in low concentration HCl matrices is indefinitely stable. It was shown, spectrophotometrically, that acidic solutions of $[\text{Ir}^{\text{IV}}\text{Cl}_6]^{2-}$ at room temperature, does not undergo any significant changes in a timeframe of at least seven days.⁶³ However, in the presence of light (254 nm) $[\text{Ir}^{\text{IV}}\text{Cl}_6]^{2-}$ will rapidly aquate and can also reduce to form a mixture of $[\text{Ir}^{\text{IV}}\text{Cl}_5(\text{H}_2\text{O})]^-$ and $[\text{Ir}^{\text{III}}\text{Cl}_6]^{3-}$.⁶⁴

4.3. IP-HPLC study of the aquation kinetics of $[\text{Ir}^{\text{III}}\text{Cl}_6]^{3-}$ and $[\text{Ir}^{\text{III}}\text{Cl}_5(\text{H}_2\text{O})]^{2-}$

The aquation kinetics of $[\text{Ir}^{\text{III}}\text{Cl}_6]^{3-}$ and $[\text{Ir}^{\text{III}}\text{Cl}_5(\text{H}_2\text{O})]^{2-}$ in well-defined acidic, chloride rich matrices were investigated previously.^{38,65,66} However, due to small differences in the UV-Vis spectra of $[\text{Ir}^{\text{III}}\text{Cl}_6]^{3-}$ and $[\text{Ir}^{\text{III}}\text{Cl}_5(\text{H}_2\text{O})]^{2-}$, separation of the Ir^{III} species was required (using ion-exchange columns) before analysis. Moreover, the resulting Ir^{III} fractions were then oxidized with Cl_2 gas to form the corresponding Ir^{IV} species and subsequently analyzed with UV-Vis spectroscopy. An alternative analysis method to determine the aquation rate of $[\text{Ir}^{\text{III}}\text{Cl}_6]^{3-}$ was reported by Domingos *et. al.*⁶⁷ The $[\text{Ir}^{\text{III}}\text{Cl}_n(\text{H}_2\text{O})_{6-n}]^{3-n}$ ($n = 4-6$) series of complex anions were separated with paper electrophoresis, followed by quantification through neutron activation. Although this is a tedious and time consuming process to obtain the required results the necessity of oxidizing Ir^{III} is removed.

In light of the importance of the aquation rates of $[\text{Ir}^{\text{III}}\text{Cl}_6]^{3-}$ and $[\text{Ir}^{\text{III}}\text{Cl}_5(\text{H}_2\text{O})]^{2-}$, Reactions 4.7 and 4.8, with respect to deducing the redox reaction mechanism and the relatively large differences between reported $k_{\text{aq}1}$ and $k_{\text{aq}2}$, Table 4.1, an IP-HPLC method was developed (*see* Chapter 2.2.3) for the rapid quantification of the $[\text{Ir}^{\text{III}}\text{Cl}_n(\text{H}_2\text{O})_{6-n}]^{3-n}$ ($n = 4-6$) species.



4.3.1. Tentative assignment of the IP-HPLC chromatographic trace of the $[\text{Ir}^{\text{III}}\text{Cl}_n(\text{H}_2\text{O})_{n-6}]^{3-n}$ ($n=4-6$) series of complex anions.

$\text{K}_3\text{IrCl}_6 \cdot x\text{H}_2\text{O}$ was dissolved in a solution consisting of 4.0 M NaCl and 0.1 M HCl and stored at 295.1 K for 33 days to ensure that equilibrium is reached. At equilibrium it is expected that approximately 55% of the iridium will be in the $[\text{Ir}^{\text{III}}\text{Cl}_6]^{3-}$ form ($K_{\text{eq}} = 0.295$ at 3.4 M HCl)³⁸. The sample was subsequently diluted (x15) and immediately injected onto the C_{18} column, Figure 4.2 (a) and (b).

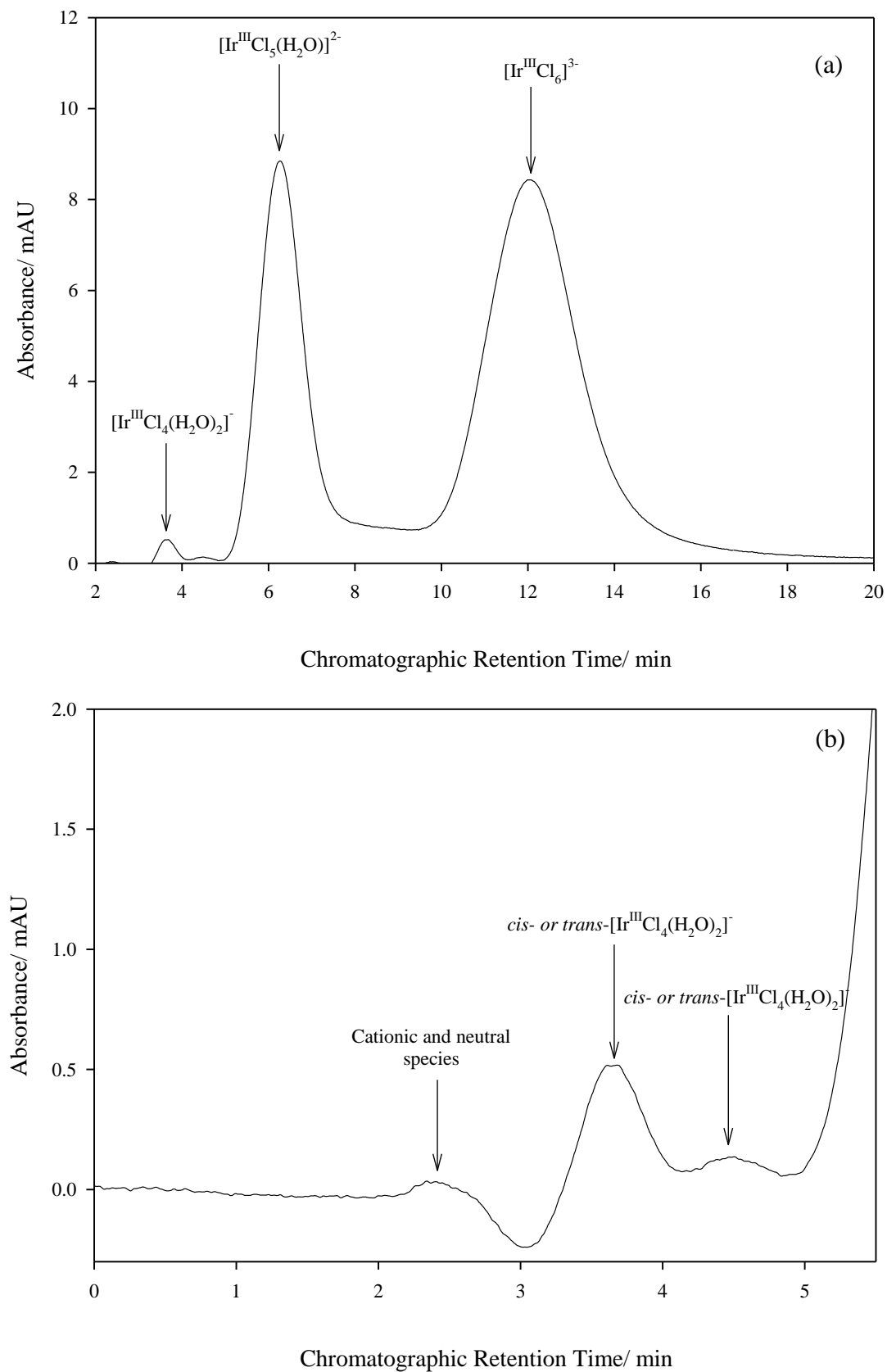


Figure 4.2: IP-HPLC separation of the $[\text{Ir}^{\text{III}}\text{Cl}_n(\text{H}_2\text{O})_{n-6}]^{3-n}$ ($n = 4-6$) series of complex anions in 4.1 M chloride after 33 days (4.0 M NaCl and 0.1 M HCl) detected at 254 nm. (a) shows the complete chromatogram and (b) shows the higher aquated species present at relatively low concentrations.

The chromatographic trace of the sample containing the $[\text{Ir}^{\text{III}}\text{Cl}_n(\text{H}_2\text{O})_{n-6}]^{3-n}$ ($n=4-6$) series of complex anions exhibits five distinct peaks, Figure 4.2 (a) and (b). The chromatographic trace was tentatively assigned based on the predicted elution order of the $[\text{Ir}^{\text{III}}\text{Cl}_n(\text{H}_2\text{O})_{n-6}]^{3-n}$ ($n=4-6$) series of complex anions as governed by the overall charge of each species.²⁶ The first peak eluting at 2.4 minutes is assumed to contain the neutral and positively charged species since no retention is observed. Two small peaks are observed at retention times of 3.7 and 4.5 minutes, Figure 4.2 (b), postulated to be the stereoisomers *cis*- $[\text{Ir}^{\text{III}}\text{Cl}_4(\text{H}_2\text{O})_2]^-$ and *trans*- $[\text{Ir}^{\text{III}}\text{Cl}_4(\text{H}_2\text{O})_2]^-$. It could not be experimentally determined which stereoisomer elutes first. However, based on their dipole moments we expect that *trans*- $[\text{Ir}^{\text{III}}\text{Cl}_4(\text{H}_2\text{O})_2]^-$ would elute before *cis*- $[\text{Ir}^{\text{III}}\text{Cl}_4(\text{H}_2\text{O})_2]^-$ species. The peaks eluting at 6.3 and 12.9 minutes are tentatively assigned to the $[\text{Ir}^{\text{III}}\text{Cl}_5(\text{H}_2\text{O})]^{2-}$ and $[\text{Ir}^{\text{III}}\text{Cl}_6]^{3-}$ species respectively. The UV-Vis signal in the region of the chromatogram between the $[\text{Ir}^{\text{III}}\text{Cl}_5(\text{H}_2\text{O})]^{2-}$ and $[\text{Ir}^{\text{III}}\text{Cl}_6]^{3-}$ species (7.5 – 10 minutes), Figure 4.2 (a), does not return to baseline. This is attributed to the interconversion of $[\text{Ir}^{\text{III}}\text{Cl}_6]^{3-}$ to $[\text{Ir}^{\text{III}}\text{Cl}_5(\text{H}_2\text{O})]^{2-}$, Reaction 4.7, in the column.

4.3.2. Kinetic investigation of the aquation of $[\text{Ir}^{\text{III}}\text{Cl}_6]^{3-}$ and $[\text{Ir}^{\text{III}}\text{Cl}_5(\text{H}_2\text{O})]^{2-}$.

The kinetic investigation regarding the aquation rates of $[\text{Ir}^{\text{III}}\text{Cl}_6]^{3-}$ and $[\text{Ir}^{\text{III}}\text{Cl}_5(\text{H}_2\text{O})]^{2-}$, Reactions 4.7 and 4.8, was done by preparation of a fresh 8.09 mM $[\text{Ir}^{\text{III}}\text{Cl}_6]^{3-}$ sample in a 0.10 M HCl matrix. At regular time intervals this sample was diluted 15 fold and injected onto the column under optimized IP-HPLC conditions and at a constant temperature of 295.1 K, Figure 4.3. The experiment was carried out over a timeframe of 22 000 minutes and the Ir^{III} species were detected by UV-Vis at 254 nm.

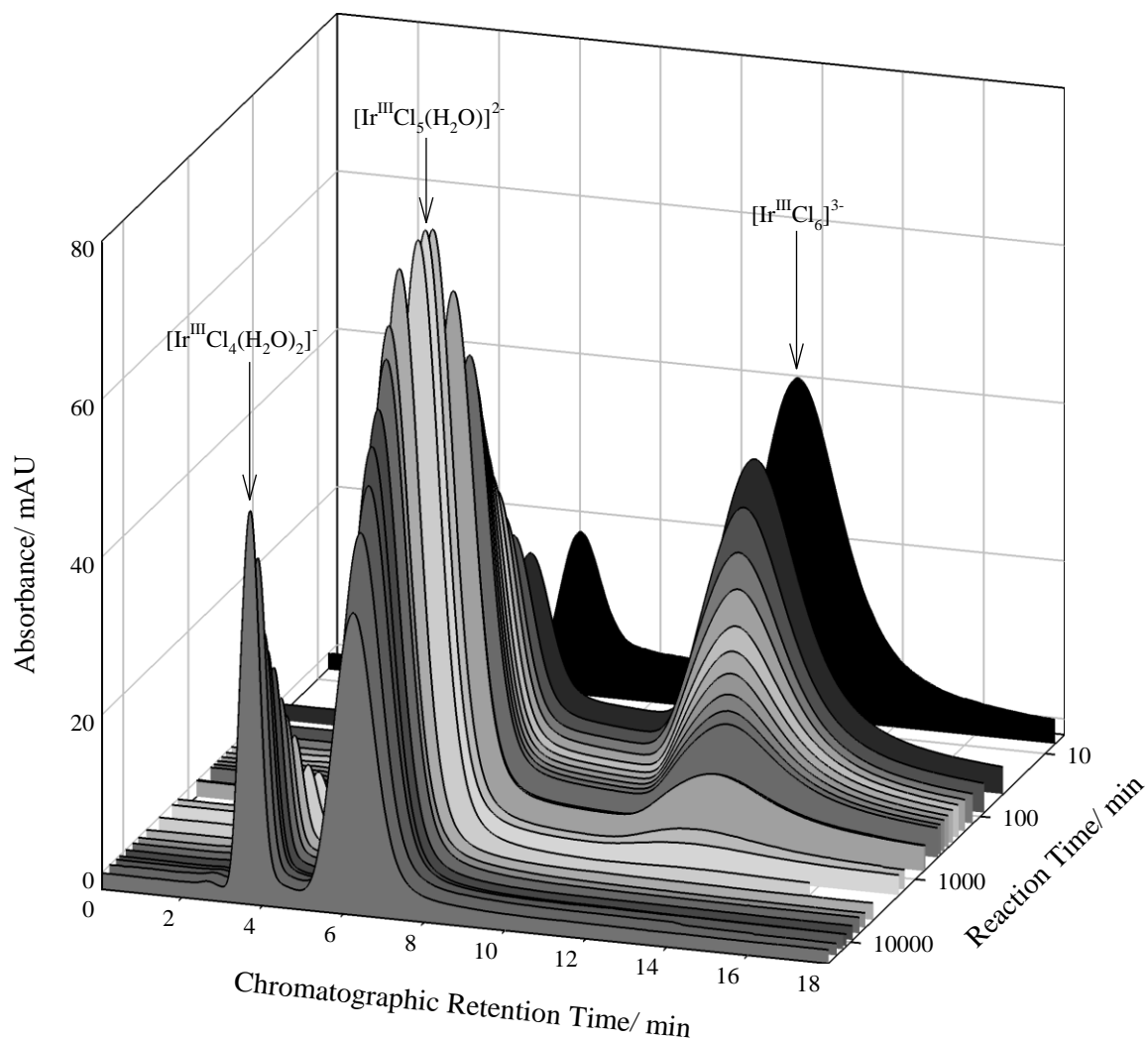
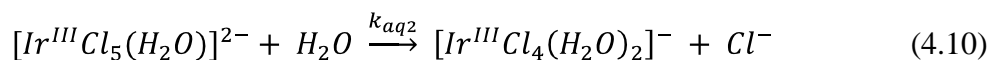
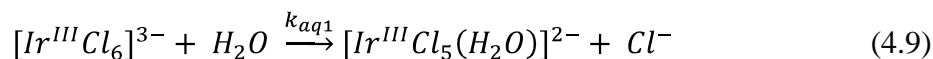


Figure 4.3: The change in the $[\text{Ir}^{\text{III}}\text{Cl}_n(\text{H}_2\text{O})_{n-6}]^{3-n}$ ($n = 4-6$) series of complex anion amounts as a function of time at 295.1. (Note: Reaction Time illustrated on a logarithmic scale)

From the chromatographic data in Figure 4.3 it is clear that the peak area at 12.9 minutes decrease with increasing reaction time. This gradual decrease is accompanied by an increase in the peak area at 6.3 minutes, followed by a subsequent decrease in this peak area at an approximate reaction time of 2800 minutes. Furthermore, the decrease in the peak area at 6.3 minutes is associated with an increase in the peak area at 3.7 minutes. This trend corresponds to the sequential aquation of $[\text{Ir}^{\text{III}}\text{Cl}_6]^{3-}$, Reaction 4.7, to $[\text{Ir}^{\text{III}}\text{Cl}_5(\text{H}_2\text{O})]^{2-}$ which further aquates to $[\text{Ir}^{\text{III}}\text{Cl}_4(\text{H}_2\text{O})_2]^-$, Reaction 4.8. After a reaction time of 2800 minutes the $[\text{Ir}^{\text{III}}\text{Cl}_6]^{3-}$ concentration is insignificantly small and it can thus be assumed that the anation of $[\text{Ir}^{\text{III}}\text{Cl}_5(\text{H}_2\text{O})]^{2-}$ is negligible in 0.1 M HCl. Literature reports that in 0.1 M HCl anation of $[\text{Ir}^{\text{III}}\text{Cl}_5(\text{H}_2\text{O})]^{2-}$ and $[\text{Ir}^{\text{III}}\text{Cl}_4(\text{H}_2\text{O})_2]^-$ does not occur and confirms our observations.^{38,67} In the absence of significant anation the aquation reactions of $[\text{Ir}^{\text{III}}\text{Cl}_6]^{3-}$ and $[\text{Ir}^{\text{III}}\text{Cl}_5(\text{H}_2\text{O})]^{2-}$ can therefore be rewritten as, Reactions 4.9 and 4.10.



Reactions 4.9 and 4.10 were used to construct the pseudo-first order aquation rate model, Equations 4.11 - 4.13, for the determination of the rate constants $k_{\text{aq}1}$ and $k_{\text{aq}2}$.

$$\frac{d[\text{Ir}^{\text{III}}\text{Cl}_6]^{3-}}{dt} = -k_{\text{aq}1}[\text{Ir}^{\text{III}}\text{Cl}_6]^{3-} \quad (4.11)$$

$$\frac{d[\text{Ir}^{\text{III}}\text{Cl}_5(\text{H}_2\text{O})]^{2-}}{dt} = k_{\text{aq}1}[\text{Ir}^{\text{III}}\text{Cl}_6]^{3-} - k_{\text{aq}2}[\text{Ir}^{\text{III}}\text{Cl}_5(\text{H}_2\text{O})]^{2-} \quad (4.12)$$

$$\frac{d[\text{Ir}^{\text{III}}\text{Cl}_4(\text{H}_2\text{O})_2]^-}{dt} = k_{\text{aq}2}[\text{Ir}^{\text{III}}\text{Cl}_5(\text{H}_2\text{O})]^{2-} \quad (4.13)$$

Using the program *Sigmaplot - Peakfit*, each chromatographic peak in Figure 4.3 was integrated. The peak areas of $[\text{Ir}^{\text{III}}\text{Cl}_6]^{3-}$ and $[\text{Ir}^{\text{III}}\text{Cl}_4(\text{H}_2\text{O})_2]^-$ at a reaction time of 2800 minutes is negligibly small compared to the peak area of $[\text{Ir}^{\text{III}}\text{Cl}_5(\text{H}_2\text{O})]^{2-}$. It can therefore be assumed that all the Ir^{III} is in the form of $[\text{Ir}^{\text{III}}\text{Cl}_5(\text{H}_2\text{O})]^{2-}$ and that this peak area is proportional to the total Ir^{III} concentration. Note, for the first chromatographic run, with a reaction time of 5 min, that only $[\text{Ir}^{\text{III}}\text{Cl}_6]^{3-}$ and $[\text{Ir}^{\text{III}}\text{Cl}_5(\text{H}_2\text{O})]^{2-}$ are present. Similarly for the last chromatographic run only $[\text{Ir}^{\text{III}}\text{Cl}_5(\text{H}_2\text{O})]^{2-}$ and $[\text{Ir}^{\text{III}}\text{Cl}_4(\text{H}_2\text{O})_2]^-$ are present in relatively large amounts. It is therefore possible using a peak area ratio calculation to obtain the $[\text{Ir}^{\text{III}}\text{Cl}_6]^{3-}$, $[\text{Ir}^{\text{III}}\text{Cl}_5(\text{H}_2\text{O})]^{2-}$ and $[\text{Ir}^{\text{III}}\text{Cl}_4(\text{H}_2\text{O})_2]^-$ species concentration as a function of time, Figure 4.4. The program *Equikin*^{26,27} was used to simulate the pseudo-first order aquation rate model and the non-linear least-squares fits to the experimental data are excellent, Figure 4.4. The calculated rate constants agree quantitatively with those reported by Domingos *et al.*⁶⁷, Table 4.1. However, rate constants reported by Garner *et al.*^{38,65} are not a good match but still within the experimental error range given by Garner *et al.* (± 0.6). It should also be noted that the ionic strength employed by Garner *et al.* is significantly higher compared to our and Domingos' study.⁶⁷ Furthermore, the good correlation between the calculated rate constants ($k_{\text{aq}1}$, $k_{\text{aq}2}$) and the corresponding rate constants reported in literature, Table 4.1, prove that the tentative peak assignment given in Figure 4.2 (a) and (b) are correct.

$$\frac{A_{[\text{Ir}^{\text{III}}\text{Cl}_5(\text{H}_2\text{O})]^-} \text{ at } t_{2800}}{A_{[\text{Ir}^{\text{III}}\text{Cl}_5(\text{H}_2\text{O})]^-} \text{ at } t_x} = \frac{\text{Total } C_{\text{Ir}^{\text{III}}}}{C_{[\text{Ir}^{\text{III}}\text{Cl}_5(\text{H}_2\text{O})]^-} \text{ at } t_x} \quad (4.14)$$

Table 4.1: Calculated rate constants obtained with the pseudo-first order rate model, Equations 4.11 - 4.13, compared to rate constants reported in literature.

Source	Ionic strength/ M	$k_{\text{aq1}}/\text{sec}^{-1}$	$k_{\text{aq2}}/\text{sec}^{-1}$
This study	0.102	$3.50 (\pm 0.12) \times 10^{-5}$	$1.14 (\pm 0.10) \times 10^{-6}$
Domingos <i>et. al.</i> ⁶⁷	0.130	$3.40 (\pm 0.05) \times 10^{-5}$	$1.19 (\pm 0.03) \times 10^{-6}$
Garner <i>et. al.</i> ^{38,65}	2.200	$9.4 (\pm 0.6) \times 10^{-6}$	$8 (\pm 7) \times 10^{-7}$

^a Poulson and Garner³⁸

^β Chang and Garner⁶⁵ at 298.1 K

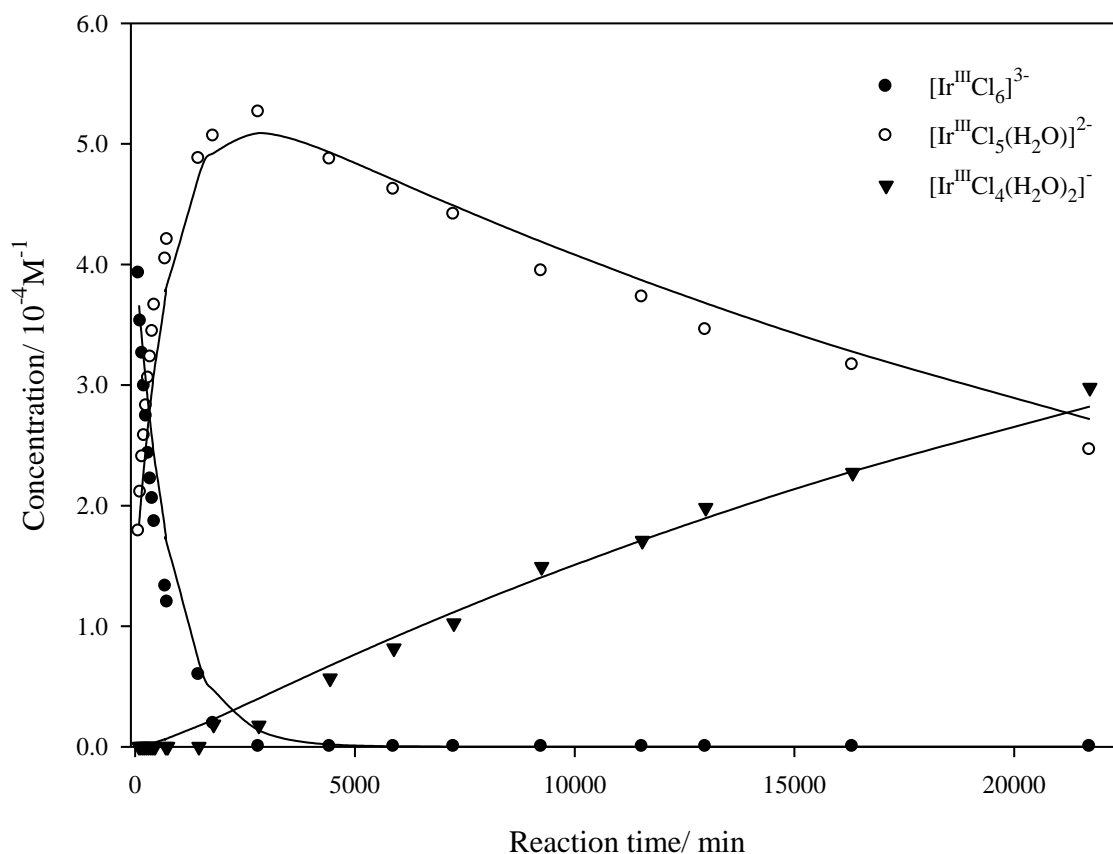


Figure 4.4: Species concentration determined as a function of time. The symbols represent the data obtained from the chromatographic traces in Figure 4.3 and the solid lines represent the non-linear least-squares fit calculated with the program Equikin.

The rate of $[\text{Ir}^{\text{III}}\text{Cl}_6]^{3-}$ aquation as a function of temperature was measured with the developed IP-HPLC system. Samples containing 8.00 ± 0.05 mM $[\text{Ir}^{\text{III}}\text{Cl}_6]^{3-}$ were prepared in a 0.10 M HCl matrix and stored at different temperatures. The samples were analysed as a function of time and the resulting chromatographic traces were integrated using the program

Peakfit. The rate constants (k_{aq1}) at different temperatures were determined by integration of the pseudo-first order aquation rate model, Equation 4.11, to yield Equation 4.15. Plots of $\ln([\text{Ir}^{\text{III}}\text{Cl}_6]^{2-} \text{ peak area})$ vs. time are shown in, Figure 4.5, and excellent linear fits to the data were obtained. The rate constants (k_{aq1}) calculated from the gradients of these linear functions at different temperatures are listed in Table 4.2.

$$\ln[\text{Ir}^{\text{III}}\text{Cl}_6]^{2-} = \ln [\text{Ir}^{\text{III}}\text{Cl}_6]_i^{2-} - k_{\text{aq1}}t \quad (4.15)$$

Table 4.2: Rate constants calculated for the aquation of $[\text{Ir}^{\text{III}}\text{Cl}_6]^{3-}$ as a function of temperature.

Temperature/ K	Concentration of $[\text{IrCl}_6]^{3-}$ / mM	Concentration of HCl/ M	k_{aq1} / sec^{-1}
295.1	8.01	0.102	3.42×10^{-5}
300.1	7.95	0.102	6.83×10^{-5}
305.1	8.00	0.102	13.49×10^{-5}
310.1	8.04	0.102	26.89×10^{-5}
315.1	7.99	0.102	46.5×10^{-5}

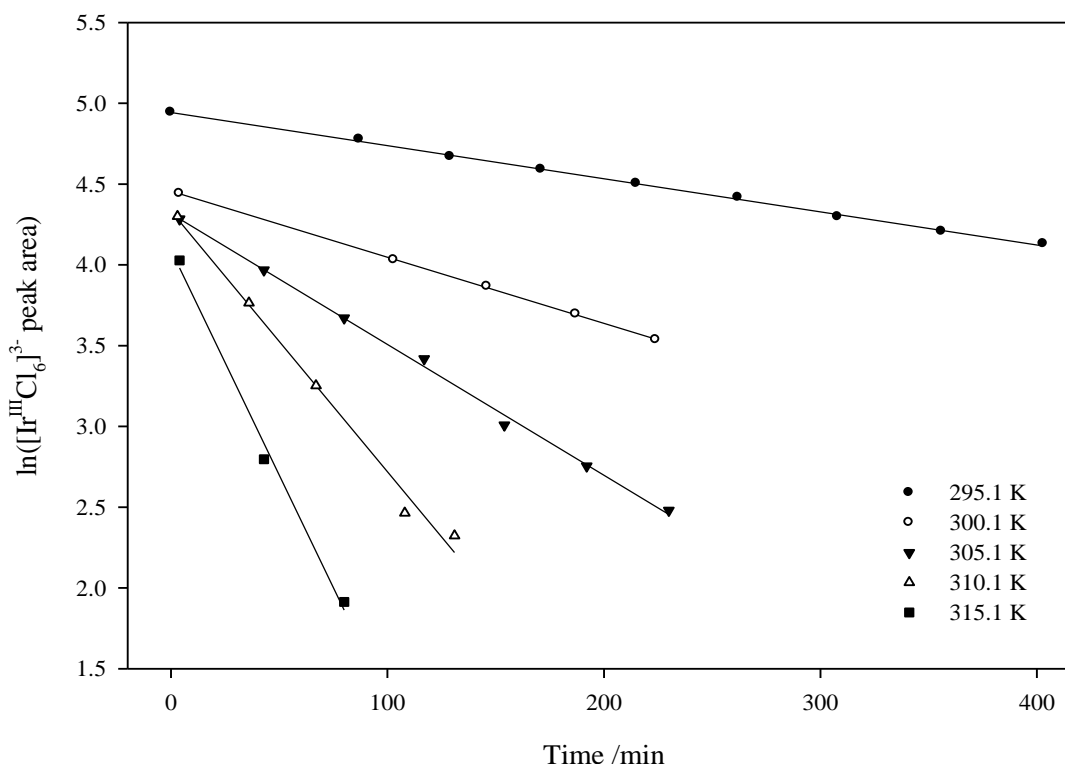


Figure 4.5: Plot of the natural logarithm of the absorbance measured for $[\text{Ir}^{\text{III}}\text{Cl}_6]^{3-}$ as a function of time, for the calculation of the rate constant, k_{aq1} .

The corresponding Eyring plot, Equation 3.27, for the rate constants (k_{aq1}) listed in Table 4.2 is shown in Figure 4.6. The straight line obtained indicates that the enthalpy of activation (ΔH^\ddagger) is not dependent on temperature in the range of 295.1 - 315.1 K. The enthalpy of activation ($\Delta H^\ddagger = 99.41 \pm 0.09 \text{ kJ.mol}^{-1}$) and entropy of activation ($\Delta S^\ddagger = 40.70 \pm 0.17 \text{ J.mol}^{-1}.\text{K}^{-1}$) were calculated from the slope and intercept respectively. The Gibbs energy of activation (ΔG^\ddagger) at 298.1 K is equal to $87.28 \pm 0.04 \text{ kJ.mol}^{-1}$ and relates to the energy required to form the activated complex.

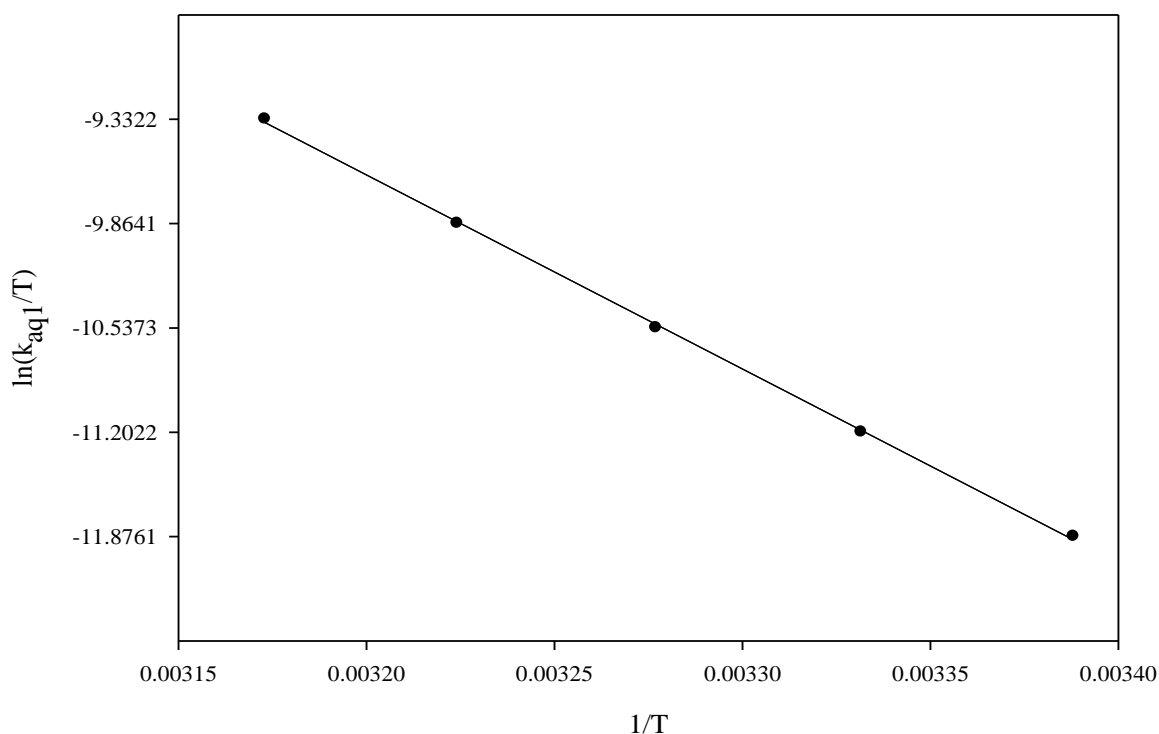


Figure 4.6: Plot of $\ln(k_{\text{aq1}}/T)$ as a function of $(1/T)$. From this plot the thermodynamic parameters (ΔH^\ddagger and ΔS^\ddagger) were calculated. T = temperature in Kelvin

In contrast to the relative large negative entropy of activation calculated for the oxidation of $[\text{Pt}^{\text{II}}\text{Cl}_4]^{2-}$ by $[\text{Ir}^{\text{IV}}\text{Cl}_6]^{2-}$, Reaction 3.12, ($\Delta S^\ddagger = -107.76 \pm 0.87 \text{ J.mol}^{-1}.\text{K}^{-1}$), the ΔS^\ddagger calculated for the aquation of $[\text{Ir}^{\text{III}}\text{Cl}_6]^{3-}$ is positive. It is reported that the aquation of $[\text{Ir}^{\text{III}}\text{Cl}_6]^{3-}$ occurs via a dissociative interchange mechanism (I_d) and the positive entropy of activation obtained here supports this mechanistic proposition.⁶⁸

4.4. IP-HPLC separation of $[Pt^{IV}Cl_6]^{2-}$, $[Pt^{II}Cl_4]^{2-}$, $[Ir^{IV}Cl_6]^{2-}$, $[Ir^{III}Cl_6]^{3-}$ and their respective aquation products

4.4.1. Reactions that must be taken into account for the investigation of the redox mechanism.

In order to predict the extent of $[Ir^{III}Cl_6]^{3-}$ aquation during the reaction between $[Ir^{IV}Cl_6]^{2-}$ and $[Pt^{II}Cl_4]^{2-}$ in HCl deficient matrices the rate constants for the various reactions must be compared to one another. If the concentration of water (55.5 M) is taken into account, the pseudo-first order rate constant for the aquation of $[Ir^{III}Cl_6]^{3-}$ ($k_{aq1} = 3.50 \times 10^{-5} \text{ sec}^{-1}$) can be described as a second order rate constant ($k_{aq1}^* = 6.31 \times 10^{-7} \text{ M}^{-1} \cdot \text{sec}^{-1}$). This rate constant can be compared to the rate constant for the reduction of $[Ir^{IV}Cl_6]^{2-}$ by $[Pt^{II}Cl_4]^{2-}$. The rate constant for the reduction of $[Ir^{IV}Cl_6]^{2-}$ by $[Pt^{II}Cl_4]^{2-}$ at 0.8 M HCl is equal to $0.713 \text{ M}^{-1} \cdot \text{sec}^{-1}$ which is 1.13×10^6 times larger than the second order aquation rate constant of $[Ir^{III}Cl_6]^{3-}$ in 0.1 M HCl. Therefore, if $[Ir^{III}Cl_6]^{3-}$ is formed during the reduction of $[Ir^{IV}Cl_6]^{2-}$ by $[Pt^{II}Cl_4]^{2-}$ it will still be visible during analysis with limited aquation taking place.

$$\frac{d[Ir^{III}Cl_6]^{3-}}{dt} = 2k_1([Ir^{IV}Cl_6]^{2-})([Pt^{II}Cl_4]^{2-}) \quad (4.16)$$

$$\frac{d[Ir^{III}Cl_6]^{3-}}{dt} = k_{aq1}^*([Ir^{III}Cl_6]^{3-})(H_2O) = k_{aq1}([Ir^{III}Cl_6]^{3-}) \quad (4.17)$$

When $[Pt^{IV}Cl_6]^{2-}$, $[Pt^{II}Cl_4]^{2-}$, $[Ir^{IV}Cl_6]^{2-}$ and $[Ir^{III}Cl_6]^{3-}$ are simultaneously present in a chloride deficient sample, several reactions can take place. The aquation of $[Ir^{IV}Cl_6]^{2-}$ is negligible in a timeframe of 7 days, whereas the rate of $[Pt^{IV}Cl_6]^{2-}$ aquation is very slow.⁵⁷⁻⁶¹ However, the presence of $[Pt^{II}Cl_4]^{2-}$ will significantly increase the rate of $[Pt^{IV}Cl_6]^{2-}$ aquation ($k \approx 10^5 \text{ sec}^{-1}$) and therefore aquation will take place before the sample can be analyzed using this HPLC-UV-Vis method. Furthermore, only a small amount (3 %) of $[Pt^{II}Cl_4]^{2-}$ will aquate in a 0.1 M HCl matrix. It was proven spectrophotometrically that the presence of $[Pt^{II}Cl_4]^{2-}$ has no effect on the aquation rate of $[Ir^{III}Cl_6]^{3-}$ and that in 0.1 M HCl the $[Ir^{III}Cl_6]^{3-}$ complex anion will aquate at a rate of $k_{aq1} = 3.50 \times 10^{-5} \text{ sec}^{-1}$. In comparison to the reduction rate of $[Ir^{IV}Cl_6]^{2-}$ the aquation rate of $[Ir^{III}Cl_6]^{3-}$ is much slower and the Ir^{III} product formed during this redox reaction will be observable. If the assumption is made that chloride transfer does not facilitate the redox reaction between $[Ir^{IV}Cl_6]^{2-}$ and $[Pt^{II}Cl_4]^{2-}$ a peak corresponding to $[Ir^{III}Cl_6]^{3-}$ will be observed in the chromatographic trace. However, if chloride transfer does

take place, the $[\text{Ir}^{\text{III}}\text{Cl}_6]^{3-}$ species will not be formed to any significant extent during this redox reaction in 0.1 M HCl and no $[\text{Ir}^{\text{III}}\text{Cl}_6]^{3-}$ peak will be observed. The presence or absence of the $[\text{Ir}^{\text{III}}\text{Cl}_6]^{3-}$ peak in the chromatographic trace will clearly indicate whether chloride transfer does or does not take place.

4.4.2. IP-HPLC separation of $[\text{Pt}^{\text{IV}}\text{Cl}_6]^{2-}$ and $[\text{Pt}^{\text{II}}\text{Cl}_4]^{2-}$

A sample containing 1.0 mM $[\text{Pt}^{\text{IV}}\text{Cl}_6]^{2-}$ was prepared in Milli-Q water and aged for a sufficient time such that aquation can take place. This sample was then injected onto the C_{18} column (IP-HPLC UV-Vis analysis) and the resulting chromatographic trace at 262 nm is shown in Figure 4.7. The optimized chromatographic conditions used were a mobile phase of 47% (v/v) acetonitrile and an aqueous solution of 15 mM TBA^+Cl^- buffered to a pH of 4 using an acetate buffer. Optimization of the IP-HPLC method used here is briefly discussed in chapter 2.2.3 and all subsequent IP-HPLC separations were carried out with this methodology.

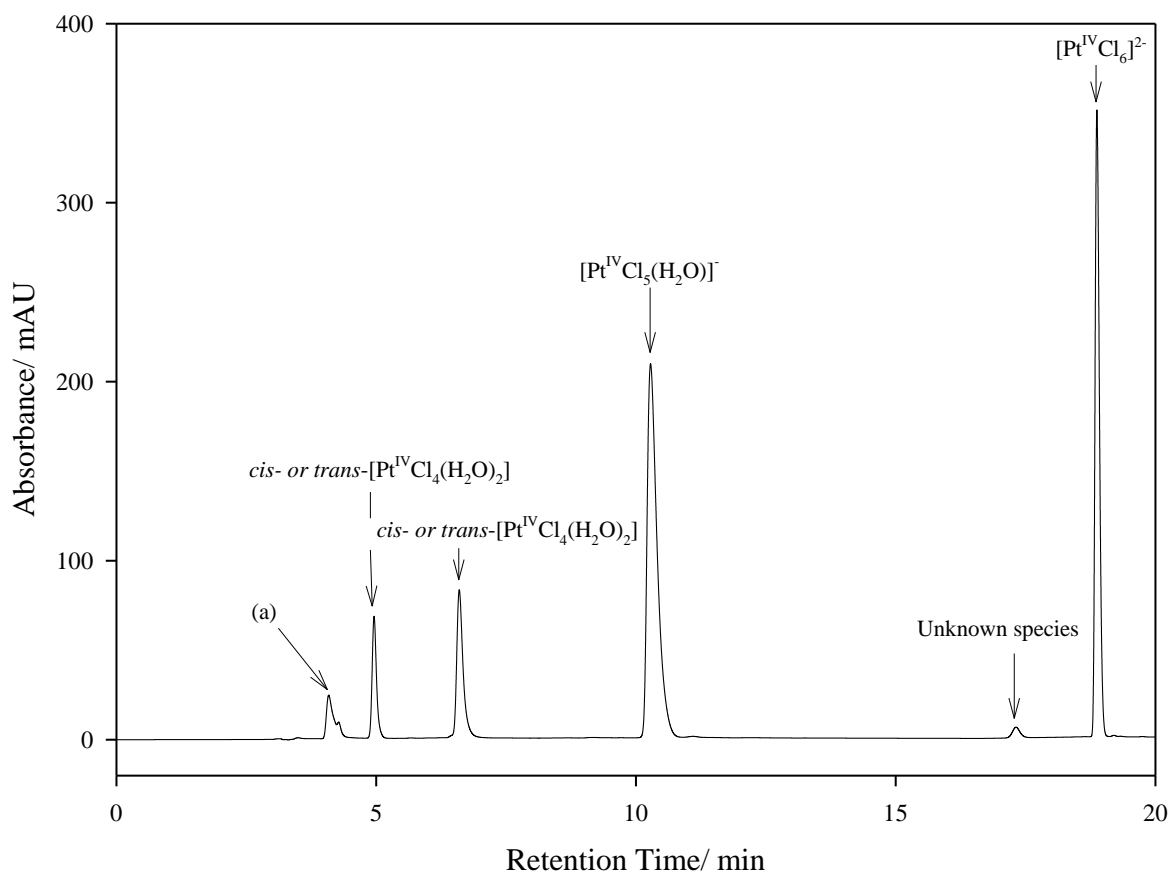


Figure 4.7: Chromatographic separation of the $[\text{Pt}^{\text{IV}}\text{Cl}_n(\text{H}_2\text{O})_{6-n}]^{4-n}$ ($n=3-6$) series of complexes detected at 262 nm, (a) *fac-* and *mer-* $[\text{Pt}^{\text{IV}}\text{Cl}_3(\text{H}_2\text{O})_3]^+$.

Assignment of the peaks observed in the chromatographic trace, Figure 4.7, is based on previous work done by Koch *et. al.*³⁰ where it is reported that the separation of the $[\text{Pt}^{\text{IV}}\text{Cl}_n(\text{H}_2\text{O})_{6-n}]^{4-n}$ ($n = 3-6$) series of complexes is dependent on the charge of the anionic species and that the retention time of the anionic complexes decrease with a decrease in charge. The retention times of the detected species are listed in Table 4.3. The neutral and cationic aquated stereoisomer pairs (*cis-* and *trans-* $[\text{Pt}^{\text{IV}}\text{Cl}_4(\text{H}_2\text{O})_2]$; *fac-* and *mer-* $[\text{Pt}^{\text{IV}}\text{Cl}_3(\text{H}_2\text{O})_3]^+$) were also separated. Koch *et. al.* postulated that partial hydrolysis occurs to form the respective anionic hydroxido species, which can ion-pair with TBA^+ and be retained in the column.³⁰ Moreover, the hydroxido and aqua analogous of the stereoisomers *cis-* and *trans-* $[\text{Pt}^{\text{IV}}\text{Cl}_4(\text{H}_2\text{O})_2]$ and the stereoisomers *fac-* and *mer-* $[\text{Pt}^{\text{IV}}\text{Cl}_3(\text{H}_2\text{O})_3]^+$ are in rapid exchange and therefore elute as single peaks.

Table 4.3: Peak assignment for the chromatographic separation of $[\text{Pt}^{\text{IV}}\text{Cl}_n(\text{H}_2\text{O})_{6-n}]^{4-n}$ ($n = 3-6$) in Figure 4.7.

Retention time/ min	Peak assignment
4.07	<i>fac-</i> or <i>mer-</i> $[\text{Pt}^{\text{IV}}\text{Cl}_3(\text{H}_2\text{O})_3]^+$
4.28	<i>fac-</i> or <i>mer-</i> $[\text{Pt}^{\text{IV}}\text{Cl}_3(\text{H}_2\text{O})_3]^+$
4.90	<i>cis-</i> or <i>trans-</i> $[\text{Pt}^{\text{IV}}\text{Cl}_4(\text{H}_2\text{O})_2]$
6.60	<i>cis-</i> or <i>trans-</i> $[\text{Pt}^{\text{IV}}\text{Cl}_4(\text{H}_2\text{O})_2]$
10.30	$[\text{Pt}^{\text{IV}}\text{Cl}_5(\text{H}_2\text{O})]^-$
17.33	unknown species
18.85	$[\text{Pt}^{\text{IV}}\text{Cl}_6]^{2-}$

A sample containing 1.0 mM $[\text{Pt}^{\text{II}}\text{Cl}_4]^{2-}$ was prepared in Milli-Q water and aged for a sufficient time such that aquation can take place. A small amount of $[\text{Pt}^{\text{IV}}\text{Cl}_6]^{2-}$ was added to the sample just before analysis, to compare the retention behavior of $[\text{Pt}^{\text{IV}}\text{Cl}_6]^{2-}$ in the presence of $[\text{Pt}^{\text{II}}\text{Cl}_4]^{2-}$. The sample was then injected onto the C_{18} column for IP-HPLC UV-Vis analysis and the resulting chromatographic trace at 250 nm is shown in Figure 4.8.

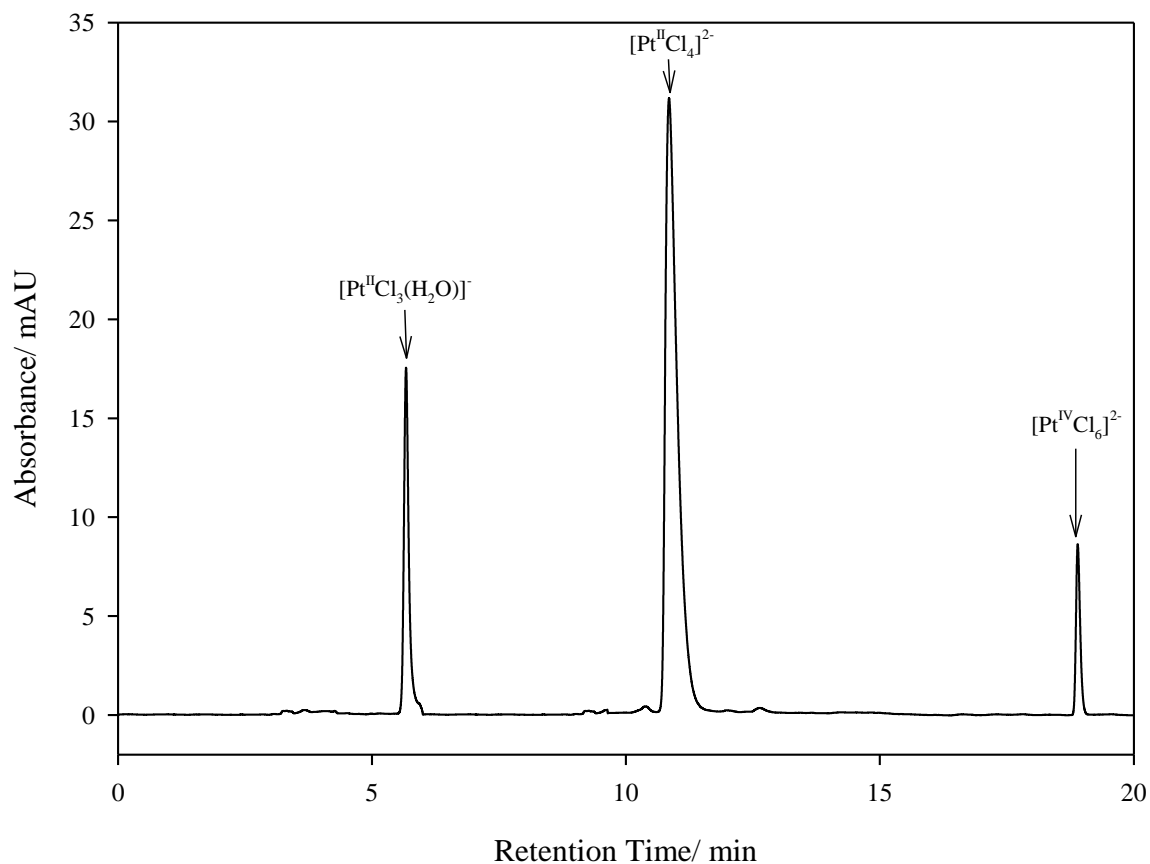


Figure 4.8: Chromatographic separation of the $[\text{Pt}^{\text{II}}\text{Cl}_n(\text{H}_2\text{O})_{4-n}]^{2-n}$ ($n=3-4$) series of complex anions detected at 250 nm

Assignment of the peaks observed in the chromatographic trace, Figure 4.8, is based on previous work done by Koch *et. al.*³⁰ and the retention times of all species are listed in Table 4.4. The peak eluting at 18.82 minutes is assigned to the $[\text{Pt}^{\text{IV}}\text{Cl}_6]^{2-}$ species, based on the UV-Vis spectrum of this peak obtained using the PDA as detector.

Table 4.4: Peak assignment for the chromatographic separation of $[\text{Pt}^{\text{II}}\text{Cl}_n(\text{H}_2\text{O})_{4-n}]^{2-n}$ ($n = 3-4$) in Figure 4.8

Retention time/ min	Peak assignment
5.65	$[\text{Pt}^{\text{II}}\text{Cl}_3(\text{H}_2\text{O})]^-$
10.84	$[\text{Pt}^{\text{II}}\text{Cl}_4]^{2-}$
18.82	$[\text{Pt}^{\text{IV}}\text{Cl}_6]^{2-}$

4.4.3. IP-HPLC separation of $[\text{Ir}^{\text{IV}}\text{Cl}_6]^{2-}$ and $[\text{Ir}^{\text{III}}\text{Cl}_6]^{3-}$

A sample containing 1.0 mM $[\text{Ir}^{\text{IV}}\text{Cl}_6]^{2-}$ was prepared in Milli-Q water. However, upon injection precipitation of the $[\text{Ir}^{\text{IV}}\text{Cl}_6]^{2-}$ species on the guard column occurs. If the concentration of $[\text{Ir}^{\text{IV}}\text{Cl}_6]^{2-}$ is below the K_{sp} , Equation 4.18, precipitation will not take place and this results in a relatively low intensity peak for $[\text{Ir}^{\text{IV}}\text{Cl}_6]^{2-}$ at a retention time of 19.08 minutes.

$$K_{\text{sp}} = (\text{TBA}^+)^2 ([\text{Ir}^{\text{IV}}\text{Cl}_6]^{2-}) \quad (4.18)$$

A sample containing 1.0 mM $[\text{Ir}^{\text{III}}\text{Cl}_6]^{3-}$ in Milli-Q water was prepared and injected onto the C_{18} column directly after preparation with the resulting chromatographic trace at 254 nm shown in Figure 4.9.

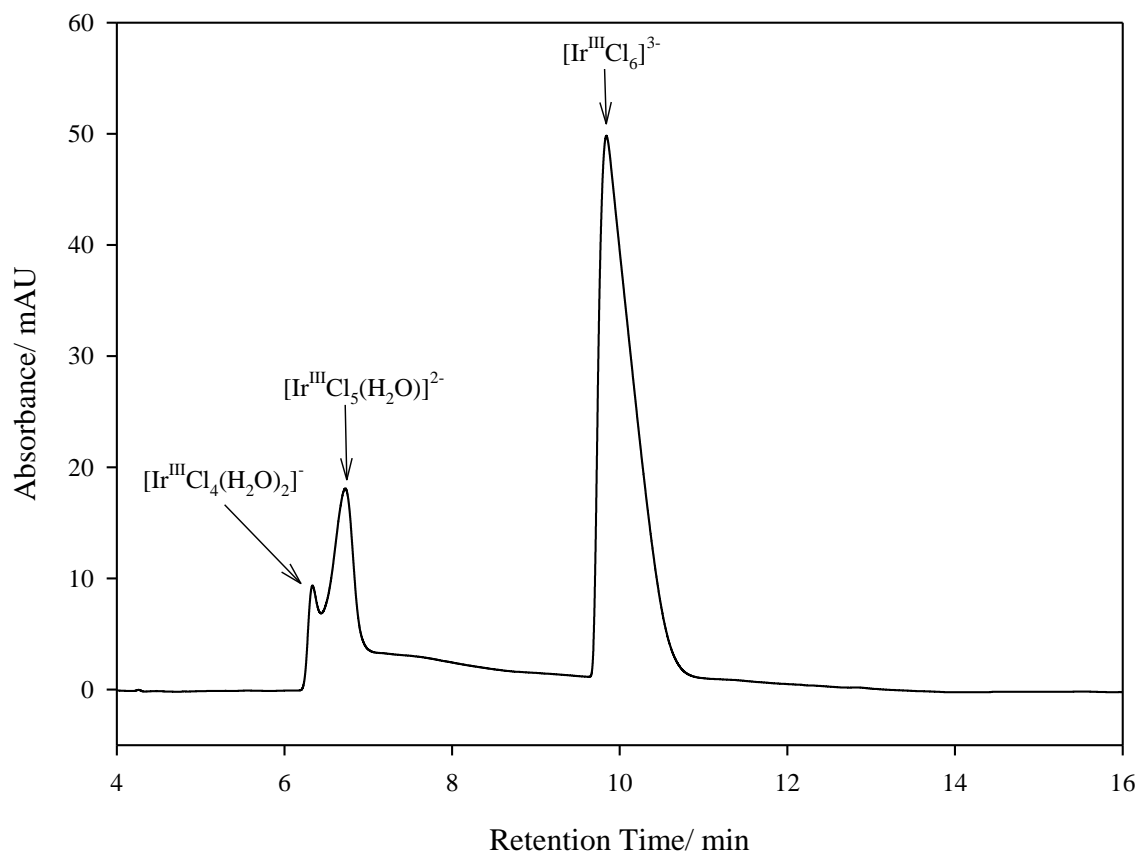


Figure 4.9: Chromatographic separation of the $[\text{Ir}^{\text{III}}\text{Cl}_n(\text{H}_2\text{O})_{6-n}]^{3-n}$ ($n = 4-6$) species detected at 254 nm

A similar chromatographic separation for Figure 4.9 is obtained as compared to Figure 4.2 and assignment of the chromatographic trace is based on the assignment given in Figure 4.2. The retention times of the eluting species are listed in Table 4.5. After elution of the $[\text{Ir}^{\text{III}}\text{Cl}_5(\text{H}_2\text{O})]^{2-}$ species, the absorbance does not return to the baseline and can be ascribed to the aquation of $[\text{Ir}^{\text{III}}\text{Cl}_6]^{3-}$ during the chromatographic run. The presence of $[\text{Ir}^{\text{III}}\text{Cl}_4(\text{H}_2\text{O})_2]^-$ indicate that the salt used for this chromatographic separation contains traces of this species since the time required for $[\text{Ir}^{\text{III}}\text{Cl}_5(\text{H}_2\text{O})]^{2-}$ to substantially aquate and form $[\text{Ir}^{\text{III}}\text{Cl}_4(\text{H}_2\text{O})_2]^-$ at the observed quantities is much longer than the time taken to prepare and inject the sample, Figure 4.9.

Table 4.5: Peak assignment for the chromatographic separation of $[\text{IrCl}_n(\text{H}_2\text{O})_{6-n}]^{3-n}$ ($n = 4-6$) in Figure 4.9.

Retention time/ min	Peak assignment
6.34	$[\text{Ir}^{\text{III}}\text{Cl}_4(\text{H}_2\text{O})_2]^-$
6.71	$[\text{Ir}^{\text{III}}\text{Cl}_5(\text{H}_2\text{O})]^{2-}$
9.89	$[\text{Ir}^{\text{III}}\text{Cl}_6]^{3-}$

4.4.4. IP-HPLC separation of a sample containing a mixture of $[\text{Pt}^{\text{II}}\text{Cl}_4]^{2-}$, $[\text{Pt}^{\text{IV}}\text{Cl}_6]^{2-}$, $[\text{Ir}^{\text{III}}\text{Cl}_6]^{3-}$ and their respective aquation products

A sample containing 1 mM $[\text{Ir}^{\text{III}}\text{Cl}_6]^{3-}$, 1 mM $[\text{Pt}^{\text{II}}\text{Cl}_4]^{2-}$ and 1mM $[\text{Pt}^{\text{IV}}\text{Cl}_6]^{2-}$ was prepared in MilliQ water to investigate whether sufficient separation of $[\text{Ir}^{\text{III}}\text{Cl}_6]^{3-}$, $[\text{Pt}^{\text{II}}\text{Cl}_4]^{2-}$ and $[\text{Pt}^{\text{IV}}\text{Cl}_5(\text{H}_2\text{O})]^{2-}$, eluting in the region of 10 minutes, is achieved. The sample was injected onto the column and the resulting chromatographic trace is shown in Figure 4.10.

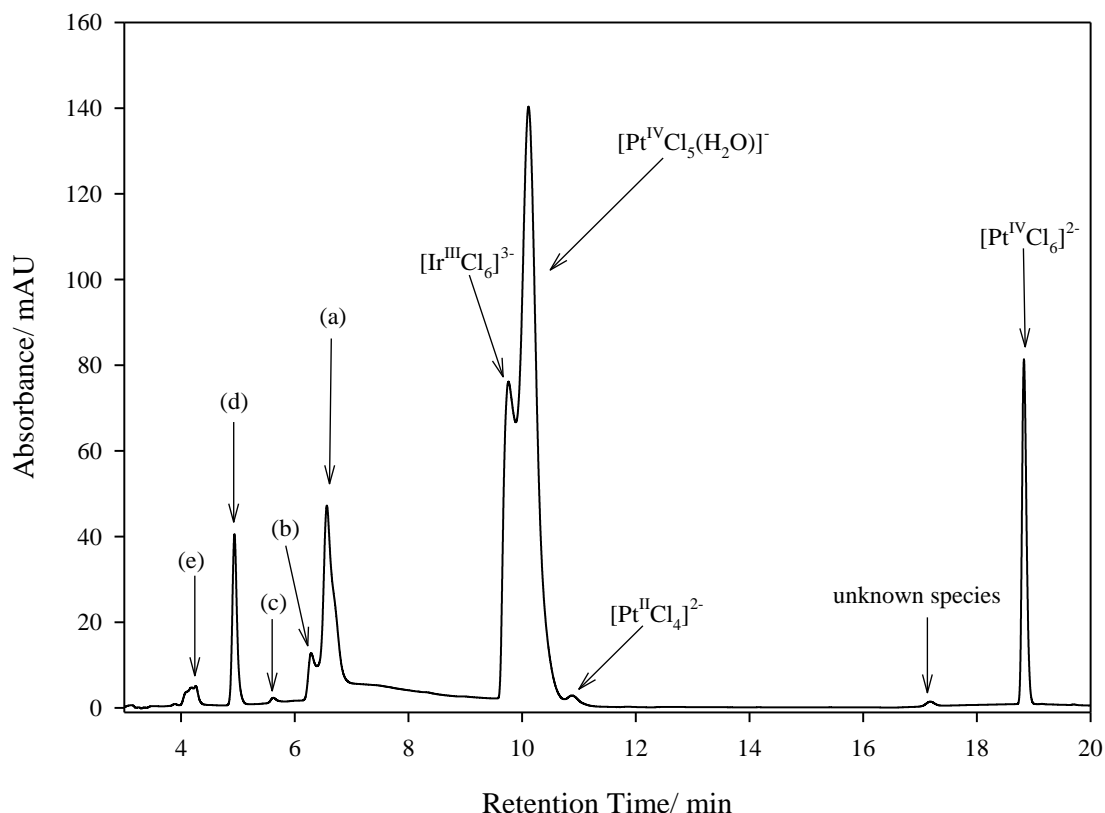


Figure 4.10: Chromatographic trace of the simultaneous separation of $[\text{Ir}^{\text{III}}\text{Cl}_6]^{3-}$, $[\text{Pt}^{\text{II}}\text{Cl}_4]^{2-}$, $[\text{Pt}^{\text{IV}}\text{Cl}_6]^{2-}$ and their respective aquation products detected at 250 nm. (a) the $[\text{Ir}^{\text{III}}\text{Cl}_5(\text{H}_2\text{O})]^{2-}$ and *cis* or *trans*- $[\text{Pt}^{\text{IV}}\text{Cl}_4(\text{H}_2\text{O})_2]$ species co-eluting, (b) $[\text{Ir}^{\text{III}}\text{Cl}_4(\text{H}_2\text{O})_2]^-$, (c) unknown species, (d) *cis* or *trans*- $[\text{Pt}^{\text{IV}}\text{Cl}_4(\text{H}_2\text{O})_2]$, (e) *fac* and *mer*- $[\text{Pt}^{\text{IV}}\text{Cl}_3(\text{H}_2\text{O})_3]^+$.

The chromatographic trace, Figure 4.10, shows three peaks elute in the retention time region of 10 minutes. The three peaks are assigned to the $[\text{Ir}^{\text{III}}\text{Cl}_6]^{3-}$, $[\text{Pt}^{\text{IV}}\text{Cl}_5(\text{H}_2\text{O})]^-$ and $[\text{Pt}^{\text{II}}\text{Cl}_4]^{2-}$ species, based on the retention times obtained from Figures 4.7 - 4.9. The $[\text{Ir}^{\text{III}}\text{Cl}_6]^{3-}$ species elutes as a shoulder of the $[\text{Pt}^{\text{IV}}\text{Cl}_5(\text{H}_2\text{O})]^-$ species. However, these species are distinguishable from one another.

4.5. IP-HPLC analysis of the formation of Pt^{IV} and Ir^{III} products in 0.1 M HCl

A sample containing 10 mM $[\text{Pt}^{\text{II}}\text{Cl}_4]^{2-}$ and 10 mM $[\text{Ir}^{\text{IV}}\text{Cl}_6]^{2-}$ was prepared by adding equal parts of 20 mM $[\text{Ir}^{\text{IV}}\text{Cl}_6]^{2-}$ and 20 mM $[\text{Pt}^{\text{II}}\text{Cl}_4]^{2-}$ stock solutions in 0.10 M HCl. After a reaction time of 5 minutes the sample was diluted 10 fold and injected onto the C_{18} column, Figure 4.11.

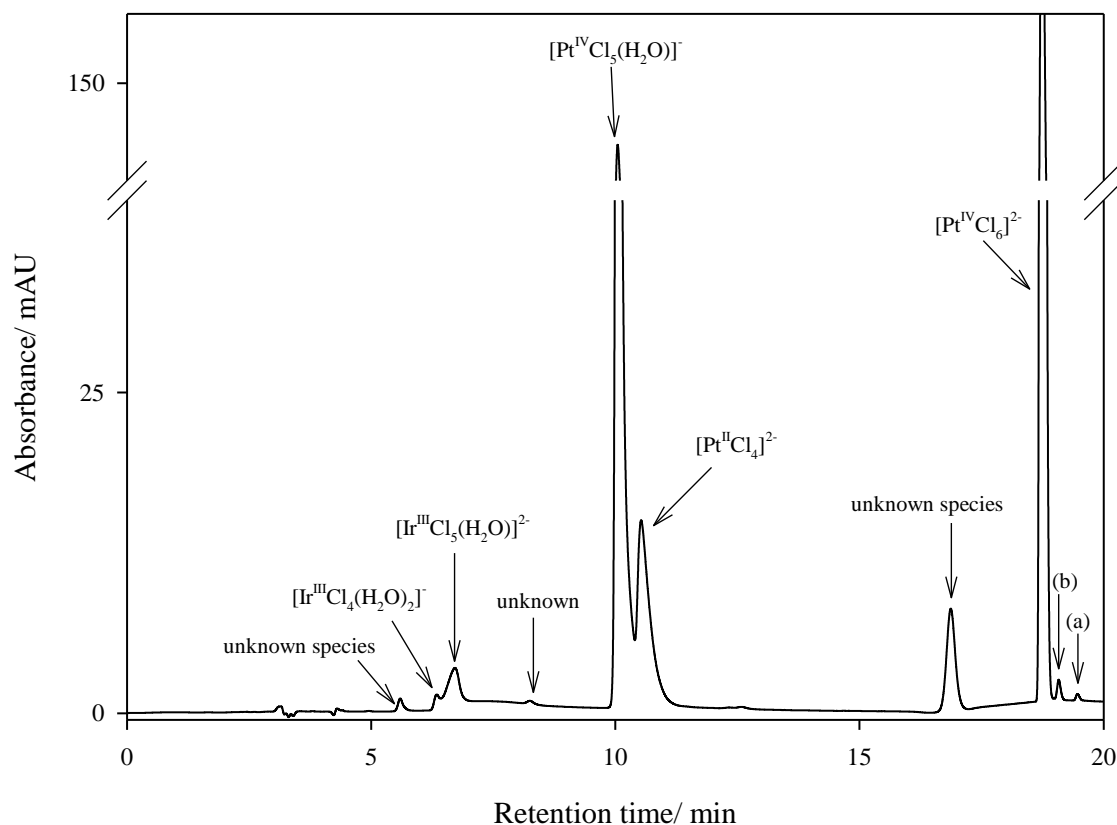


Figure 4.11: Investigation of the Ir^{III} and Pt^{IV} reaction products in 0.10 M chloride after a reaction time of 5 min, for the rationalization of the reaction mechanism for the redox reaction between $[\text{Ir}^{\text{IV}}\text{Cl}_6]^{2-}$ and $[\text{Pt}^{\text{II}}\text{Cl}_4]^{2-}$, (a) unknown species, (b) small amounts of $[\text{Ir}^{\text{IV}}\text{Cl}_6]^{2-}$ observed.

In Figure 4.11 it can be observed that relatively large amounts of $[\text{Pt}^{\text{IV}}\text{Cl}_6]^{2-}$ and $[\text{Pt}^{\text{IV}}\text{Cl}_5(\text{H}_2\text{O})]^{-}$ species have formed after a reaction time of 5 minutes and only small amounts of the higher aquated Pt^{IV} species are present. This corresponds well with the expected $[\text{Pt}^{\text{IV}}\text{Cl}_n(\text{H}_2\text{O})_{6-n}]^{4-n}$ ($n = 3-6$) species distribution in a 0.1 M HCl matrix. A relatively large peak for the unreacted $[\text{Pt}^{\text{II}}\text{Cl}_4]^{2-}$ species is present, with only a small peak observed for the $[\text{Ir}^{\text{IV}}\text{Cl}_6]^{2-}$ species. Peaks corresponding to the $[\text{Ir}^{\text{III}}\text{Cl}_5(\text{H}_2\text{O})_2]^{2-}$ and $[\text{Ir}^{\text{III}}\text{Cl}_4(\text{H}_2\text{O})_2]^{-}$ species can clearly be seen and the $[\text{Ir}^{\text{III}}\text{Cl}_6]^{3-}$ species is not observed in the chromatographic trace. The PDA spectrum of the $[\text{Pt}^{\text{IV}}\text{Cl}_5(\text{H}_2\text{O})]^{-}$ peak was studied to verify that $[\text{Ir}^{\text{III}}\text{Cl}_6]^{3-}$ and $[\text{Pt}^{\text{IV}}\text{Cl}_5(\text{H}_2\text{O})]^{-}$ does not co-elute. Furthermore, the peaks corresponding to $[\text{Pt}^{\text{IV}}\text{Cl}_5(\text{H}_2\text{O})]^{-}$ and $[\text{Pt}^{\text{II}}\text{Cl}_4]^{2-}$ are not well resolved and traces of $[\text{Pt}^{\text{II}}\text{Cl}_4]^{2-}$ is expected to co-elute with the $[\text{Pt}^{\text{IV}}\text{Cl}_5(\text{H}_2\text{O})]^{-}$ species. The PDA spectra of $[\text{Pt}^{\text{IV}}\text{Cl}_5(\text{H}_2\text{O})]^{-}$ obtained from Figure 4.7 and $[\text{Pt}^{\text{II}}\text{Cl}_4]^{2-}$ from Figure 4.8 are shown in Figure 4.12.

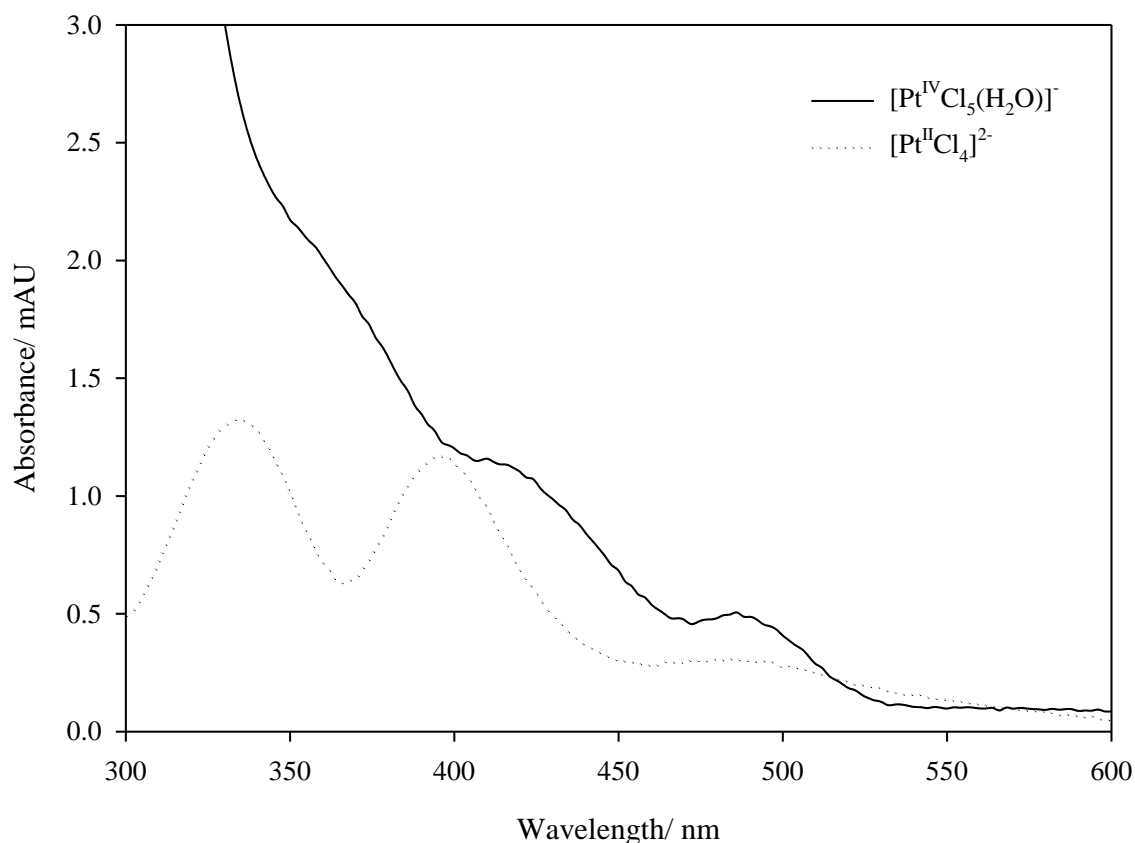


Figure 4.12: PDA spectra of $[\text{Pt}^{\text{IV}}\text{Cl}_5(\text{H}_2\text{O})]^-$ obtained from Figure 4.7 and $[\text{Pt}^{\text{II}}\text{Cl}_4]^{2-}$ obtained from Figure 4.8.

The PDA spectrum of $[\text{Pt}^{\text{IV}}\text{Cl}_5(\text{H}_2\text{O})]^-$ along with the simulation of a mixture of $[\text{Pt}^{\text{II}}\text{Cl}_4]^{2-}$ and $[\text{Pt}^{\text{IV}}\text{Cl}_5(\text{H}_2\text{O})]^-$ obtained by combining the PDA spectra of these species given in Figure 4.12 ($0.975 \times [\text{Pt}^{\text{IV}}\text{Cl}_5(\text{H}_2\text{O})]^- + 0.025 \times [\text{Pt}^{\text{II}}\text{Cl}_4]^{2-}$) is shown in Figure 4.13. The simulation fit of ($0.975 \times [\text{Pt}^{\text{IV}}\text{Cl}_5(\text{H}_2\text{O})]^- + 0.025 \times [\text{Pt}^{\text{II}}\text{Cl}_4]^{2-}$) to the spectrum of $[\text{Pt}^{\text{IV}}\text{Cl}_5(\text{H}_2\text{O})]^-$ in the reaction mixture, Figure 4.11, is excellent and indicates that no $[\text{Ir}^{\text{III}}\text{Cl}_6]^{3-}$ co-elutes with the $[\text{Pt}^{\text{IV}}\text{Cl}_5(\text{H}_2\text{O})]^-$ species. Therefore, it is clear that no $[\text{Ir}^{\text{III}}\text{Cl}_6]^{3-}$ forms during the reduction of $[\text{Ir}^{\text{IV}}\text{Cl}_6]^{2-}$ with $[\text{Pt}^{\text{II}}\text{Cl}_4]^{2-}$ in chloride deficient media and that the absence of $[\text{Ir}^{\text{III}}\text{Cl}_6]^{3-}$ supports the notion that chloride transfer occurs during this redox reaction. Moreover, the lack of any $[\text{Ir}^{\text{III}}\text{Cl}_6]^{3-}$ signifies that the second redox reaction, Reaction 3.13, occurs via a similar mechanism and also produces the $[\text{Ir}^{\text{III}}\text{Cl}_5(\text{H}_2\text{O})]^{2-}$ product. A reaction mechanism that takes chloride transfer into account is illustrated in Scheme 4.1.

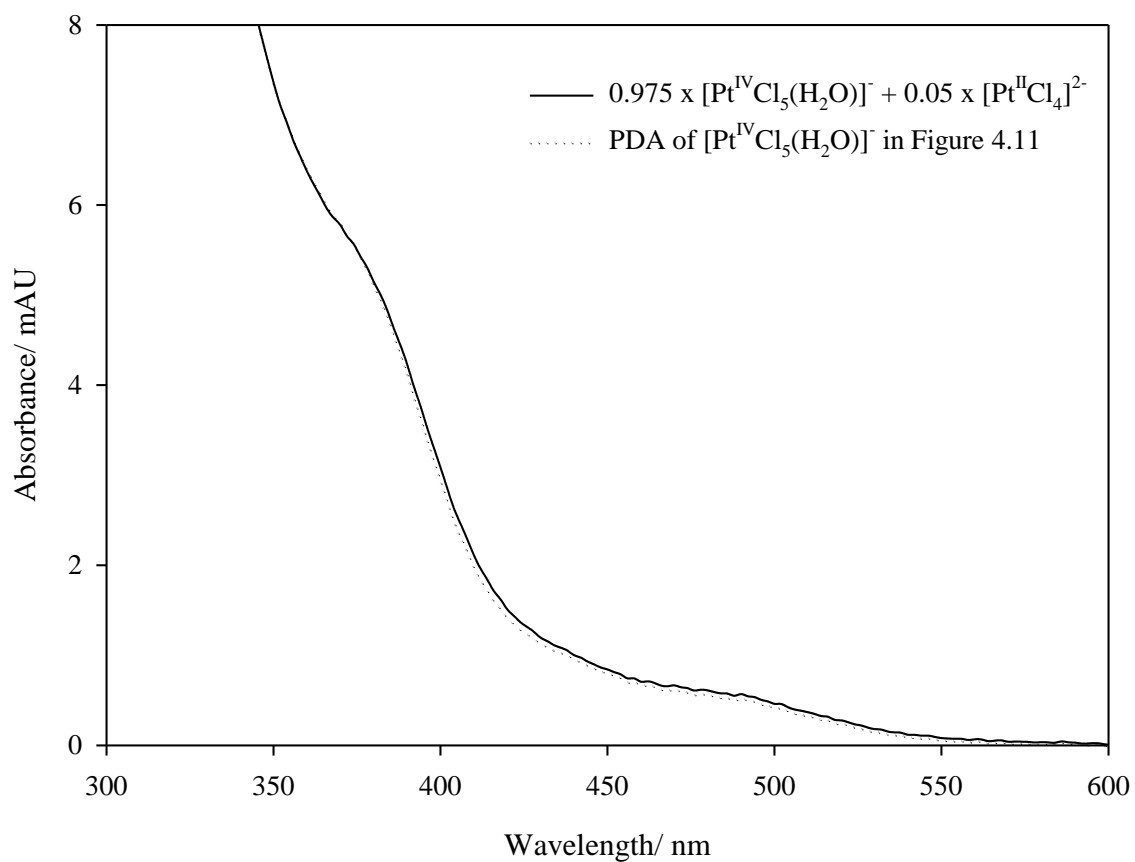
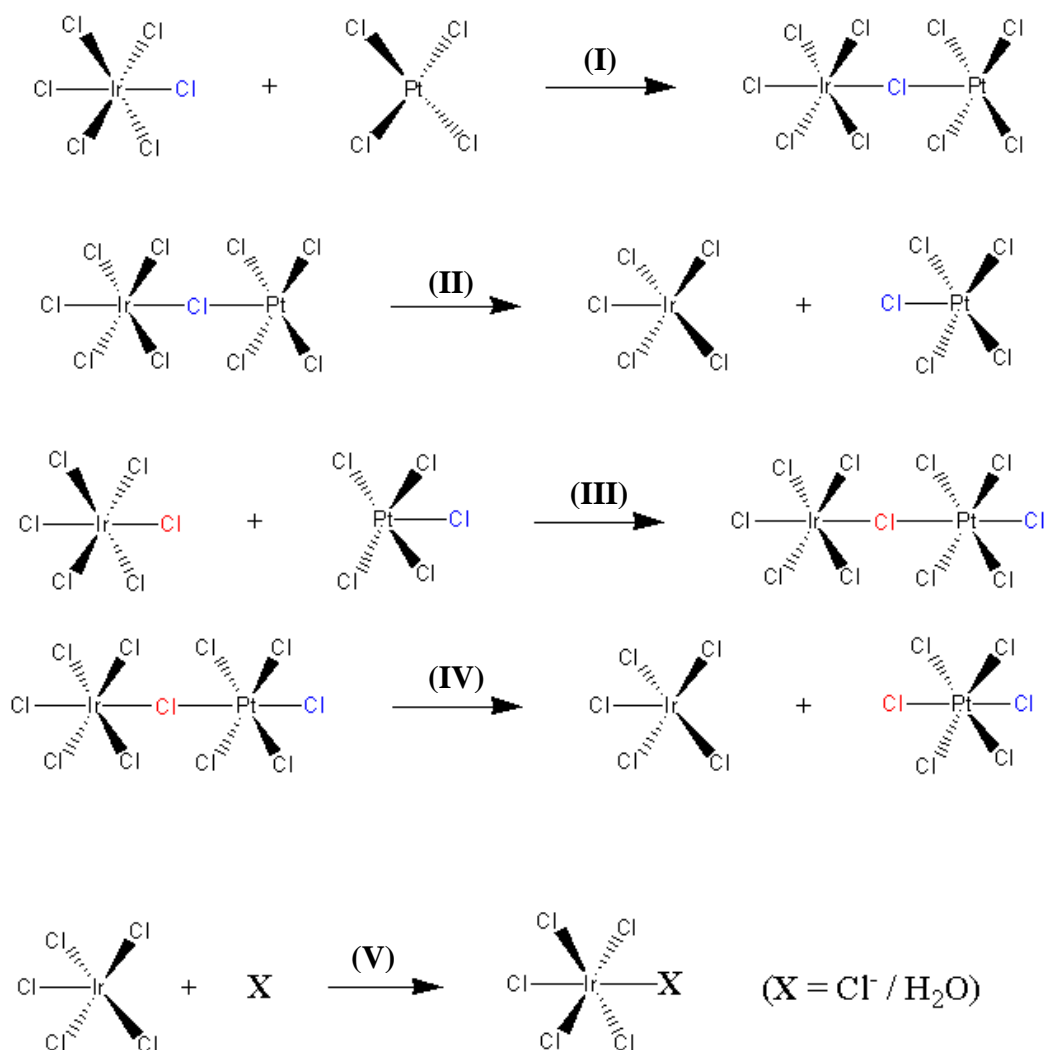


Figure 4.13: The PDA spectrum of $[\text{Pt}^{\text{IV}}\text{Cl}_5(\text{H}_2\text{O})]^-$ in Figure 4.11 with the simulation of $0.05 \times [\text{Pt}^{\text{II}}\text{Cl}_4]^{2-} + 0.975 \times [\text{Pt}^{\text{IV}}\text{Cl}_5(\text{H}_2\text{O})]^-$ from the PDA spectra given in Figure 4.12.



Scheme 4.1: Proposed reaction mechanism for the redox reaction between $[\text{Ir}^{\text{IV}}\text{Cl}_6]^{2-}$ and $[\text{Pt}^{\text{II}}\text{Cl}_4]^{2-}$. The relative nature of X will result in a mixture of $[\text{Ir}^{\text{III}}\text{Cl}_6]^{3-}$ and $[\text{Ir}^{\text{III}}\text{Cl}_5(\text{H}_2\text{O})]^{2-}$ depending on the free chloride concentration of the sample matrix.

Step (I) in the proposed reaction mechanism, Scheme 4.1, shows the formation of a chloride bridged activated complex. In step (II), the activated complex subsequently dissociates with the transfer of the bridged chloride from Ir^{IV} to Pt^{II} and an electron from Pt^{II} to Ir^{IV} resulting in the formation of $[\text{Pt}^{\text{III}}\text{Cl}_5]^{2-}$ and $[\text{Ir}^{\text{III}}\text{Cl}_5]^{2-}$. Step (III) describes the second redox reaction where another $[\text{Ir}^{\text{IV}}\text{Cl}_6]^{2-}$ complex anion reacts with the $[\text{Pt}^{\text{III}}\text{Cl}_5]^{2-}$ species to form a chloride bridged activated complex. Step (IV) describes the dissociation of the activated complex in a similar manner as step (II) to form $[\text{Ir}^{\text{III}}\text{Cl}_5]^{2-}$ and $[\text{Pt}^{\text{IV}}\text{Cl}_6]^{2-}$ as products. Step (V): The coordinative unsaturated $[\text{Ir}^{\text{III}}\text{Cl}_5]^{2-}$ complex will then react with the matrix, which is chloride deficient and form the $[\text{Ir}^{\text{III}}\text{Cl}_5(\text{H}_2\text{O})]^{2-}$ species. The nature of the Ir^{III} product will depend on the chloride concentration of the sample matrix. Note, due to the presence of $[\text{Pt}^{\text{II}}\text{Cl}_4]^{2-}$, the $[\text{Pt}^{\text{IV}}\text{Cl}_6]^{2-}$ species will rapidly aquate.

4.6. Concluding remarks

To successfully account for the formation of the products formed during the redox reaction of $[\text{Ir}^{\text{IV}}\text{Cl}_6]^{2-}$ and $[\text{Pt}^{\text{II}}\text{Cl}_4]^{2-}$ a detailed study of the aquation rates of $[\text{Pt}^{\text{IV}}\text{Cl}_6]^{2-}$, $[\text{Pt}^{\text{II}}\text{Cl}_4]^{2-}$, $[\text{Ir}^{\text{IV}}\text{Cl}_6]^{2-}$ and $[\text{Ir}^{\text{III}}\text{Cl}_6]^{3-}$ was done. The aquation rates of $[\text{Ir}^{\text{IV}}\text{Cl}_6]^{2-}$ and $[\text{Pt}^{\text{IV}}\text{Cl}_6]^{2-}$ in chloride deficient matrices are relatively slow, *i.e.* the aquation of these species are negligible within a timeframe of 5 hours. However, the $[\text{Pt}^{\text{IV}}\text{Cl}_6]^{2-}$ complex anion will rapidly aquate in the presence of $[\text{Pt}^{\text{II}}\text{Cl}_4]^{2-}$ ($k \approx 10^5$) to reach equilibrium before HPLC-UV-Vis analysis can be carried out. This significantly influences the ability to determine the nature of the Pt^{IV} product species formed during the reaction of $[\text{Ir}^{\text{IV}}\text{Cl}_6]^{2-}$ and $[\text{Pt}^{\text{II}}\text{Cl}_4]^{2-}$. The aquation kinetics of $[\text{Ir}^{\text{III}}\text{Cl}_6]^{3-}$ and $[\text{Ir}^{\text{III}}\text{Cl}_5(\text{H}_2\text{O})]^{2-}$ in 0.10 M HCl were investigated by separating the $[\text{Ir}^{\text{III}}\text{Cl}_n(\text{H}_2\text{O})_{n-6}]^{3-n}$ ($n = 3-6$) series of complex anions with the developed IP-HPLC in this study, Figure 4.3. The non-linear least-squares fits obtained for the pseudo-first order rate model, Equations 4.11 - 4.13, gave excellent fits to the experimental data, Figure 4.4. The rate constants calculated, ($k_{\text{aq1}} = 3.50 (\pm 0.12) \times 10^{-5} \text{ sec}^{-1}$ and $k_{\text{aq2}} = 1.14 (\pm 0.10) \times 10^{-6} \text{ sec}^{-1}$) compare well with the rate constants reported in literature, Table 4.1.^{38,65,67} Furthermore, the aquation of $[\text{Ir}^{\text{III}}\text{Cl}_6]^{3-}$ was studied as a function of temperature and the ΔH^\ddagger and ΔS^\ddagger for this reaction were determined ($\Delta H^\ddagger = 99.41 \pm 0.09 \text{ kJ.mol}^{-1}$ and $\Delta S^\ddagger = 40.70 \pm 0.17 \text{ J.mol}^{-1}.\text{K}^{-1}$) with the Eyring equation, Equations 3.26 and 3.27. A dissociative interchange (I_d) mechanism is proposed for the aquation of $[\text{Ir}^{\text{III}}\text{Cl}_6]^{3-}$, with the dissociation of an Ir-Cl bond to yield a 5-coordinate $[\text{Ir}^{\text{III}}\text{Cl}_5]^{2-}$ activated complex.⁶² This statement is supported by the positive ΔS^\ddagger experimentally determined for this reaction.

An IP-HPLC system was developed for the separation of the $[\text{Pt}^{\text{II}}\text{Cl}_4]^{2-}$, $[\text{Pt}^{\text{IV}}\text{Cl}_6]^{2-}$ and $[\text{Ir}^{\text{III}}\text{Cl}_6]^{3-}$ complex anions and their respective aquation products, Figures 4.7 - 4.9. The elution order and PDA spectra of the peaks obtained in the chromatographic traces were used to assign the peaks. Precipitation of $[\text{Ir}^{\text{IV}}\text{Cl}_6]^{2-}$ occurs on the guard column and only a small peak for this species can be observed at 19.08 minutes.

A reaction mixture of $[\text{Ir}^{\text{IV}}\text{Cl}_6]^{2-}$ and $[\text{Pt}^{\text{II}}\text{Cl}_4]^{2-}$ in 0.10 M chloride matrix was analysed with IP-HPLC, Figure 4.11. Substantial amounts of $[\text{Pt}^{\text{IV}}\text{Cl}_6]^{2-}$ and $[\text{Pt}^{\text{IV}}\text{Cl}_5(\text{H}_2\text{O})]^-$ species formed and unreacted $[\text{Pt}^{\text{II}}\text{Cl}_4]^{2-}$ can also be observed. Furthermore, peaks corresponding to $[\text{Ir}^{\text{III}}\text{Cl}_5(\text{H}_2\text{O})]^{2-}$ and $[\text{Ir}^{\text{III}}\text{Cl}_4(\text{H}_2\text{O})_2]^-$ are present with no peak for the $[\text{Ir}^{\text{III}}\text{Cl}_6]^{3-}$ species

present. The absence of a $[\text{Ir}^{\text{III}}\text{Cl}_6]^{3-}$ peak signifies that the first redox reaction step, Reaction 3.12, occurs via a chloride and electron transfer inner sphere mechanism. Similarly the second redox reaction, Reaction 3.13, is proposed to also occur via an inner sphere mechanism, due to the absence of $[\text{Ir}^{\text{III}}\text{Cl}_6]^{3-}$. Based on these chromatographic results a proposed reaction mechanism was constructed for the redox reaction between $[\text{Ir}^{\text{IV}}\text{Cl}_6]^{2-}$ and $[\text{Pt}^{\text{II}}\text{Cl}_4]^{2-}$, Scheme 4.1.

Chapter 5

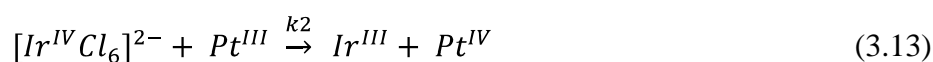
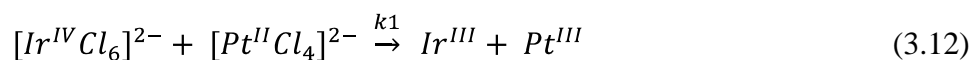
Conclusions

5

Conclusions

5.1. General conclusion

With respect to the objectives listed in Chapter 1.4, it was established that the rate of the $[\text{Ir}^{\text{IV}}\text{Cl}_6]^{2-}$ and $[\text{Pt}^{\text{IV}}\text{Cl}_6]^{2-}$ species formation during ClO_3^- oxidation of a mixed $[\text{Pt}^{\text{II}}\text{Cl}_4]^{2-}$ and $[\text{Ir}^{\text{III}}\text{Cl}_6]^{3-}$ solution is considerably influenced by the redox reaction between $[\text{Ir}^{\text{IV}}\text{Cl}_6]^{2-}$ and $[\text{Pt}^{\text{II}}\text{Cl}_4]^{2-}$, Figures 3.22 and 3.23. The reaction between $[\text{Pt}^{\text{II}}\text{Cl}_4]^{2-}$ and $[\text{Ir}^{\text{IV}}\text{Cl}_6]^{2-}$ causes an induction period in the formation of $[\text{Ir}^{\text{IV}}\text{Cl}_6]^{2-}$ and only after quantitative oxidation of $[\text{Pt}^{\text{II}}\text{Cl}_4]^{2-}$ to $[\text{Pt}^{\text{IV}}\text{Cl}_6]^{2-}$ does $[\text{Ir}^{\text{IV}}\text{Cl}_6]^{2-}$ form. The standard Gibbs reaction energy (ΔG^0_{rxn}) for the redox reaction between $[\text{Pt}^{\text{II}}\text{Cl}_4]^{2-}$ and $[\text{Ir}^{\text{IV}}\text{Cl}_6]^{2-}$ was determined to be $-42.45 \text{ kJ}\cdot\text{mol}^{-1}$ and $K_{\text{eq}} = 2.73 \times 10^7$. Furthermore, the kinetics of the reaction between $[\text{Pt}^{\text{II}}\text{Cl}_4]^{2-}$ and $[\text{Ir}^{\text{IV}}\text{Cl}_6]^{2-}$ was studied as a function of reagent concentration, ionic strength and temperature and enabled us to derive a suitable reaction rate model, Reactions 3.12 and 3.13.



The kinetic runs at varying temperature were used to determine the enthalpy- and entropy of activation ($\Delta H^\ddagger = 36.65 \pm 0.24 \text{ kJ}\cdot\text{mol}^{-1}$ and $\Delta S^\ddagger = -107.76 \pm 0.87 \text{ J}\cdot\text{mol}^{-1}\cdot\text{K}^{-1}$) for the Reaction 3.12. An IP-HPLC method was developed for the separation of $[\text{Pt}^{\text{IV}}\text{Cl}_6]^{2-}$, $[\text{Pt}^{\text{II}}\text{Cl}_4]^{2-}$, $[\text{Ir}^{\text{IV}}\text{Cl}_6]^{2-}$, $[\text{Ir}^{\text{III}}\text{Cl}_6]^{3-}$ and their respective aquation products. The relatively large negative ΔS^\ddagger for the reaction between $[\text{Pt}^{\text{II}}\text{Cl}_4]^{2-}$ and $[\text{Ir}^{\text{IV}}\text{Cl}_6]^{2-}$ and the absence of $[\text{Ir}^{\text{III}}\text{Cl}_6]^{3-}$

in the chromatographic trace, Figure 4.11, support the notion that chloride transfer facilitates electron transfer during the redox reaction.

5.2. A more detailed conclusion of this project

5.2.1. Kinetic investigation of the multi-step oxidation of $[Pt^{II}Cl_4]^{2-}$ by $[Ir^{IV}Cl_6]^{2-}$

The reduction half reactions of $[Pt^{IV}Cl_6]^{2-}$ and $[Ir^{IV}Cl_6]^{2-}$ indicate that a redox reaction between the $[Pt^{II}Cl_4]^{2-}$ and $[Ir^{IV}Cl_6]^{2-}$ complex anions will occur, Reactions 3.3 and 3.4. Moreover, the half cell potentials were used to determine the standard Gibbs reaction energy ($\Delta G^0_{rxn} = -42.45 \text{ kJ.mol}^{-1}$) and equilibrium constant ($K_{eq} = 2.73 \times 10^7$) for this redox reaction. The stoichiometric relationship for the reaction between $[Pt^{II}Cl_4]^{2-}$ and $[Ir^{IV}Cl_6]^{2-}$ was determined by monitoring the UV-Vis spectral changes as a function of time, Figures 3.2 and 3.3, and a stoichiometric relationship of 2 $[Ir^{IV}Cl_6]^{2-}$:1 $[Pt^{II}Cl_4]^{2-}$ was obtained. In order to determine the reaction rate between $[Pt^{II}Cl_4]^{2-}$ and $[Ir^{IV}Cl_6]^{2-}$ in a chloride rich acidic matrix a kinetic study was performed as a function of reagent concentration, ionic strength, H^+ concentration and temperature, Figures 3.4 - 3.8. The rate model is proposed to comprise of two consecutive elementary steps, Reactions 3.12 and 3.13, based on the reduction half reactions of $[Ir^{IV}Cl_6]^{2-}$ and $[Pt^{II}Cl_4]^{2-}$, Reactions 3.3 and 3.4, and preliminary simulation results of the kinetic data. The first elementary step consists of the reduction of Ir^{IV} to Ir^{III} with the oxidation of Pt^{II} to form a postulated Pt^{III} intermediate. The second elementary step will be the further reaction of the Pt^{III} intermediate with another Ir^{IV} complex, and is consistent with a stoichiometry of 2 $[Ir^{IV}Cl_6]^{2-}$:1 $[Pt^{II}Cl_4]^{2-}$. Furthermore, it was established that the reaction rate is first order with respect to the concentrations of both $[Ir^{IV}Cl_6]^{2-}$ and $[Pt^{II}Cl_4]^{2-}$ species and the multi-step redox reaction rate model was derived, Equations 3.14 - 3.18. Using the program *Equikin*, the multi-step redox reaction rate model was simulated and the non-linear least-squares fits obtained are shown in Figures 3.9 and 3.10. The consistency of the rate constant ($k_1 = 7.04 \pm 0.34 \text{ M}^{-1}.\text{sec}^{-1}$) and molar extinction coefficient of $[Ir^{IV}Cl_6]^{2-}$ at 488 nm ($4003 \pm 63 \text{ M}^{-1}.\text{cm}^{-1}$) along with the excellent least-squares fits obtained validated the rate model with respect to the first elementary step. However, inconsistent values for the calculated rate constant ($k_2 = 2002.67 \pm 6300.18 \text{ M}^{-1}.\text{sec}^{-1}$) were obtained. Therefore, refinement of the multi-step redox reaction rate model with respect to the second elementary step was required. Reported investigations of similar redox reactions with Pt^{III} show that this species is highly reactive and the reported reactions were all described as diffusion controlled

reactions.^{37,43} The multi-step redox reaction rate model was refined to reflect the high reactivity of Pt^{III} by assuming that the second elementary step occurs instantaneous ($k_2 = \infty$), which implies that the concentration of Pt^{III} at any given time is negligible ($Pt^{III} = 0$). By applying the steady state approximation, Equations 3.19 - 3.22, the diffusion controlled rate model was derived, Equations 3.22 - 3.25, and simulated to the experimental data. The calculated rate constant ($k_1 = 6.60 \pm 0.46 \text{ M}^{-1}.\text{sec}^{-1}$) and molar extinction coefficient of $[Ir^{IV}Cl_6]^{2-}$ at 488 nm ($4258 \pm 209 \text{ M}^{-1}.\text{cm}^{-1}$) yield very consistent data, Table 3.6, and the excellent correlation of the non-linear least-squares fits, Figures 3.12 and 3.13, further support the assumption that $k_2 = \infty$. Moreover, the calculated rate constant (k_1) obtained with the diffusion controlled rate model compares very well with the rate constant (k_1) calculated with the multi-step redox reaction rate model ($k_1 = 7.04 \pm 0.34 \text{ M}^{-1}.\text{sec}^{-1}$). The average calculated rate constant (k_1) and molar extinction coefficient of $[Ir^{IV}Cl_6]^{2-}$ at 488 nm were fitted to the experimental data using the program *Equikin*, Figures 3.14 and 3.15, and in most cases very good fits are obtained. The diffusion controlled rate model was simulated and fitted to the kinetic data collected at varying ionic strength. The simulations illustrate that an increase in the rate constant (k_1) is obtained as the $NaClO_4$ concentration increases. At higher Na^+ concentration, presumably more solvent separated ion-pairs form with the reactants, 'lowering' the repulsion between negatively charged reactants and results in an increase in the rate constant.¹⁸ The diffusion controlled rate model was simulated to the kinetic data collected at varying temperatures. The non-linear least-squares fits show excellent correlation between the experimental and simulated data, Figure 3.18. The calculated rate constants (k_1) were used to construct an Eyring plot, Figure 3.19, and the linear relationship between $\ln(k_1/T)$ versus $1/T$ indicates that the enthalpy of activation ($\Delta H^\ddagger = 36.65 \pm 0.24 \text{ kJ.mol}^{-1}$) is independent of temperature in the range of 301.1 - 310.1 K. Furthermore, the relatively large negative entropy of activation ($\Delta S^\ddagger = -107.76 \pm 0.87 \text{ J.mol}^{-1}.\text{K}^{-1}$) is indicative of an associative reaction mechanism. Utilizing the enthalpy- and entropy of activation the Gibbs energy of activation was calculated ($\Delta G^\ddagger = 68.77 \pm 0.15 \text{ kJ.mol}^{-1}$) at 298.1 K. Taking into account the redox reaction of $[Ir^{IV}Cl_6]^{2-}$ and $[Pt^{II}Cl_4]^{2-}$ during the simultaneous ClO_3^- oxidation of $[Pt^{II}Cl_4]^{2-}$ and $[Ir^{III}Cl_6]^{3-}$ in a mixed metal solution, the predicted species evolution ($[Ir^{IV}Cl_6]^{2-}$ and $[Pt^{IV}Cl_6]^{2-}$) will be drastically influenced. Comparison of the ClO_3^- oxidation rate of $[Ir^{III}Cl_6]^{3-}$ ($8.25 \times 10^{-5} \text{ M}^{-1}.\text{sec}^{-1}$) and the redox reaction rate ($k_1 = 6.60 \pm 0.46 \text{ M}^{-1}.\text{sec}^{-1}$) suggest that any $[Ir^{IV}Cl_6]^{2-}$ formed in this reaction mixture will be reduced by the $[Pt^{II}Cl_4]^{2-}$ present in the solution. Therefore, the formation of $[Ir^{IV}Cl_6]^{2-}$ will be delayed until complete oxidation of $[Pt^{II}Cl_4]^{2-}$ has occurred. Furthermore,

the rate of $[\text{Pt}^{\text{II}}\text{Cl}_4]^{2-}$ oxidation will also be enhanced, since both the ClO_3^- oxidation ($k = 4.25 \times 10^{-3} \text{ M}^{-1} \cdot \text{sec}^{-1}$) and $[\text{Ir}^{\text{IV}}\text{Cl}_6]^{2-}$ oxidation will influence the species formation rate of $[\text{Pt}^{\text{IV}}\text{Cl}_6]^{2-}$. The simulation of this complex series of redox reactions are shown in Figure 3.22 and clearly illustrate the induction period for $[\text{Ir}^{\text{IV}}\text{Cl}_6]^{2-}$ formation.

ESI-Q-TOF-MS evidence for the existence of a Pt^{III} chlorido complex in the form of $[\text{Pt}^{\text{III}}\text{Cl}_4]^-$ was obtained during the analysis of $[\text{Pt}^{\text{IV}}\text{Cl}_6]^{2-}$. It was also found that the applied cone voltage significantly influences the extent of $[\text{Pt}^{\text{IV}}\text{Cl}_6]^{2-}$ fragmentation, Figure 3.20. The $[\text{Pt}^{\text{IV}}\text{Cl}_6]^{2-}$ fragments were unambiguously assigned by using distinct isotopologue peak patterns obtained for each fragment, Figure 3.21.

5.2.2. A mechanistic investigation of the first oxidation reaction of $[\text{Pt}^{\text{II}}\text{Cl}_4]^{2-}$ by $[\text{Ir}^{\text{IV}}\text{Cl}_6]^{2-}$

An IP-HPLC method was developed for the separation and quantification of the $[\text{Ir}^{\text{III}}\text{Cl}_n(\text{H}_2\text{O})_{6-n}]^{3-n}$ ($n = 4-6$) series of complex anions. This IP-HPLC method was utilized to determine the aquation rate constants (k_{aq1} , k_{aq2}) of $[\text{Ir}^{\text{III}}\text{Cl}_6]^{3-}$ and $[\text{Ir}^{\text{III}}\text{Cl}_5(\text{H}_2\text{O})]^{2-}$ in 0.10 M HCl, Figures 4.2 (a) and (b). Using Equation 4.14 the change in concentrations of each Ir^{III} species were calculated as a function of time. A pseudo-first order rate model, Equations 4.11 - 4.13, was simulated to the experimental data and good correlation between the calculated and simulated data was obtained, Figure 4.4. The resulting calculated rate constants were $k_{\text{aq1}} = 3.50 \pm 0.12 \times 10^{-5} \text{ sec}^{-1}$ and $k_{\text{aq2}} = 1.14 \pm 0.10 \times 10^{-6} \text{ sec}^{-1}$. Moreover, the aquation of $[\text{Ir}^{\text{III}}\text{Cl}_6]^{3-}$ was studied as a function of temperature in the range of 295.1 - 315.1 K and the resulting rate constants (k_{aq1}), Table 4.2, were used to construct the Eyring plot, Figure 4.6. From this Eyring plot the $\Delta H^\ddagger = 99.41 \pm 0.09 \text{ kJ} \cdot \text{mol}^{-1}$ and $\Delta S^\ddagger = 40.70 \pm 0.17 \text{ J} \cdot \text{mol}^{-1} \cdot \text{K}^{-1}$ were calculated and these values correlated to a $\Delta G^\ddagger = 87.28 \pm 0.04 \text{ kJ} \cdot \text{mol}^{-1}$ at 298.1 K. In contrast to the redox reaction between $[\text{Ir}^{\text{IV}}\text{Cl}_6]^{2-}$ and $[\text{Pt}^{\text{II}}\text{Cl}_4]^{2-}$, the positive ΔS^\ddagger obtained for the aquation of $[\text{Ir}^{\text{III}}\text{Cl}_6]^{3-}$ supports a dissociative mechanism for the aquation of $[\text{Ir}^{\text{III}}\text{Cl}_6]^{3-}$.

With respect to the first elementary step of the redox reaction between $[\text{Ir}^{\text{IV}}\text{Cl}_6]^{2-}$ and $[\text{Pt}^{\text{II}}\text{Cl}_4]^{2-}$ the relatively large negative entropy of activation (ΔS^\ddagger) suggests that an associative mechanism occurs. Investigation of the products formed during the oxidation of $[\text{Pt}^{\text{II}}\text{Cl}_4]^{2-}$ in chloride deficient matrices will enable the elucidation of the reaction mechanism. However, this required a detailed understanding of the aquation rates of $[\text{Ir}^{\text{IV}}\text{Cl}_6]^{2-}$, $[\text{Pt}^{\text{II}}\text{Cl}_4]^{2-}$, $[\text{Pt}^{\text{IV}}\text{Cl}_6]^{2-}$ and $[\text{Ir}^{\text{III}}\text{Cl}_6]^{3-}$ to account for the formation of their respective aquation products during the

chromatographic runs. The aquation rates of $[\text{Pt}^{\text{IV}}\text{Cl}_6]^{2-}$ and $[\text{Ir}^{\text{IV}}\text{Cl}_6]^{2-}$ are relatively slow, to the extent that no aquation can spectrophotometrically be observed within the timeframe of 5 hours. However, in the presence of $[\text{Pt}^{\text{II}}\text{Cl}_4]^{2-}$ the $[\text{Pt}^{\text{IV}}\text{Cl}_6]^{2-}$ species will rapidly aquate ($k \approx 5 \times 10^5 \text{ sec}^{-1}$) and equilibrium will be reached before analysis can be carried out. This implies that, irrespective of the redox mechanism, the same Pt^{IV} species distribution will be obtained upon analysis of the reaction products. In a 0.1 M HCl matrix $[\text{Pt}^{\text{II}}\text{Cl}_4]^{2-}$ will aquate to a limited extent and only 3 % of the $[\text{Pt}^{\text{II}}\text{Cl}_3(\text{H}_2\text{O})]^-$ species will form. In order to analyse the products formed during the redox reaction of $[\text{Pt}^{\text{II}}\text{Cl}_4]^{2-}$ and $[\text{Ir}^{\text{IV}}\text{Cl}_6]^{2-}$ an IP-HPLC method was developed for the sufficient separation of the $[\text{Pt}^{\text{II}}\text{Cl}_4]^{2-}$, $[\text{Pt}^{\text{IV}}\text{Cl}_6]^{2-}$, $[\text{Ir}^{\text{III}}\text{Cl}_6]^{3-}$ complexes and their aquation products, Figures 4.7 - 4.9. The relative retention times and PDA spectra of the peaks obtained in the chromatographic traces were used to assign the peaks. A sample containing 10 mM $[\text{Ir}^{\text{IV}}\text{Cl}_6]^{2-}$ and 10 mM $[\text{Pt}^{\text{II}}\text{Cl}_4]^{2-}$ in 0.10 M HCl was left to react for 5 minutes and injected onto the C_{18} -column to investigate whether chloride transfer occur during the reaction of $[\text{Ir}^{\text{IV}}\text{Cl}_6]^{2-}$ and $[\text{Pt}^{\text{II}}\text{Cl}_4]^{2-}$, Figure 4.11. No peak for the $[\text{Ir}^{\text{III}}\text{Cl}_6]^{3-}$ species was obtained which indicates that chloride transfer does occur during the redox reaction, with the formation of $[\text{Ir}^{\text{III}}\text{Cl}_5(\text{H}_2\text{O})]^{2-}$ as product. Moreover, the lack of a chromatographic peak for $[\text{Ir}^{\text{III}}\text{Cl}_6]^{3-}$ signifies that the second redox reaction, Reaction 3.13, occurs via a similar mechanism and a proposed reaction mechanism for the redox reaction between $[\text{Ir}^{\text{IV}}\text{Cl}_6]^{2-}$ and $[\text{Pt}^{\text{II}}\text{Cl}_4]^{2-}$ was derived, Scheme 4.1.

References

1. D.L. Buchanan., *Platinum Group Element Exploration*, Elsevier, Amsterdam. **1988**.
2. C.R.M. Rao, G.S. Reddi., *Trends. Anal. Chem.* **2000**, *19*, 565
3. H. Zhang, M. Jin, Y. Xia., *Chem. Soc. Rev.* **2012**, *41*, 8035-8049
doi: 10.1039/c2cs35173k
4. F.L. Bernardis, R.A. Grant and D.C. Sherrington., *React. Funct. Polym.* **2005**, *65*, 205.
5. G.M. Mudd, B.J. Glaister., *The Environmental Costs of Platinum-PGM Mining: An Excellent Case Study In Sustainable Mining. Proc.* “48th Annual Conference of Metallurgists”, Canadian Metallurgical Society, Sudbury, Ontario, Canada. **2009**.
6. B. Fischer., *Platinum Metals Rev.* **1992**, *36*, 14-25
7. R.J. Seymore, J.I. O’Farrelly, L.C. Potter., *Kirk-Othmer Encyclopedia of Chemical Technology*, vol. 19, fourth ed., in: M. Howe-Grant (Ed.) Wiley, New York, **1998**, 367
8. G. Ertl, H. Knozinger, F. Schuth, J. Weitkamp, *Handbook of Heterogeneous Catalysis*, Wiley-VCH, Weinheim, 2nd ed. **2008**, 37–56.
9. L. B. Hunt., *Platinum Metals Rev.* **1958**, *2*, 129-134
10. R.T. Jones., *An overview of Southern African PGM Smelting, Nickel and Cobalt 2005: Challenges in Extraction and Production*, 44th Annual Conference of Metallurgists, Calgary, Alberta, Canada. **2005**, 147-178.
11. C.F. Vermaak., *The Platinum-Group Metals – A Global Perspective*, Mintek, Randburg, South Africa. **1995**, 247

References

12. F. Crudwell, M. Moats, V. Ramachandran, T. Robinson, V.G. Davenport., *Extractive Metallurgy of Nickel, Cobalt and Platinum-Group Metals*. Elsevier Ltd. **2011**
doi: 10.1016/B978-0-08-096809-4.10037-1
13. R.I. Edwards, W.A.M. teRiele, G.J. Bernfield., *Handbook of Inorganic Chemistry*, Suppl. vol. A1, ed. J. K. Acres and K. Swars, Springer Verlag, Berlin, **1986**.
14. R.I. Edwards., *The Refining of the Platinum-Group Metals*, National Institute for Metallurgy, **1975**, 514
15. P. Murray, K.R. Koch., *J. Coord. Chem.* **2010**, 63, 2561-2577
16. G.A. Rechnitz, J.E. McClure., *Anal. Chem.* **1964**, 36, 2265-2270
17. J. Halpern, M. Pribanic., *J. Am. Chem. Soc.* **1968**, 90, 5942
18. F.A. Cotton, G. Wilkonson., *Advances in Inorganic Chemistry*, New York: John Wiley and Sons, inc. **1966**, 1306-1318
19. H. Taube, H. Myers., *J. am. Chem. Soc.* **1954**, 76, 2103-2111
20. S.A. Arrhenius., *Z. Phys. Chem.* **1889**, 4, 226
21. K.J. Laidler, M.C. King., *J. Phys. Chem.* **1983**, 87, 2657
22. H. Eyring., *Chem. Reviews.* **1935**, 17. 1
23. R.A. Marcus., *J. Chem. Phys.* **1956**, 24, 996
24. R.A. Marcus., *J. Chem. Phys.* **1965**, 43, 679-671
25. R.A. Marcus., *Electron Transfer Reactions in Chemistry: Theory and Eperiment*, Nobel lecture, **1992**
26. W.J. Gerber, K.R. Koch, H.E. Rohwer, E.C. Hosten, T.E. Geswindt, *Talanta.* **2010**, 82, 348
27. W.J. Gerber, Ph.D. Thesis, Nelson Mandela Metropolitan University. **2006**

References

28. R.L. Burden, J.D. Faires., *Numerical Analysis, 6th ed.*, Brooks/Cole Publishing Company. **1997**.
29. E. Kreyszig., *Advanced Engineering Mathematics, 6th ed.*, John Wiley & Sons. **1988**, 1120-1129
30. P. van Wyk, W.J. Gerber, K.R. Koch., *Anal Chim Acta*, **2011**, 704, 154-161
doi: 10.1016/j.aca.2011.07.037
31. J.J. Kirkland, J.J. DeStefano., *J. Chromatogr. A*. **2006**, 50, 1126
32. F. Basolo, P.H. Wilks, R.G. Pearson, R.G. Wilkins., *J. Inorg. Nucl. Chem.* **1958**, 8, 203
33. F. Basolo, A.F. Messing, P.H. Wilks, R.G. Wilkins, R.G. Pearson., *J. Inorg. Nucl. Chem.* **1958**, 8, 203
34. F. Basolo, M.L. Morris, R.C. Pearson., *Discuss. Faraday Soc.* **1960**, 29, 80-91
35. L.I. Elding, L. Gustafson., *Inorganica Chimica Acta*, **1976**, 19, 31-38
36. R.L. Rich, H. Taube., *J. Am. Chem. Soc.* **1954**, 76, 2608-2611
37. R.C. Wright, G.S. Lawrence., *J.C.S. Chem. Comm.* **1972**, 132-133
38. I.A. Poulsen, C.S. Garner., *J. Am. Chem. Soc.* **1962**, 84, 2032
39. L.I. Elding., *Acta Chemica Scandanavica*, **1966**, 20, 2559-2567
40. Z. Zhou, W. Zhou, S. Wang, G. Wang, L. Jiang, H. Li, G. Sun, Q. Xin., *Catalysis Today*. **2004**, 93, 523-528
41. A. Garsot, H Chermette, WL Waltz, J Lilie., *Inorg. Chem.* **1989**, 28, 2241-2247
42. I.V. Znakovskaya, Y.A. Sosedova, E.M. Glebov, V.P. Grivin, V.F. Plyusnin., *Photochem. Photobiol. Sci.* **2005**, 4, 897-902
43. V.P. Grivin, I.V. Khmelinski, V.F. Plyusnin., *J. Photochem. Phorobiol. A: Chem.* **1991**, 62, 15-25

References

44. K.P. Balashev, I.I. Blinov and G.A. Shagisultanova, *Zh. Neorg. Khim.*, **1987**, 32, 2470-2474
45. V. P. Grivin, I. V. Khmelinski, V. F. Plyusnin, I. I. Blinov and K. P. Balashev., *J. Photochem. Photobiol. A:Chem.* **1990**, 51, 167.
46. J. H. Espenson., *Chemical Kinetics and Reaction Mechanisms*, McGraw-Hill, **1981**
47. W. Henderson, J. S. McIndoe., *Mass Spectrometry of Inorganic, Coordination and Organometallic Compounds: Tools-Techniques-Tips*, Copyright **2005** John Wiley & Sons, Ltd. ISBNs: 0-470-85015-9 (HB); 0-470-85016-7 (PB)8
48. H. Taube., *J. Am. Chem. Soc.* **1955**, 77, 4481
49. H. Taube, H. Myers, R.L. Rich., *J. Am. Chem. Soc.* **1953**, 75, 4118
50. D.L. Ball, E.L. King., *J. Am. Chem. Soc.* **1958**, 80, 1091
51. D.R. Stranks., *Discuss. Faraday Soc.* **1960**, 29, 73-79
52. N.S. Biradar, D.R. Stranks, M.S. Vaidya., *Trans Faraday Soc.* **1962**, 58, 2421-2432
53. B. Durham, J.F. Endicott, C. Wong, D.P. Rillema., *J. Am. Chem. Soc.* **1979**, 101, 847-857
54. A. Zwickel, H. Taube., *J. Am. Chem. Soc.* **1961**, 83, 793
55. T. Shi, L.I. Elding., *Inorg. Chim. Acta.* **1998**, 282, 55-60
56. H.V. Huynh, T.J. Meyer., *Chem. Rev.* **2007**, 107, 5004-5064
57. J. Kramer, K. R. Koch., *Inorg. Chem.* **2007**, 46, 7466
58. H. Archibald., *J. Chem. Soc. Trans.* **1920**, 117, 1104-1120
59. H. Archibald, W.A. Gale., *J. Chem. Soc. Trans.*, **1922**, 121, 2849
60. C. M. Davidson, R. F. Jameson., *Trans. Faraday Soc.* **1965**, 61, 2462-2467.
61. L.E. Cox, D.G. Peters, E.L. Wehry., *J. inorg. nucl. Chem.* **1972**, 34, 297-305

References

62. W.J. Gerber, P. Murray, K.R. Koch., *Dalton*. **2008** doi: 10.1039/b807831a
63. F.A. Cotton, G. Wilkonson., *Advances in Inorganic Chemistry.*, New York: John Wiley and Sons, inc. **1966**, 1011
64. E.M. Glebov, V.F. Plyusnin, N.V. Tkachenko, H. Lemmetyinen., *Russ.Chem.Bull. Int.Ed.* **2008**, 57, 2487-2494
65. J.C. Chang, C.S. Garner., *Inorg. Chem.* **1965**, 4, 209-215
66. A.A. El-Awady, E.J. Bounsall, C.S.Garner., *Inorg.Chem.* **1967**, 6, 79-86
67. A.J.P. Domingos, A.M.T.S. Domingos, J.M. Peixoto Cabral., *J. inorg. nucl. Chem.* **1969**, 31, 2563-2573.
68. F.A. Cotton, G. Wilkonson., *Advances in Inorganic Chemistry.*, New York: John Wiley and Sons, inc. **1966**, p.1285-1289

Appendix A

An ion-pairing reversed phase UHPLC-ESI-Q-TOF-MS method for the characterization of $[\text{Pt}^{\text{IV}}\text{Cl}_{6-n}\text{Br}_n]^{2-}$ ($n = 0 - 6$) and mono-aquated $[\text{Pt}^{\text{IV}}\text{Cl}_{5-n}\text{Br}_n(\text{H}_2\text{O})]^-$ ($n = 0 - 5$) species at the sub parts per million range
